OXYGEN DEPENDENCE OF TETRAHYDROFURAN COMBUSTION USING JET-STIRRED REACTOR EXPERIMENTS AND CHEMICAL KINETICS MODELING

by

ALANNA KORITZKE

(Under the Direction of Brandon Rotavera)

ABSTRACT

In an ongoing effort to mitigate climate change concerns from the transportation sector, development of next-generation biofuels concurrently with cleaner-burning, higher-efficiency engines that operate at low temperature (< 1200 K) remains a top priority of the U.S. and international entities. Balancing climate concerns with rising transportation energy demands has created a need for diversifying biofuel beyond ethanol and biodiesel. However, the impact on ignition from using new biofuels is an ongoing area of research. Such insight is critical for developing predictive modeling tools and is supported by isomer-resolved speciation measurements. The experiments of the work herein use a jet-stirred reactor (JSR) paired with vacuum-ultraviolet absorption spectroscopy and electron-impact mass spectrometry to provide isomer-resolved speciation measurements, a process that was developed as described in this work.

Low-temperature combustion of tetrahydrofuran, a next-generation biofuel, involves competing reactions that depend on temperature, pressure, and oxygen concentration, including ring-opening and subsequent oxidation of initial radicals (Ṙ), HOȮ-elimination yielding dihydrofuran isomers, and the formation of peroxy radicals

(ROȮ). The latter species can isomerize to hydroperoxy-substituted radicals (ȮOOH) that undergo either unimolecular decomposition or second-O_2-addition. To examine the influence of temperature and oxygen concentration on intermediates from tetrahydrofuran, isomer-resolved speciation measurements were conducted at 810 Torr in a JSR from 500 – 1000 K. Resulting from negative-temperature coefficient behavior, species concentrations peaked at two temperatures, 600 K and 800 K, which were then selected for separate experiments to quantify O_2-dependence using O_2 concentrations of $0.37 – 7.40 \cdot 10^{18}$ molecules cm^{-3}.

Several species were detected for the first time, including constitutional isomers tetrahydrofuran-3-one, butanedial, and allyl formate; the latter two resulting from ring-opening reactions of ȮOOH radicals. For the majority of species, clear dependence on O_2 exists that is not captured quantitatively by chemical kinetics mechanisms. The experiments herein provide new targets for refinement of chemical kinetics mechanisms of tetrahydrofuran. The discrepancies existing between the measured and model-predicted species profiles indicate that sub-mechanisms for important intermediates may require additional elementary reactions, such as for dihydrofuran isomers. In addition, rates for O_2-addition to tetrahydrofuranyl radicals in chemical kinetics mechanisms, which employ rate rules from alkyl radicals, require scrutiny.

INDEX WORDS: biofuel, low-temperature combustion, tetrahydrofuran, transportation energy, absorption spectroscopy, mass spectrometry

OXYGEN DEPENDENCE OF TETRAHYDROFURAN COMBUSTION USING JET-STIRRED REACTOR EXPERIMENTS AND CHEMICAL KINETICS MODELING

by

ALANNA KORITZKE

BS, Northern Arizona University, 2015

A Dissertation Submitted to the Graduate Faculty of The University of Georgia in Partial Fulfillment of the Requirements for the Degree

DOCTOR OF PHILOSOPHY

ATHENS, GEORGIA

2022

OXYGEN DEPENDENCE OF TETRAHYDROFURAN COMBUSTION USING JET-STIRRED REACTOR EXPERIMENTS AND CHEMICAL KINETICS MODELING

by

ALANNA KORITZKE

Major Professor:	Brandon Rotavera
Committee:	Geoffrey Smith
	Amanda Frossard

Electronic Version Approved:

Ron Walcott
Vice Provost for Graduate Education and Dean of the Graduate School
The University of Georgia
December 2022

ACKNOWLEDGEMENTS

I would like to acknowledge and thank Dr. Brandon Rotavera for his guidance, my lab mates for their support, and my boyfriend, family, and friends for their love.

TABLE OF CONTENTS

Page

LIST OF TABLES vii

LIST OF FIGURES viii

CHAPTER

1 INTRODUCTION 1

1.1 CHALLENGES WITHIN THE TRANSPORTATION SECTOR 1

1.2 RESEACH APPROACHES TO COMBUSTION CHEMISTRY 12

2 EXPERIMENTAL APPROACH 24

2.1 JET-STIRRED REACTOR FACILITY 24

2.2 OFFLINE ANALYTICAL METHODS 33

2.3 DEVELOPMENT OF IDENTIFICATION AND QUANTIFICATION TECHNIQUES 39

2.4 EXPERIMENTAL CONDITIONS OVERVIEW 65

3 COMPUTATIONAL APPROACH 67

3.1 CHEMKIN PERFECTLY STIRRED REACTOR MODULE 67

3.2 LOW-TEMPERATURE CHEMICAL KINETICS MECHANISMS OF TETRAHYDROFURAN 70

4 OXYGEN DEPENDENCE OF TETRAHYDROFURAN COMBUSTION AT LOW-TEMPERATURE 72

4.1 EXPERIMENTAL RESULTS 72

4.2 DISCUSSION 95

5 CONCLUSIONS AND PROJECTIONS 106

REFERENCES 109

APPENDICES

A DEVELOPMENT OF SYRINGE-INJECTION OF LIQUIDS TO GC 118

B EXTERNAL COLLABORATIVE WORK 121

C STANDARD OPERATING PROCEDURES DEVELOPED 129

LIST OF TABLES

Page

Table 1: Definitions of absorption quantification terms 55

Table 2: Overview of Δt from chromatograms from 12 species.....60

Table 3: Initial experimental mole fractions 66

Table 4: Tabulated changes in [2,3-dihydrofuran] as a function of [O_2].....78

Table A1: Dilution factors and corresponding split ratios.....118

Table C1: Overview of standard operating procedures developed.....130

LIST OF FIGURES

Page

Figure 1: Molecular structure of tetrahydrofuran 1

Figure 2: Energy Information Agency transportation sector statistics 3

Figure 3: Soot-NO_x tradeoff.....6

Figure 4: Ignition delay times of cyclopentane and tetrahydrofuran.....7

Figure 5: Low-temperature combustion scheme for alkanes with examples from cyclopentane 9

Figure 6: Functional group behavior examples with cyclohexene and tetrahydropyran...11

Figure 7: Combustion research overview 14

Figure 8: Mechanism truncation error versus lumping.....18

Figure 9: Butanedial formation pathway 20

Figure 10: Jet-stirred reactor schematic details 25

Figure 11: Overview of experimental workflow 26

Figure 12: Vapor Delivery Module schematic.....29

Figure 13: Temperature homogeneity measurements.....32

Figure 14: Analytical diagnostics schematic 34

Figure 15: Accessible electronic transitions via absorption spectroscopy instrument 35

Figure 16: Multi-dimensional dataset for 2,3- and 2,5-dihydrofuran 37

Figure 17: Absorption cross-section comparison for cyclopentane, cyclopentene, and tetrahydropyran.....39

Figure 18: Gas-chromatograph temperature ramping profile 40
Figure 19: Gas-chromatograph method optimization results.....41
Figure 20: Electron-impact mass spectrometry conventional fragmentation mechanisms.....43
Figure 21: EI-MS spectrum and fragmentation patterns for *cis*-2,3-dimethyloxirane.....45
Figure 22: EI-MS spectrum and fragmentation patterns for 3,3-dimethyloxirane 46
Figure 23: EI-MS spectrum and fragmentation patterns for tetrahydrofuran 47
Figure 24: EI-MS spectrum and fragmentation patterns for tetrahydropyran 48
Figure 25: VUV absorption instrument schematic 52
Figure 26: VUV absorption saturation limit example with tetrahydrofuran.....53
Figure 27: VUV absorption detection limit example with 2-butanone.....54
Figure 28: Quantification methods summary 57
Figure 29: Impact of chromatographic Δt on extracted absorbance 59
Figure 30: 2,3-dihydrofuran reference and experimental sample signal overlaid 61
Figure 31: Signal deviation at high photon energy example with cyclopentane 61
Figure 32: Makeup gas pressure calibration curve 63
Figure 33: Convolved absorbance spectrum of tetrahydrofuran-3-one and butanedial with energy slice example.....65
Figure 34: Reaction pathway analyzer example of oxirane formation from tetrahydrofuran.....69
Figure 35: Types of reactions added to tetrahydrofuran chemical kinetics mechanism by Wu et al. 71
Figure 36: Example lumped reaction adopted by Wu et al.....71

Figure 37: Overview of detected species from tetrahydrofuran experiments.....73
Figure 38: Formally direct pathway example 73
Figure 39: Formation pathways of dihydrofuran isomers.....75
Figure 40: Temperature dependence of 2,3- and 2,5-dihydrofuran 76
Figure 41: Oxygen dependence of 2,3- and 2,5-dihydrofuran.....77
Figure 42: Pathway from 2,3-dihydrofuran to furan.....79
Figure 43: Temperature dependence and oxygen dependence of furan and cyclopropane carboxaldehyde 81
Figure 44: Rearrangement pathway of 2,3-dihydrofuran to cyclopropane carboxaldehyde 82
Figure 45: α-Ṙ ring opening pathways to oxirane and methyloxirane 83
Figure 46: Temperature dependence and oxygen dependence of oxirane and methyloxirane 84
Figure 47: Formation pathways of 1,2- and 3,4-epoxytetrahydrofuran.....85
Figure 48: Oxygen dependence of allyl formate.....87
Figure 49: Formation pathway of allyl formate from β,α'-ṪOOH 87
Figure 50: Formation pathways of tetrahydrofuran-2-one and tetrahydrofuran-3-one 88
Figure 51: Reference EI-MS and absorption spectra compared to measured experimental spectra for tetrahydrofuran-2-one and tetrahydrofuran-3-one 89
Figure 52: Proposed pathways for the formation of tetahydrofuran-3-one 90
Figure 53: Temperature dependence and oxygen dependence of tetrahydrofuran-3-one..91
Figure 54: Rate-of-production analyses for tetrahydrofuran-3-one.....92

Figure 55: Deconvolved absorbance spectrum of tetrahydrofuran-3-one and butanedial, temperature dependence and oxygen dependence of butanedial 95
Figure 56: Rate-of-production analyses for 2,3-dihydrofuran 98
Figure 57: Rate-of-production analyses for furan 102
Figure 58: Rearrangement network of 2,3-dihydrofuran, cyclopropane carboxaldehyde, and 2-butenal 104
Figure A1: Effect of split ratio and injection volume on signal saturation 120
Figure B1: Cyclohexene formation from cyclohexane, resonance stabilization of cyclohexenyl radicals, and ȮOOH radicals 122
Figure B2: Multi-plexed photoionization mass spectrometer schematic 124
Figure B3: Ring opening pathways of tetrahydropyran 126
Figure B4: Product formation of tetahydrofuran-3-one and 2-butenal via ketohydroperoxide-type radicals 127
Figure B5: Formation of diacetyl from ketohydroperoxide and ketohydroperoxide-type radicals 128

CHAPTER 1

INTRODUCTION

1.1 CHALLENGES WITHIN THE TRANSPORTATION SECTOR

The combustion community has ongoing research activities to contribute to two broad challenges that the transportation sector currently faces – rising energy demands and mitigating pollutant emissions. Continued progress in the development of new engine technologies focuses on more efficient and cleaner burning combustion, which inherently relies on a fundamental understanding of oxidation chemistry that drives combustion behavior. The motivation for the work herein is to contribute to the understanding of reaction mechanisms and combustion kinetics of a next-generation biofuel, tetrahydrofuran (**Figure 1**), in order to gain insight on combustion behavior relevant to current engines and those in development.

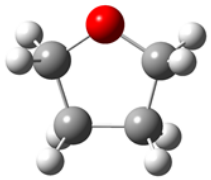

Figure 1. Molecular structure of tetrahydrofuran.

1.1.1. Transportation energy outlook

In a recent report, the United States Energy Information Agency (EIA) projects that in the next 30 years, energy demands will increase by over 50%.[1] Energy is consumed by five sectors within the United States; electric power, transportation, industrial, residential, and commercial where in 2021, the transportation sector consumed 27% of total energy

(**Figure 2a**).[1] Rising energy demands are easier met with an increased efficiency in each sector including the transportation sector where there is ongoing research in engine development and electricity integration. Still, the EIA also projects that liquid fuels will continue to provide greater than 95% of transportation energy needs by 2050 (**Figure 2b**).[1] Additionally in the transportation sector, internal combustion engines power over 99% of the cars on the road today and will continue to makeup ~97% in 2050.[2] However, transportation relies on petroleum-based fuels (i.e. gasoline and diesel) and internal combustion engines, contributes 27% of greenhouse gas emissions (**Figure 2c**), which includes ~79% CO_2, ~11% methane, ~7% NO_x, and ~3% other gases including fluorinated compounds and non-methane volatile organic compounds (**Figure 2d**).[3] Greenhouse gases – produced from all sectors and from all modes of powered transportation, including the production and development of batteries for electric cars – contribute to climate change and therefore, research efforts motivated by sustainable energy are ongoing to achieve higher-efficiency, cleaner burning engines.

While the de-carbonization of emissions can contribute to mitigating climate change concerns, it is worth noting that this is increasingly difficult do within the transportation sector because by its very definition, this sector requires that fuel by transported, which necessitates safety in handling and high energy density per unit volume of fuel to minimize the volume needed for transport. Therefore, the infrastructure (i.e. known safety risks and mitigation, existing pipeline, etc.) and high energy density of gasoline, diesel, and biofuels secures their role in transportation for the foreseeable future, as supported by projections by the EIA (**Figure 2b**).[1,4] Consequently, combustion research efforts aim to minimize the amount of carbon emitted from existing fuel systems by

incorporating new biofuels, increasing the composition of biofuels, and developing engines that operate at conditions in which emissions are less likely to form (see Section 1.1.2 and **Figure 3**).

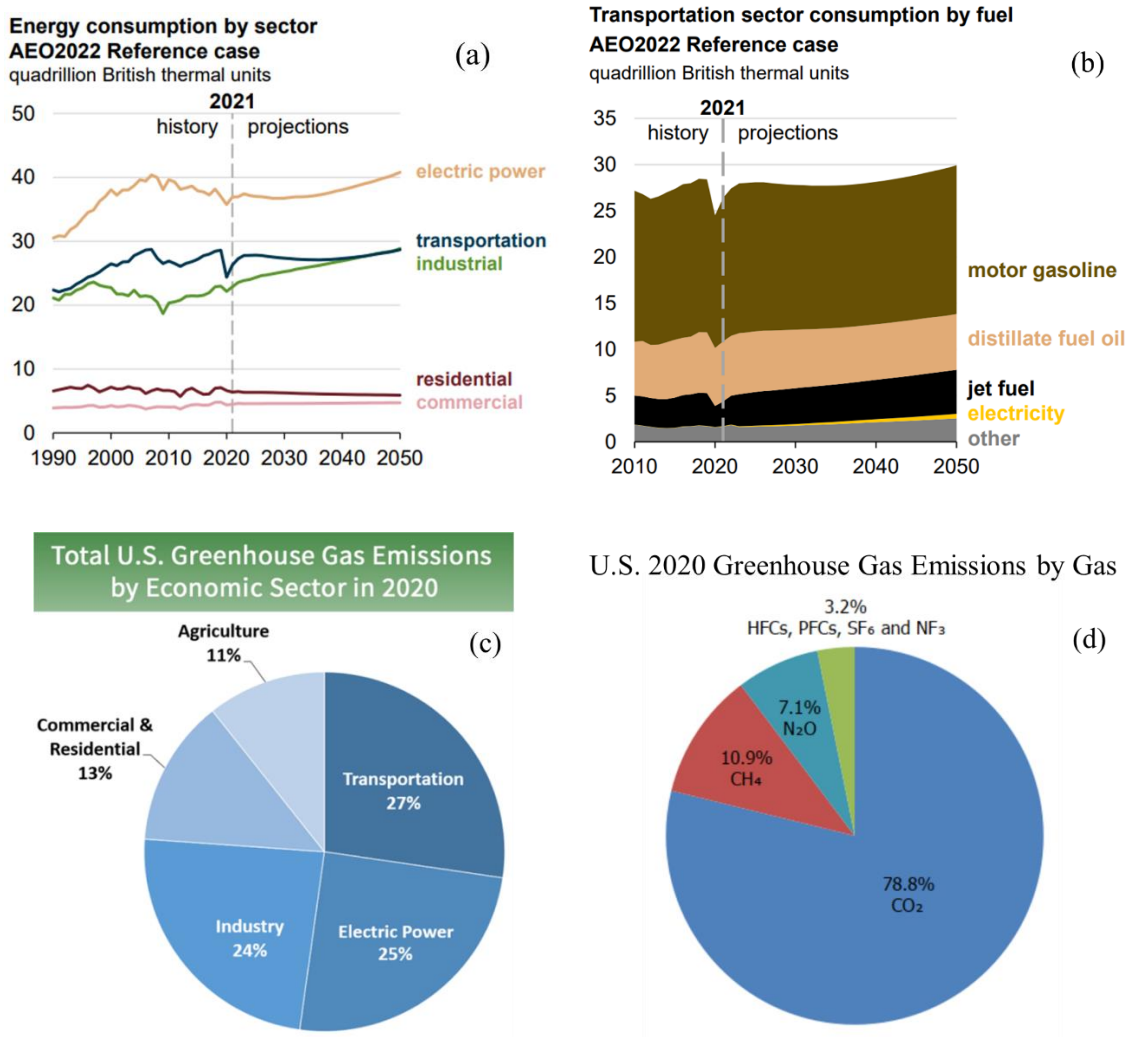

Figure 2. Energy consumption in the United States in 2021 by sector (a) and transportation sector consumption by fuel type (b). Data source: U.S. Energy Information Administration.[1] Total U.S. greenhouse gas emissions in 2020 by sector (c) and by gas (d) are sourced from the United States Environmental Protection Agency.[3]

1.1.2 Role of low-temperature combustion in sustainable transportation

In recent years, there has been a political and corporate push for full electrification of the transportation sector.[5–7] However, there are a number of challenges that are seldom accounted for nor publicized that pose challenges in relying solely on electrification. For example, there are unspecified and unknown repositories of rare earth metals and toxicity concerns of the raw materials needed for batteries and battery production is not an emissions-free process.[2,8–10] Human rights concerns are also an issue given that the location of raw materials are in countries without regulatory measures to ensure health and safety practices.[11,12] Batteries are also not robust enough for multi-modal transportation, especially aviation where batteries are inefficient at low temperature and cannot store the amount of energy needed for a long flight.[13,14] Finally, vehicles that require charging from an external source rely on local electric power grids, which still contribute to 25% of greenhouse gas emissions (**Figure 2c**).[3] Therefore, in addition to pursuing electric solutions, improving current combustion systems remains important in the near-term and in the long-term to contributing to climate change solutions.

One way to improve efficiency of internal combustion engines and reduce the dependence on petroleum-based fuels is to diversify current liquid fuels to maintain high energy density needed for transport and utilize existing infrastructure. The displacement of petroleum-derived fuels with biofuels, which is any fuel derived from biomass (i.e. plant material or agricultural waste), can reduce greenhouse gas emissions and can reduce production costs in comparison to petroleum-based fuels.[15–17] For example, two first-generation biofuels, which are derived from food-based sources, that are currently used are ethanol and biodiesel, where ethanol is partially integrated into gasoline at ~10% by

volume and most commonly up to 83% for flexible fuel vehicles, which contain an internal combustion engine designed to run on alternative fuel blends.[18,19] In diesel fuel, biodiesel is integrated most commonly at 5% by volume and up to 20%.[4] However, the production of first-generation biofuels (i.e. ethanol and biodiesel) is in competition with land and resources for agriculture food production and have a lower energy density around two-thirds that of gasoline.[20,21] Alternatively, next-generation biofuels are derived from lignocellulosic biomass via catalytic processes and have equivalent if not better energy densities compared to gasoline, making them favorable for use.[22–25]

In addition to changing fuel blend compositions, new engine technologies are in development to maximize efficiency while reducing emissions. Conventional spark-ignition and compression-ignition engines produce emissions based on the Soot-NO_x tradeoff, in which the former produces nitrous oxides (NO_x) and the latter produces soot (**Figure 3**). Ideally, to be cleaner-burning, new engine technologies could operate at conditions that minimize contributions to both emissions. This has led to the development of advanced compression ignition (ACI) designs including homogenous charge compression ignition engines (HCCI), which combines spark ignition with compression ignition strategies, is kinetically-controlled, and operates at low-temperature combustion (LTC) conditions where the formation of NO_x is less favorable.[26,27] The main driver for this work is contributing to the understanding the low-temperature combustion kinetics for next-generation biofuels, specifically tetrahydrofuran, relevant to fuel blends and ACI engines.

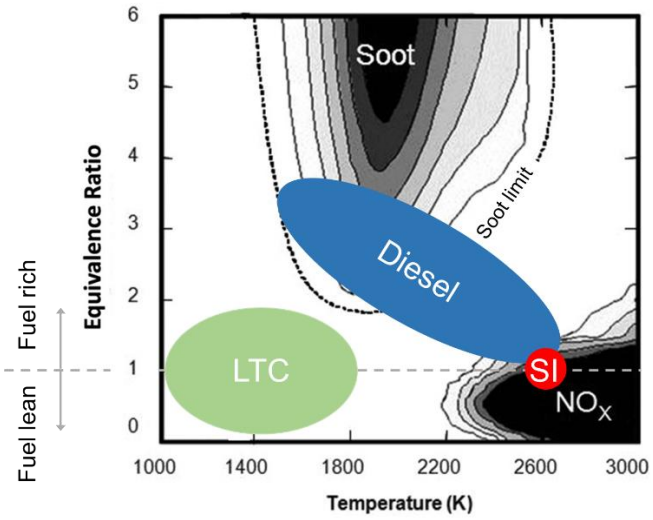

Figure 3. Soot-NO_x tradeoff adapted from Kalghatgi et al.[28] and Jeevahan et al.[27] in which spark ignition engines (SI in red) operate at high temperature and produce NO_x and diesel engines (blue) operate at high temperature and fuel rich conditions and produce both soot and NO_x. Low temperature combustion (LTC in green) are conditions in which both NO_x and soot formation are reduced. Equivalence ratio (ϕ) is defined as the ratio of the actual fuel-to-air ratio to the stoichiometric fuel-to-air ratio, where at stoichiometric conditions, all the O_2 is consumed in the reaction or $\phi = 1$. Therefore, fuel rich ($\phi > 1$) indicates that there is an excess of fuel compared to O_2 and fuel lean ($\phi < 1$) is the opposite.

ACI engines are kinetically controlled meaning that their operation relies on a fundamental understanding of combustion chemistry mechanisms, the reactivity of a fuel, and ignition behavior. For example, one such ignition behavior property that governs pre-ignition and knock phenomena is ignition delay time, defined as the time during which the radical pool is produced from a fuel and oxidizer mixture and subsequently leads to reaction at a given temperature and pressure, which varies with fuel-to-air equivalence ratio (ϕ) and fuel type.[29] Ignition delay time is a global metric that can be measured via experiments such as those using shock tubes and rapid compression machines (RCM) and provides insight into the chemical kinetics that govern combustion behavior.[30,31] In **Figure 4a**, an example pressure-time trace is shown from shock tube experiments of cyclopentane

done by Al Rashidi et al.[32] where ignition delay time is experimentally defined by the near-instantaneous increase in pressure, which corresponds to the time needed for combustion reactions to occur at the experimental conditions. Ignition delay time measurements and model predictions are shown in **Figure 4b** for cyclopentane from Al Rashidi et al.[33] and for tetrahydrofuran from Fenard et al.[34], where the ignition delay time trend changes due to the molecular structure of the fuel, which alters the network of combustion reactions responsible for the observed chemical behavior.

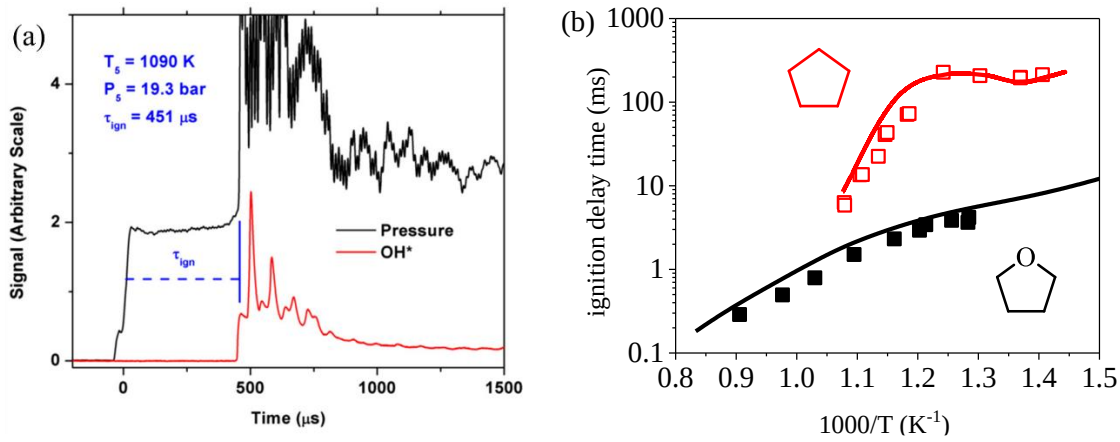

Figure 4. Pressure-time trace (a) for shock tube experiments of cyclopentane by Al Rashidi et al.[32] where ignition delay time is defined by the dashed blue line. Accompanying ignition delay time experimental data (points) and model predictions (lines) for cyclopentane from Al Rashidi et al.[32,33] and measurements of tetrahydrofuran from Fenard et al.[34] are shown in (b).

Specifically, in the ignition delay times shown in **Figure 4b** exhibit a negative trend with temperature where as temperature increases, the ignition delay time becomes shorter. This indicates that combustion is occurring more quickly because the time between radical pool formation and reaction is reduced as temperature increases. However, there are some conditions over which the opposite trend is observed, namely in cyclopentane, where as the temperature decreases, the ignition delay time becomes shorter. This is called the

negative temperature coefficient region (NTC) and is due to a shift in chemical reactions that are responsible for ignition behavior where peroxy radical chemistry becomes favored at low-temperature (< 1000 K). Further discussion of the NTC region is in Section 1.1.3. The general low-temperature combustion mechanism for alkanes follows a degenerate chain-branching scheme depicted in **Figure 5a**.[35] Similar reactions are prescribed for other types of molecules as well, augmented as appropriate to account for molecule-specific reactions such as OH-addition to C=C bonds in alkenes, for example. The low-temperature pathway begins with a fuel molecule, RH. Upon hydrogen abstraction, an alkyl radical, Ṙ, is produced. After an addition reaction with O_2, an alkylperoxy radical, ROȮ, is formed. Next, isomerization produces a highly reactive radical, called hydroperoxyalkyl (ȮOOH), which is the lynchpin of low-temperature chemistry.[36,37] ȮOOH is a carbon-centered radical (**Figure 5b**) that undergoes one of two critical steps in the forward direction: (1) chain-propagation whereby unimolecular reactions form cyclic ethers and carbonyls (**Figure 5c**), *β*-scission products, and conjugate alkenes; (2) second O_2-addition leading to ketohydroperoxides (HOOQ'=O) and causing chain-branching. Understanding the balance of ȮOOH reactions between unimolecular decomposition pathways and chain-branching via bimolecular reactions is essential because the timing of these reactions, on the order of tens of microseconds, dictates ignition delay time. However, ȮOOH is short-lived and therefore, difficult to detect directly due to low steady state concentrations. Therefore, in this work, mechanistic details are inferred by measuring the unimolecular decomposition products. More information on the goals of this work will be discussed in Section 1.2.2.

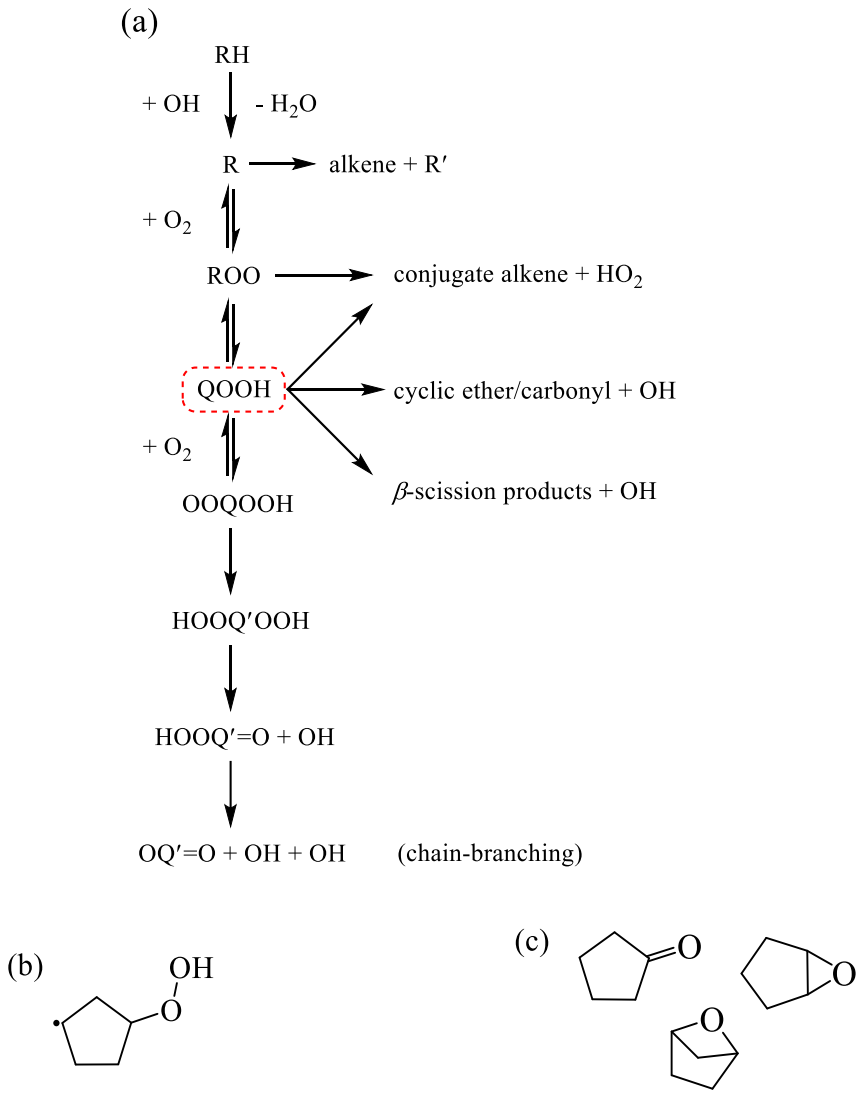

Figure 5. Low-temperature alkane oxidation scheme (a) where ȮOOH is highlighted in red as the fate of ȮOOH dictates ignition behavior. An example ȮOOH radical for cyclopentane is shown in (b). Expected cyclic ether and carbonyl products of cyclopentane oxidation are shown in (c) of which all are isomers of each other.

1.1.3 Next-generation biofuels

Biofuels are distinguished from one another based on their functional groups. The presence of functional groups, such as an ether group, often leads to a variation of the system of reactions that occur during combustion.[26] Ethers, including diethyl ether, tetrahydrofuran, and 2-methyltetrahydrofuran, are next-generation biofuels that are

expected to contribute to sustainable energy needs of today and to advance clean engine technologies of tomorrow.[38] Reaction mechanisms of functionalized biofuels remain an important area of research to the United States Department of Energy and to European counterparts. This work contributes to the effort by specifically focusing on the formation and consumption of partially oxidized intermediates.

While the low-temperature oxidation scheme shown in **Figure 5a** is based on alkane combustion behavior, functionalization of the fuel can affect which pathways are favored or, in some cases, accessible. For example, Koritzke et al.[37] showed that cyclohexene facilitates second-O_2 addition because the C=C double bond enables resonance stabilization of ȮOOH species, stabilizing the ȮOOH and increasing the well-depth on the potential energy surface of the corresponding RȮ, which inhibits ȮOOH unimolecular decomposition (**Figure 6a**) compared to cyclohexane.[37] Whereas, in tetrahydropyran oxidation, the presence of the ether group facilitates ȮOOH decomposition pathways, especially ring-opening, which reduces the already low steady-state concentration of ȮOOH and prevents second-O_2 addition to the ring and subsequent chain-branching pathways from the parent molecule (**Figure 6b**).[39] The goal of the work herein is to examine the effect of the ether group on oxidation pathways by studying tetrahydrofuran.

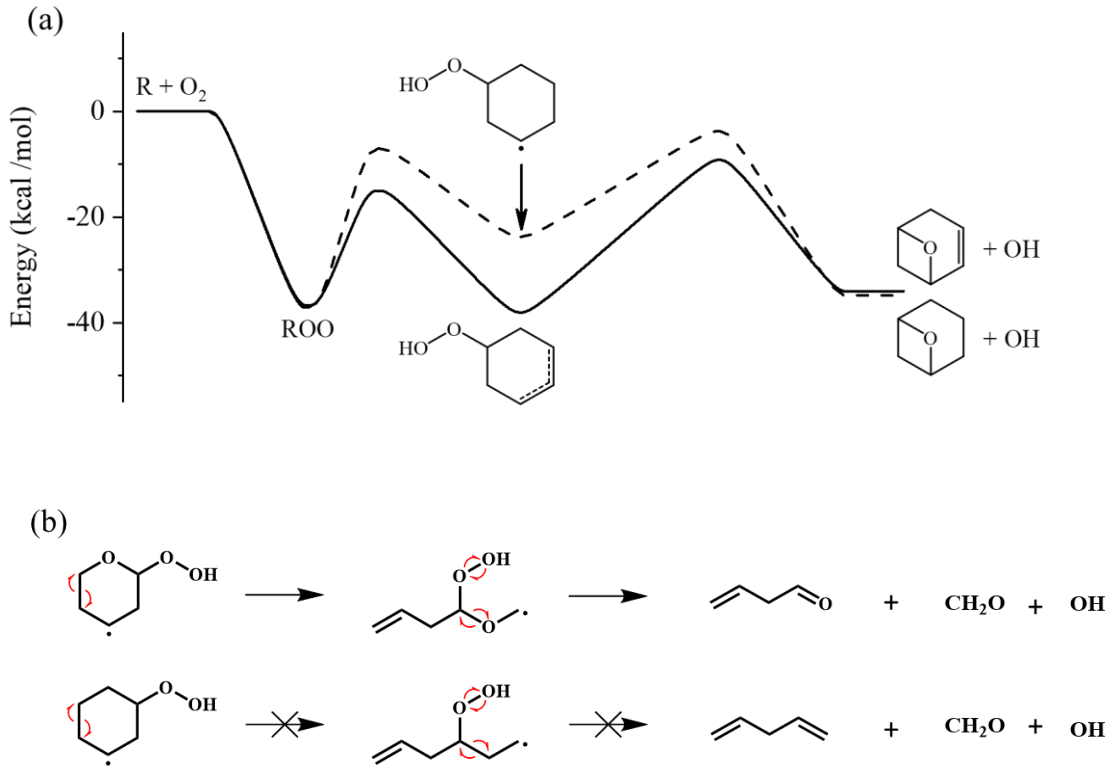

Figure 6. (a) Potential energy surfaces calculated at the CBS-QB3 level of theory for γ-ȮOOH radicals derived from cyclohexane (dashed line) and cyclohexene (solid line) where resonance-stabilization lowers the barrier for RO$\dot{O}$ → ȮOOH isomerization, yet increases the barrier for unimolecular decomposition. The combination of a lower barrier to isomerization and higher barrier to decomposition increases the potential for reactions of ȮOOH with O_2 or by ring-opening.[37] Example ring-opening reaction of tetrahydropyran facilitated by ether group (b) in comparison to cyclohexane where ring-opening products were not observed in experiments.[39]

Functional group effects can be observed in ignition behavior. In reference to the ignition delay times of cyclopentane and tetrahydrofuran (**Figure 4**), cyclopentane exhibits longer ignition delay times by two orders of magnitude compared to tetrahydrofuran indicating that the ether group facilitates the reactivity of tetrahydrofuran. Additionally, the difference in chemistry is observed via a more pronounced negative temperature coefficient (NTC) region from ~ 730 – 800 K, in which reactivity decreases with increasing temperature. This NTC behavior corresponds to the temperatures that are too high for

alkylperoxy chemistry to be favored, but also too low for rapid high-temperature chain-branching to dominate. NTC behavior indicates how complex the chemistry becomes in different temperature regimes and how the competition of reactions that unfold can affect ignition phenomena.

1.2 RESEACH APPROACHES TO COMBUSTION CHEMISTRY

Computational and experimental efforts are necessary for fundamental description of biofuel autoignition chemistry in order to understand and predict combustion phenomena that occur in complex molecules. The main purpose for the synergistic approach is to continue to build on the success of combustion science that has resulted in increased fuel efficiency by more than a factor of 2 over the last 20 years and in reducing particulate matter (PM) emissions to the point that exhaust PM accounts for only ~15% of transportation-derived emissions.[40,41] The overwhelming majority of emissions from the transportation sector are attributed to non-exhaust PM produced from brake dust and tear wear and are exacerbated due to the fact that electric cars are heavier on average than analogous internal combustion engine-powered cars.[42,43] Experimental results act as modeling targets to identify new and relevant pathways, and to highlight modeling deficiencies, while models can contribute to defining new experimental targets.

A summary of the how research efforts of the combustion community are related is depicted in **Figure 7**. First, a in a practical engine system, temperature and pressure can be measured against crank angle degree, which is the location of the piston during repeated 360° rotations in an engine (**Figure 7a**), which represents the heat evolution versus time, or the true ignition behavior. In a laboratory setting, this behavior is mimicked at various

stages of temperature and pressure by conducting well-controlled experiments, such as shock tubes, rapid compression machines (RCM), as well as flow reactors including photolytically-initiated reactors and jet-stirred reactors. **Figure 7b** shows an example of a pressure signal measured in shock tube experiments on 2-methyltetrahydrofuran by Uygun et al.[44] where ignition delay time is estimated by the steepest increase in pressure. In these experiments, global metrics of fuel behavior such as ignition delay time are plotted as a function of temperature or pressure (**Figure 7c**). Each condition has underlying chemistry that dictates the fuel behavior and can be inferred from experimental results (**Figure 7d**) using speciation measurements from flow reactors. From this fundamental understanding, chemical kinetics mechanisms can be built or improved upon (**Figure 7e**). If the mechanism is properly defined with elementary reactions, rates, and thermochemistry, it can be used in a numerical model that accounts for multi-phase physics and fluid dynamics to predict ignition behavior in a practical engine (**Figure 7e**). The work herein falls under the 'fundamental chemistry understanding' (**Figure 7d**) by collecting speciation measurements as a function of temperature and oxygen concentration for the purposes of expanding insight on tetrahydrofuran and specifically the effect of the ether functional group on low-temperature combustion pathways.

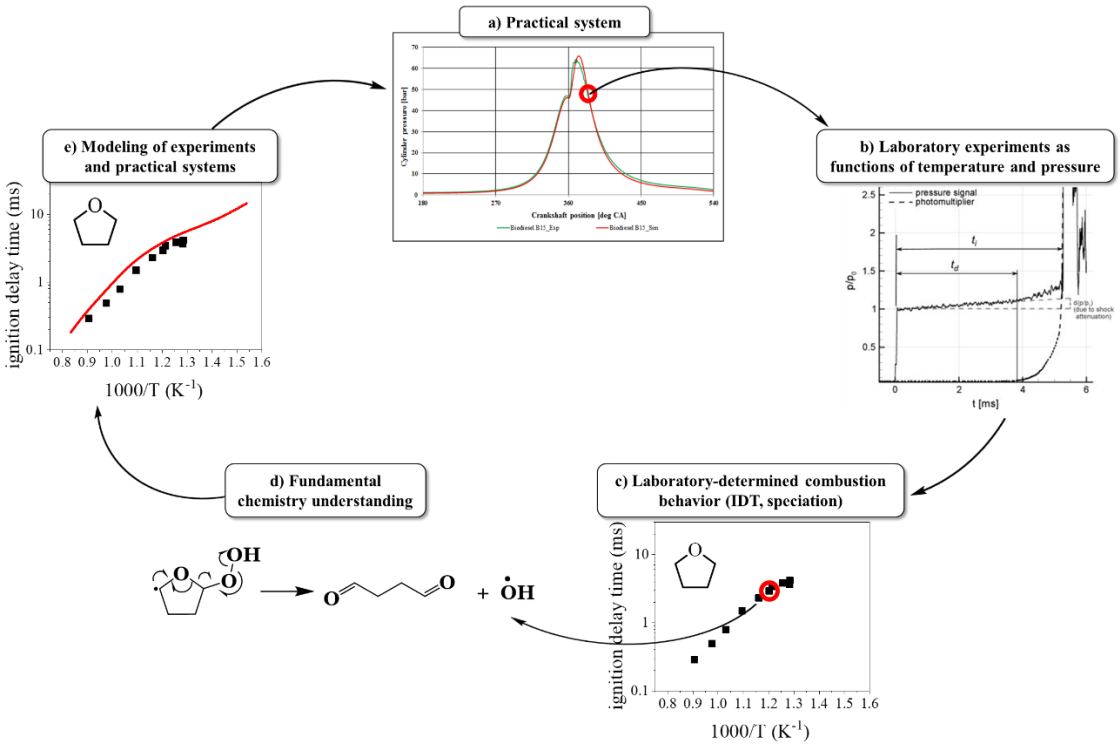

Figure 7. An overview of how experimental and modeling efforts work together to aid in the application of highly efficient, cleaner-burning engine technologies where practical engine performance (a) was measured by Aldhaidhawi et al.[45], shock tube experiments were completed by Uygun et al.[44], ignition delay time behavior was experimentally determined by Uygun et al.[44] from 800 – 1100 K and by Vanhove et al.[46] from 700 – 1000 K, and modeling of tetrahydrofuran behavior was performed by Fenard et al.[34]

1.2.1 Chemical kinetics modeling

In order to describe combustion chemistry, models aim to predict phenomena from a molecular level to application. Curran et al.[47] describes levels of computational work beginning with quantum mechanics and direct kinetic measurements, followed by construction and testing of chemical kinetics mechanisms, which depend on fuel structure and fundamental chemistry. The remaining levels described by Curran et al.[47] involve first reducing the chemistry to be used with computational fluid dynamics, then finally applying

models to real applications, such as fuel behavior in engines. The testing and use of chemical kinetics mechanisms is the primary role of modeling in this work.

A chemical kinetics mechanism consists of species and reactions involved in the combustion of a fuel and can be broken into thermodynamic and kinetic properties where the latter consists of elementary reactions and their rate constants.[47] Because chemical kinetics mechanisms aim to describe the combustion of a fuel entirely, they are often comprised of hundreds of species and thousands of reactions. For example, Fenard et al.[34] developed a chemical kinetics mechanism including low-temperature combustion pathways of tetrahydrofuran, which included 467 species and 2390 reactions. As fundamental chemistry is better understood and chemical kinetics mechanisms are updated or developed, the complexity grows as the number of species and reactions increases significantly. As an example, and in contrast to tetrahydrofuran, the most updated chemical kinetics mechanism for cyclopentane by Al Rashidi et al.[33] includes 33 species and 148 reactions.

While rate coefficients can be measured directly at some conditions, theoretical calculations via quantum chemistry are necessary due to the sheer number of reactions included in a mechanism and due to temperature and pressure ranges that fall beyond the scope of laboratory work.[26,48,49] In absence of theoretical calculations, two common methods for generating estimates of rate Arrhenius parameters are rate rules and structure-activity relationships.[26] Rate rules are based on assumptions that the rates of a certain elementary reaction are equal to that of a similar reaction type, fuel, or site.[50] For example, Curran et al.[51] chose the rate constant for H-abstraction by ȮH at secondary site of *n*-heptane to be identical to that for the same reaction of propane. Structure-activity

relationships are a type of estimation technique that relies solely on the molecular structure of the species involved in the reactions, where site-specific contributions determined for other molecules are summed to estimate a total rate coefficient.[52]

A numerical solver, such as ChemKin, is used to simulate experiments using chemical kinetics mechanisms and physical constraints of the experiment. For example, a jet-stirred reactor is modeled by the perfectly-stirred reactor module within ChemKin where inputs include temperature, pressure, initial mole fractions, and residence time. A series of equations representing mass and energy conservation (**Equations 1 and 2**, respectively) are solved, where F_x represents the mole flow rate at the inlet and outlet, $v_{x,y}$ is the stoichiometric coefficient of species *x* in reaction *y*, r_y is the rate of reaction *y*, V is the volume of the reactor, h_x is the enthalpy of formation of the species *x* at the inlet and outlet, and W is the reactor heat loss[53,54]. There are a number of outputs including speciation predictions and reaction pathway analyses, which will be discussed in further detail in Section 3.

$$F_x^{out} = F_x^{in} + \sum_y v_{x,y} r_y V \quad (1)$$

$$\sum_x F_x^{out} h_x^{out} + W = \sum_x F_x^{in} h_x^{in} \quad (2)$$

In order to accurately model a system, accurate thermochemistry, rate coefficients, and elementary reactions are necessary. To determine how accurate a model is, simulated predictions are compared to experimental results. Discrepancies are identified with specific modeling targets, which are then addressed, and re-evaluated against experimental results. It is important to note that when chemical kinetics models are developed they are often validated against specific or limited experimental data, which may introduce uncertainty. For example, Fenard et al.[34] developed a low-temperature sub-mechanism for

tetrahydrofuran combustion, in which they added an entirely new set of peroxy radical chemistry to a base chemical kinetics mechanism of the high-temperature combustion of tetrahydrofuran by Tran et al.[55] Fenard et al.[34] chose to tailor their mechanism to successfully predict ignition delay time data and jet-stirred reactor data where some rate coefficients were adjusted in order to better predict these data sets. However doing so accurately, as stated by Fenard et al.[34] came at the detriment of rapid compression machine predictions.

In addition, other errors may be introduced in current chemical kinetics mechanism development practices. One of the most common is mechanism truncation error, which is uncertainty that results from missing or incomplete chemistry (**Figure 8b**). For example, in chemical kinetics mechanisms of *n*-butane combustion, rate coefficients of the formation of 2,3-dimethyloxirane are reported.[56] However, *cis*- and *trans*- stereoisomers are not distinguished and the consumption pathways of these intermediates are not described, causing mechanism truncation error in the chemical kinetics mechanism of *n*-butane.[57] Subsequent work by Hartness et al.[58] showed significant sensitivity of model predictions for *n*-butane kinetics to unimolecular reactions of ȮOOH. In order to aid this effort, Doner et al.[57] conducted experiments and computations to uncover new consumption pathways of 2,3-dimethyloxirane and examine isomer-dependence.

Another common practice that may introduce uncertainty is a lumping procedure in which multi-step elementary reactions are abbreviated into simplified global reactions that neglect the formation of intermediates, such as combining a reaction that follows four steps into a single step (**Figure 8c**).[59] Lumping decreases the size of mechanisms, since it decreases the number of species, which has the benefit of simplifying complex systems

with a large number of species and reactions in order to reduce the dimensionality to a smaller number of components easing computational load.[59–61] Yet, in contrast with mechanism truncation error where the chemistry is unknown, the purpose of lumping is to simplify a complicated system where the rates of elementary reactions are unknown. One example of lumping occurred by Wu et al.[62] where although a series of elementary reaction pathways were proposed for O_2-addition to 2,3-dihydrofuranyl radical, thermal and kinetic data for these reactions were absent so a lumping procedure was adopted within the chemical kinetics mechanism.

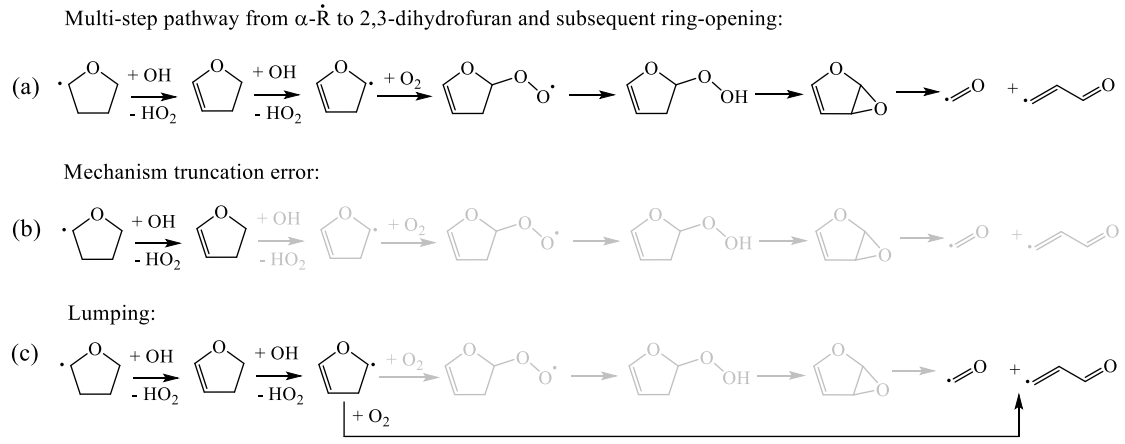

Figure 8. Multi-step pathway from α-Ṙ to 2,3-dihydrofuran, which can undergo subsequent H-abstraction, O_2-addition, and ring opening (a). An example of mechanism truncation error is where 2,3-dihydrofuranyl O_2-addition and ring-opening consumption pathways are unknown and therefore omitted from the chemical kinetics mechanism (b). Lumping is where although these pathways are known, they are abbreviated into one step to simplify the mechanism by reducing the number of species and reactions (c).

1.2.2 Experimental goals and challenges

Within the context of this work, the experimental goal is to measure species profiles of intermediates and products relevant to the low-temperature combustion pathways outlined in **Figure 5a**. Speciation data provides direct insight into ignition chemistry and combustion behavior as depicted in **Figure 7** by observing trends in speciation, connections to mechanisms can be made, which will deepen the understanding of ȮOOH chemistry. Additionally, model predictions of gas-phase intermediates using two mechanisms of Fenard et al.[34] and Wu et al.[62] are be compared to experimental species profiles to contribute to model development. Specifically, discrepancies between model predictions and experimental results are highlighted in which causes are identified, if possible, in order to provide suggestions on what areas within the chemical kinetics mechanism require attention to improve agreement between predictions and experiments. For example, it is possible to uncover new mechanisms, redefine certain pathways as important or unimportant, or determine the influence of temperature, pressure, or [O_2].

One experimental challenge in combustion research has been the isolation and detection of certain isomers, particularly multi-functional species and stereoisomers. For example, the identification of isomers in combustion experiments that rely exclusively on mass spectrometry is often unreliable as mass spectra are often indistinguishable for isomers (see Section 2.3.2).[46,63,64] Isomer-resolution is important as ȮOOH unimolecular decomposition produces numerous constitutional isomers and stereoisomers (**Figure 5c**). In order to infer specific mechanistic information, isomers must be resolved. For the work herein, the absorption spectroscopy technique used can distinguish isomers due to the ability to probe unique electronic transitions (see Section 2.2 and **Figure 15**). One example

that will be discussed in Section 4 is that of butanedial, a β-scission decomposition product that can only be attributed to α,α-ȮOOH of tetrahydrofuran, in which the –OOH group and radical are adjacent to the ether group (α-position) and on opposing sides (**Figure 9**). The detection and quantification of butanedial allows for a direct probe on α,α'-ȮOOH pathways where the influence of temperature and [O_2] can be studied via butanedial speciation. Additionally, model predictions of butanedial can be compared to experimental species profiles to gain insight on how chemical kinetics mechanisms respond to temperature and [O_2].

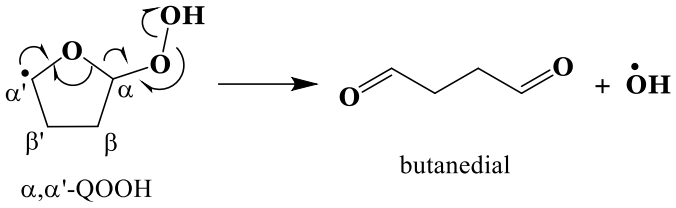

Figure 9. Pathway for the formation of butanedial from α,α'- ȮOOH.

1.2.3 Focus of this work

Understanding tetrahydrofuran oxidation is important for several reasons, including the potential as a next-generation biofuel and because the base molecular structure is common to other biofuels, such as 2,5-dimethyltetrahydrofuran and 2-methyltetrahydrofuran, among others.[65,66] In addition, since tetrahydrofuran is an intermediate of *n*-butane combustion, obtaining fundamental insight on reaction pathways and species concentrations, particularly from reactions involving hydroperoxy-butyl, enables high-fidelity computational modeling of not only tetrahydrofuran, but also *n*-butane low-temperature combustion and *n*-alkanes in general.[56,67–69]

Several speciation studies on low-temperature oxidation of tetrahydrofuran exist.[46,70–74] Vanhove et al.[46] conducted speciation experiments using a jet-stirred reactor (JSR) and a rapid compression machine (RCM) that provided a substantial basis upon which to understand tetrahydrofuran combustion. However, several species were unable to be resolved including several at mass 86, which is the mass of carbonyl, cyclic ether, and several β-scission products of tetrahydrofuran ȮOOH decomposition. Time-resolved, multiplexed photoionization mass spectrometry (MPIMS) experiments were conducted by Antonov et al.[70] at 10 – 2000 Torr and 400 – 700 K. In MPIMS experiments, the reaction is photolytically initiated with an excimer laser and the reaction stream is expanded in a vacuum chamber where it is crossed with a tunable synchrotron radiation beam (8.2 – 11.2 eV) for ionization before detection in a time-of-flight mass spectrometer. Chain-inhibiting reactions were dominant, particularly that of 2,3-dihydrofuran formation in part due to the favorability of the ether group. However, previously unidentified species were detected including 2-hydroperoxy-2,3-dihydrofuran (formed coincident with HOȮ) and a ketohydroperoxide species. Hansen et al.[72] utilized a JSR and photoionization mass spectrometry at 1 atm and reported the first isomer-resolved detection of ketohydroperoxides. Belhadj et al.[73] conducted JSR experiments from 550 – 620 K and focused on qualitative detection of products from successive O_2-addition, including ketodihydroperoxides, formed via third-O_2-addition, hydroperoxides, dihydroperoxides, diols, and dicarbonyls. The latter species may arise from ketohydroperoxide decomposition. Lockwood and Labbe[75] computed potential energy surfaces for ketohydroperoxide formation from O_2 + β-tetrahydrofuranyl and concluded that deficiencies in model predictions in Hansen et al.[72] may arise from uncertainty in rates for

β-ROȮ → ȮOOH and to branching fractions in the initiation step of tetrahydrofuran. Additionally, Fenard et al.[34] developed the first detailed chemical kinetics mechanism that included low-temperature combustion chemistry for tetrahydrofuran. Using Fenard et al.[34] as a base, Wu et al.[62] subsequently developed revised sub-mechanisms for 2,3-dihydrofuran and furan. Further details about Fenard et al.[34] and Wu et al.[62] mechanisms are described in Section 3.2.

Because isomer resolution remains a challenge in combustion experiments and is imperative to the experimental work conducted in the Rotavera laboratory for this work and beyond, the first main objective of the work herein is to optimize the analytical diagnostics used to identify and quantify combustion intermediates and products. This consists of gas-chromatography, mass-spectrometry, thermal conductivity detection, and absorption spectroscopy. Additionally, as this is the first work of this type within the Rotavera laboratory, the quantification procedure is developed and optimized to be used in this work and all future work. See Chapter 2 for extensive detail on the progress of these objectives.

The main scientific goal of this work is to probe O_2-dependence of tetrahydrofuran to gain new insight to tetrahydrofuran combustion and provide new modeling targets to the computation community. While there has been prior work on speciation measurements as described previously, the dependence on O_2 has not been studied. By changing the concentration of O_2, the balance of ȮOOH reactions can be studied as the competition that unfolds is dependent on O_2 where it is hypothesized that with increasing O_2, second-O_2 addition out competes unimolecular decomposition. Isomer-resolved speciation experiments are conducted where in comparison to cyclopentane, the hydrocarbon

equivalent to tetrahydrofuran, changes in combustion behavior observed via differences in low-temperature combustion pathways can be attributed to the ether functional group. Specifically, this work will help contribute to understanding ether group chemistry, provide isomer-resolved species profiles that have been challenging for others to measure, and identify areas of improvement in chemical kinetics mechanisms.

CHAPTER 2

EXPERIMENTAL APPROACH

2.1 JET-STIRRED REACTOR FACILITY

To conduct low-temperature speciation measurements for this work, a jet-stirred reactor[76] was used as it has the advantage of precise control over experimental conditions, namely temperature, pressure, and residence time, i.e. the time that gases spend in the reactor volume. Jet-stirred reactors are spherical continuous-stirred reactors made of quartz to withstand high temperatures and prevent surface reactions, and have four nozzles in the main reaction volume and with cylindrical tubular additions extending in inlet and outlet directions (**Figure 10a**). Reactants are flowed through the reactor at low-temperature combustion conditions. The composition of products is determined with respect to temperature, pressure, initial fuel concentration, oxygen concentration, and residence time, where this analysis is used to infer information about elementary reactions and rates within the combustion mechanism. A summary schematic is shown in **Figure 11**.

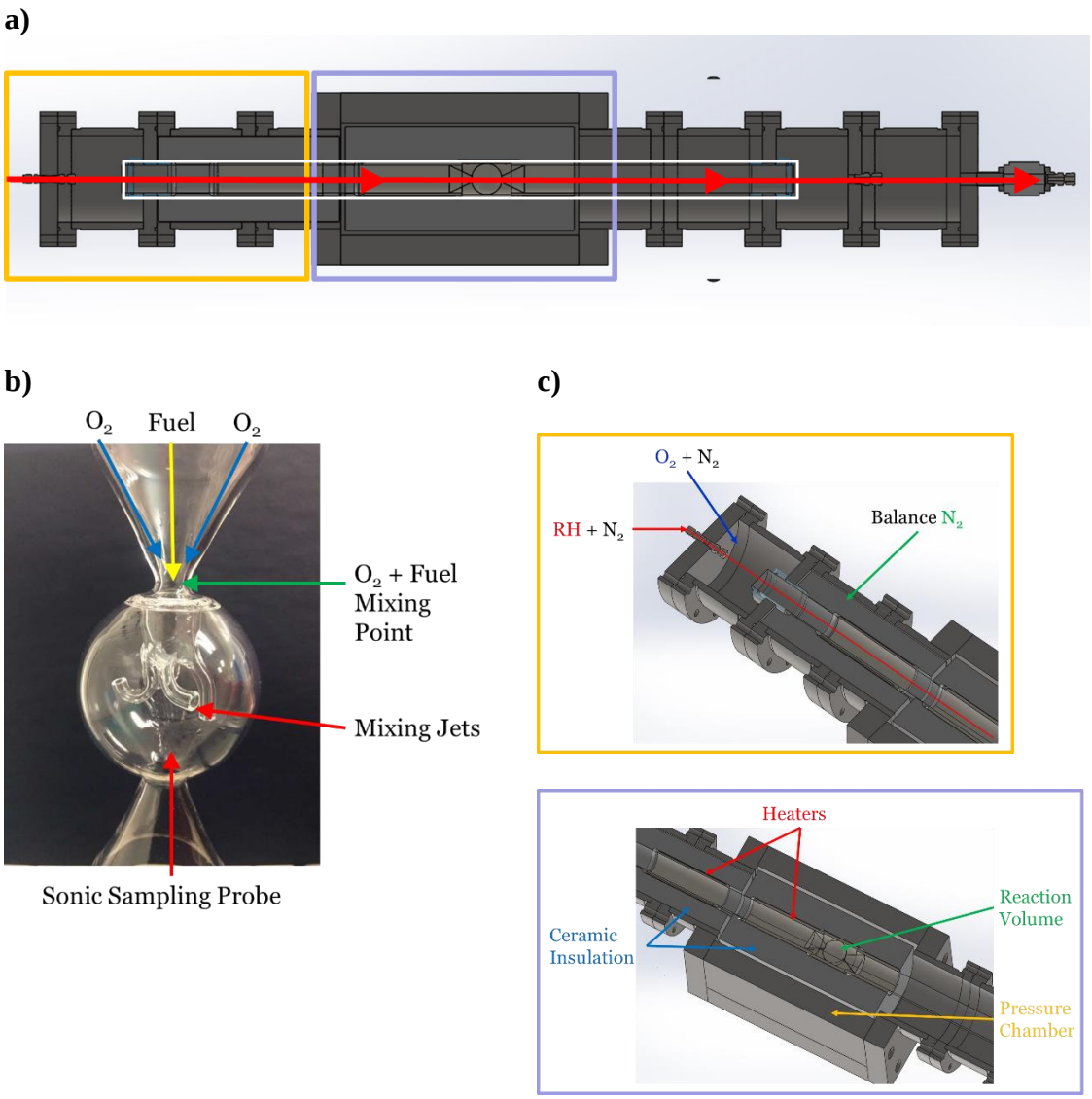

Figure 10. Jet-stirred reactor and housing unit used for the experiments herein with a top down bisected view where the quartz jet-stirred reactor is highlighted in white and direction of flow is indicated with red arrows (a). An image of the reaction volume is shown in (b) where turbulent mixing is induced in the conical region prior to the jets and within the reaction volume. In (c), a closer view of the inlet section is outlined in yellow while the main reaction volume section is outlined in purple.

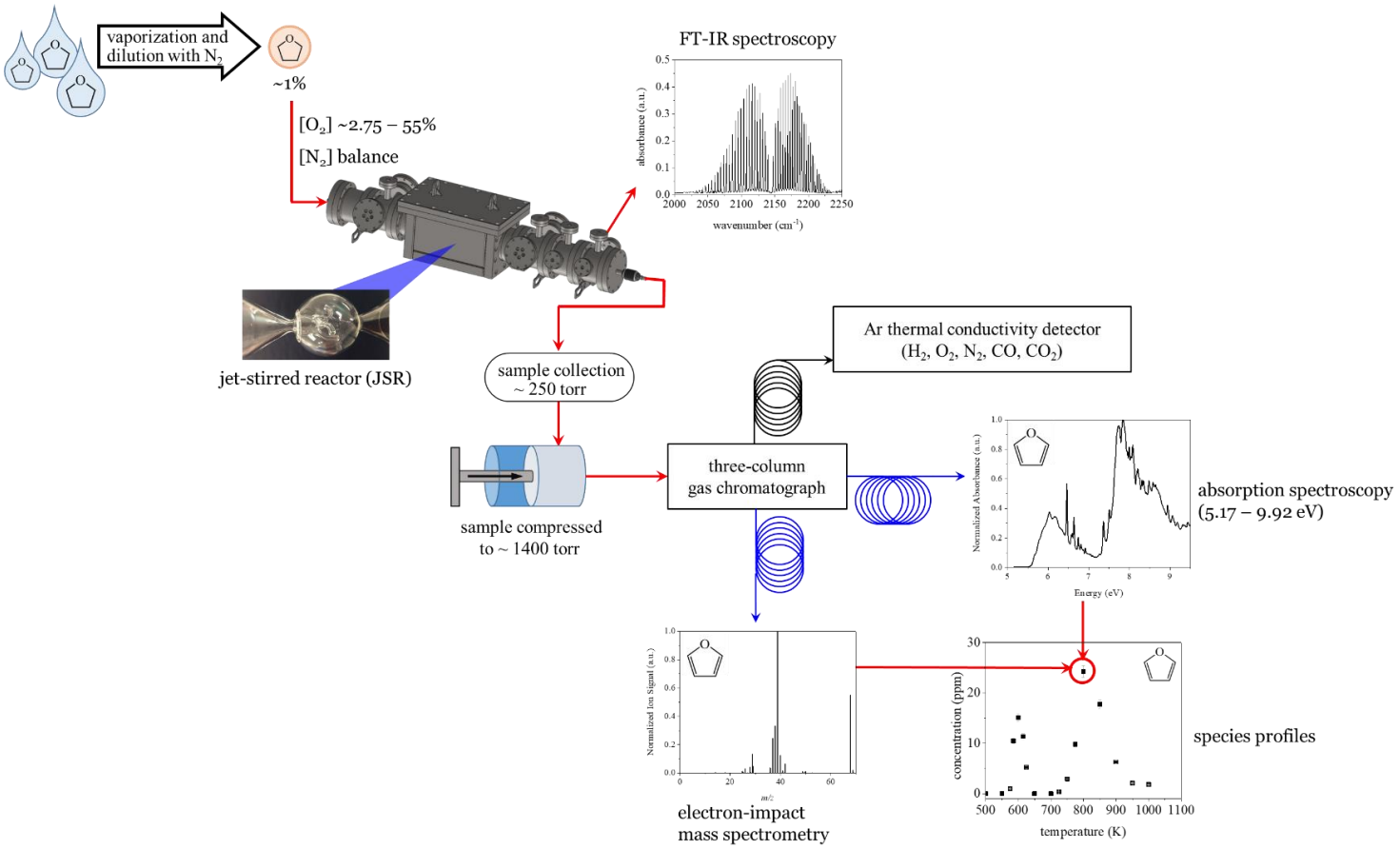

Figure 11. Schematic of full experimental setup where fuel (tetrahydrofuran) is first vaporized and diluted to ~ 1%. Fuel is introduced to jet-stirred reactor with O_2 and N_2 where reaction occurs inside central spherical reaction volume at controlled temperature, pressure, and residence time. Online analysis by FTIR indicates when reaction is at steady state and can be sampled. A sample is collected in quartz tanks at low pressure and compressed to ~ 1400 Torr to be introduced to a three-column gas chromatograph for separation and analysis by thermal conductivity detector, vacuum ultra-violet spectroscopy, and mass spectrometry simultaneously. Identification and quantification is denoted by a single point on a species profile and represents the conditions at which the sample was collected.

2.1.1 Principles of jet-stirred reactors

Jet-stirred reactors operate at steady state and are designed to turbulently mix gases, which ensures homogeneity of temperature and species concentration allowing for experimental repeatability. Turbulent mixing is facilitated within a jet-stirred reactor by two means. First, turbulence is induced in the region upstream of the nozzles, where the cylindrical tube converges to form a cone. Second, within the spherical reactor, four nozzles pointing in alternating directions produce turbulent jets (**Figure 10b**).

The primary advantage of jet-stirred reactors for speciation measurements is that due to the efficient mixing, the composition of the outlet gas is identical to that within the reactor volume. This allows for direct measurement of closed-shell reaction intermediates and products over a range of conditions. However, the sampling process prevents open-shell intermediates from being detected. Another disadvantage is that there is no time history information for individual species as is typical for other experiments including shock tubes and multiplexed photoionization mass spectrometry (MPIMS).[37,44] Time is still a variable in the experiment, however, in the form of residence time.

In a given experiment, fuel diluted to ~1% with inert gas is introduced to the reactor through a capillary that centrally sits within the jet-stirred reactor. Oxygen and nitrogen are supplied to the reactor in the area surrounding the capillary and a balance flow of N_2 surrounds the exterior of the reactor creating a negligible pressure differential (**Figure 10c**), which enables high-pressure experiments. In the conical region upstream of the jets, fuel and gases mix for the first time facilitating turbulence. The stream passes through the jets within the reaction volume, providing a second source of turbulent mixing. The entire region is heated by vacuum-brazed Inconel heating elements woven into a shell of Inconel

600, an alloy of nickel, iron, and chromium, which closely surrounds the quartz reactor; separation between the surface of the quartz and the Inconel heating element is ~2-3 mm. Inconel 600 was chosen as it has a high melting point to withstand the experimental temperature range and a high thermal conductivity to ensure homogenous heating of the entire element. The reactor and heating elements are shrouded with ceramic insulation to prevent heat loss and reduce dead volume in the stainless steel housing, which would increase the amount of gas needed to pressurize the system.

2.1.2 Fuel delivery inlet system

In order to supply fuel to the jet-stirred reactor, a fuel delivery system is used comprised of a custom syringe and Bronkhorst Vapor Delivery Module (**Figure 12**). The purpose of this two-part fuel delivery inlet system is to supply liquid fuel at a controllable and consistent gas-phase concentration to the jet-stirred reactor. The custom syringe consists of a 200-mL steel cylinder with a piston that is modulated via balance N_2 gas held at a constant pressure. This supplies liquid fuel to the Vapor Delivery Module, which contains a Coriolis liquid flow meter and a N_2-calibrated gas flow controller that supply liquid fuel and carrier gas, respectively, to a Control Evaporation Mixing (CEM) system where total evaporation occurs. This system is unique as the CEM improves upon limitations of traditional fuel delivery systems, namely bubblers, which rely on the vapor pressure of the fuel. Rather, the CEM is robust as it can accommodate fuels of different vapor pressures with accuracies to 0.2% of the total flow, which ranges from 0.5 – 5 grams per hour (g/h).

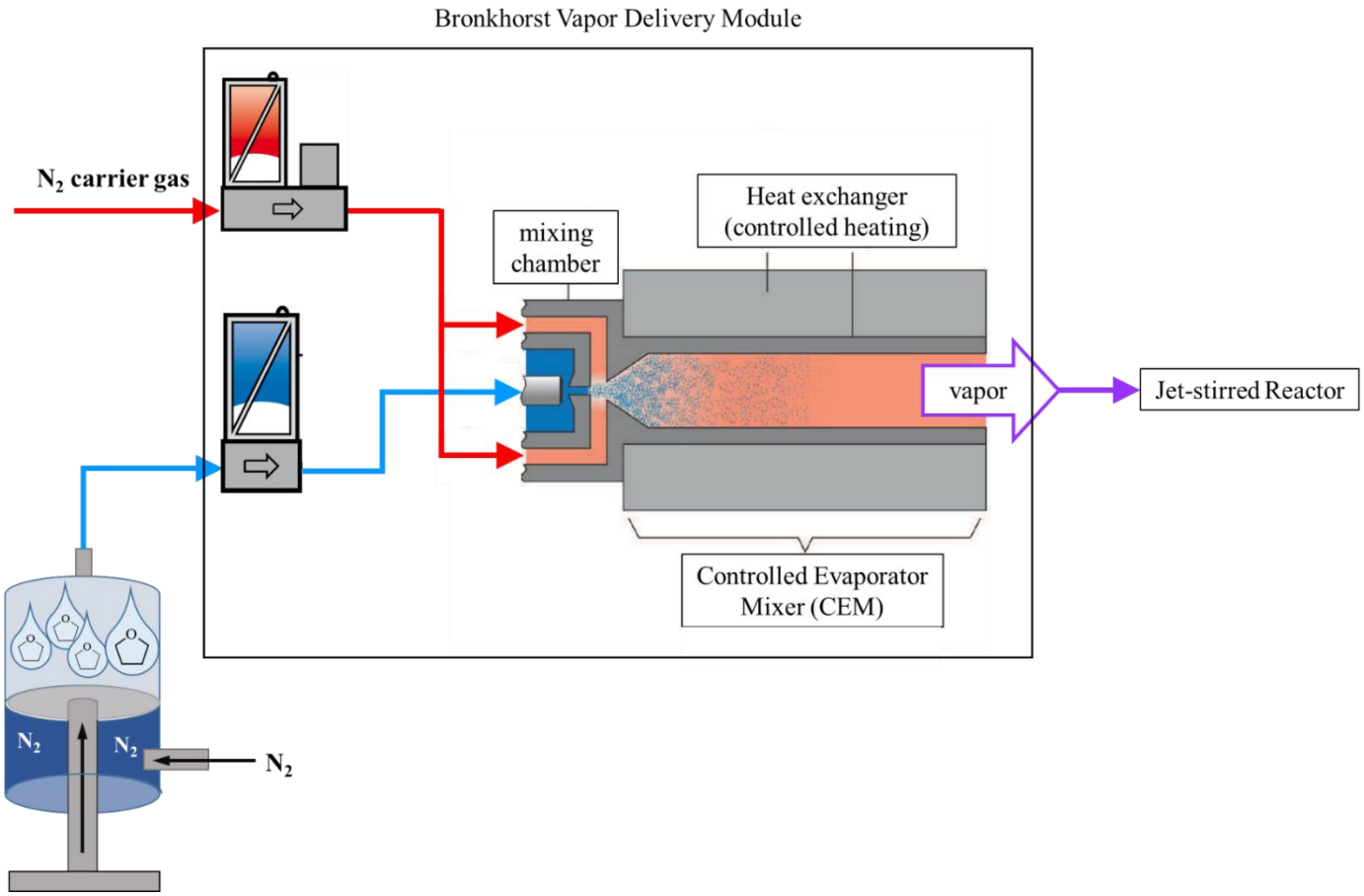

Figure 12. Schematic of fuel inlet system consisting of custom syringe that maintains ~ 300 psi of pressure on the backend to provide a consistent flow of liquid fuel to the Bronkhorst Vapor Delivery Module. Liquid fuel and N_2 carrier gas enter the VDM through mass flow controllers which deliver a set flow rate of each species to a mixing chamber where fuel is diluted to a controlled concentration. Once mixed, diluted fuel flows through the Controlled Evaporator Mixer (CEM) where heating and evaporation occurs, ultimately delivering fuel vapor at a controlled concentration to the jet-stirred reactor.

2.1.3 Sample extraction and collection method

In order to determine the relationship between chemical kinetics mechanisms and combustion conditions, samples that are composed of those closed-shell reaction intermediates present at the time of sampling are taken incrementally at each set of conditions. For example, experimental conditions may have a reactor temperature of 800 K, a pressure of 1 atm, and a residence time of 2 seconds. To capture this set of conditions and in order to not perturb the reaction with the sampling process, only a portion of the contents of the reaction volume are quenched and collected. The contents, which are in the gas phase, are analyzed, where the composition and amount of species are derived from that specific condition. Therefore, by changing the conditions incrementally and measuring the products, species profiles can be determined, which provide insight on which pathways are occurring, to what degree, and at which conditions (**Figure 11**). Species profiles in the present context refers to concentrations of measured species as they relate to temperature, pressure, or O_2 concentration.

To quench the reaction, a sonic sampling probe is situated at the outlet side of the reaction sphere. Sonic sampling is a common technique in which gas flow is forced through such a small orifice that sonic flow occurs and there is a rapid reduction in temperature leading to quenching, called expansion cooling[77]. The probe is made of fused quartz and has a 500-µm orifice. A linear motion thimble is attached to the probe outside of the jet-stirred reactor housing and allows the position of the probe to be adjusted along the longitudinal axis of the reaction volume with accuracy of 10-µm. During experimental campaigns, the position of the probe was noted and never moved unless for necessary cleaning, after which it was returned to its original denoted position.

2.1.4. Temperature homogeneity testing

Temperature homogeneity is important because as described by the modified Arrhenius equation, reaction rate is exponentially dependent on temperature (**Equation 3**). There are features in place to minimize thermal gradients such as the use of preheaters designed to gradually heat cold gases upon entry to the jet-stirred reactor. There are two zones of preheaters; an external preheater, outside of the jet-stirred reactor housing, and an internal preheater, located between the inlet and the reaction volume. Additionally, fuel is diluted in N_2 to ~1% prior to reaction to prevent temperature release upon combustion, which would also cause gradients. The reaction volume is heated from fitted insulted heating elements from above and below.

$$k = AT^n e^{\frac{-E_a}{RT}} \quad (3)$$

Temperature homogeneity of the jet-stirred reactor was tested where the gradient was measured to range from 4.4 – 11.1 K, inside the reaction volume where the higher the nominal temperature, the greater the gradient. To test temperature homogeneity, a K-type bare-wire thermocouple was fed through a quartz tube and situated within the reaction volume to take measurements of temperature using N_2. Temperatures were measured in 25 K increments from 600 – 800 K, and at three sample probe locations where the distance was 0, 1.5, and 3 cm from the jets as measured by the linear motion thimble (**Figure 13**). One hour was used as the standard equilibration time between changing set points. The measured temperature was compared to the temperature set-point and the gradient was determined. Between the minimum and maximum distances, the temperature gradient was

measured to be 4.4 K at 600 K and 11.1 K at 800 K. For experiments, the sample probe was situated at 1.5 cm.

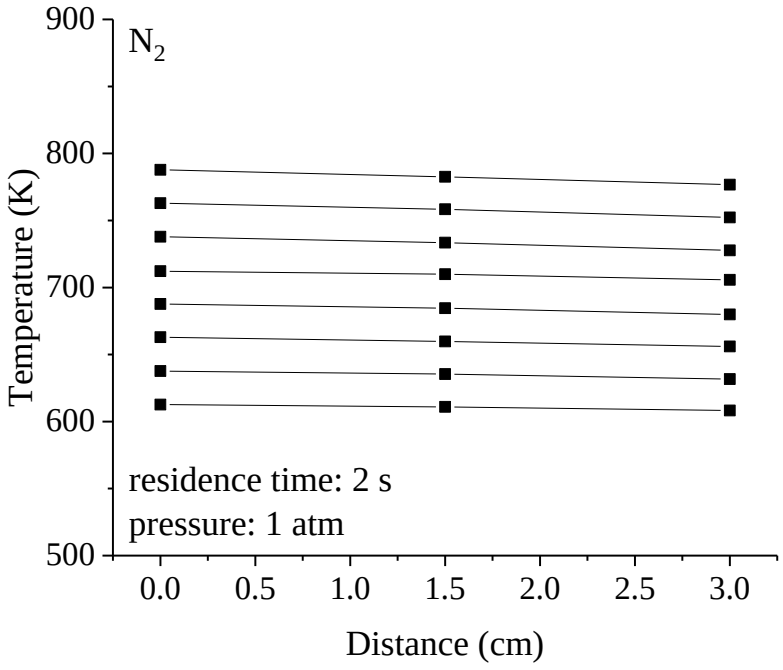

Figure 13. Temperature measured at 25 K increments from 600 – 800 K across three locations within the reaction volume as denoted by distance from the jets.

2.1.5 Steady state system and FTIR analysis

Because jet-stirred reactor experiments are conducted at steady state, it is worth noting the influence this has on the detection of low-temperature combustion intermediates. Namely, at steady state conditions, the quantitative amount of a given species is representative of both its formation and consumption. For example, at 615 K and an O_2 concentration of $0.74 \cdot 10^{18}$ molecules $\cdot$ cm^{-3} ($\phi = 1$), 2,3-dihydrofuran was quantified to be present at ~ 110 ppm. This concentration not only represents how much 2,3-dihydrofuran was formed, but also any that had been consumed.

Fourier Transform Infrared (FTIR) spectroscopy was used to determine when the reaction was at steady state to know at which point a sample should be collected. It was assumed that at steady state, there would be an unchanging composition and concentration of species continuously flowing from the reactor. This flow was directed online to an FTIR instrument, which was constantly collecting absorption data. Once a plateau in signal was observed, a sample was collected. After changing combustion conditions or after beginning reactive flow at the start of the day, it took approximately 30 minutes to an hour to reach steady state flow. Because the reaction flow consisted of ~15 – 25 species, unique spectral features could not be distinguished and therefore, FTIR was not used for identification or quantification purposes.

2.2 OFFLINE ANALYTICAL METHODS

Once samples had been collected from the jet-stirred reactor, they were analyzed via a suite of analytical diagnostics, which have the capability to resolve constitutional isomers and stereoisomers of gas-phase intermediates for quantification. The main analytical process is outlined in **Figure 14**, where first the sample is introduced to a gas-chromatograph where separation was achieved using two identical gas-chromatograph (GC) columns maintained at 40°C for 5 minutes, increased to 110°C over a period of 14 minutes and maintained for 5 minutes, then increased to 280°C over a period of 8.5 minutes and maintained for 5 minutes. Each column independently supplies sample to an electron-impact mass spectrometer (EI-MS), which measures signal as a function of mass-to-charge (*m/z*), and a vacuum ultraviolet (VUV) absorption cell, which measures absorption spectra from 5.167 – 9.920 eV.[78–80] VUV absorption spectroscopy probes electronic transitions

where $\sigma \rightarrow \sigma^*$, $n \rightarrow \sigma^*$, $\pi \rightarrow \pi^*$, and $n \rightarrow \pi^*$ are accessible (**Figure 15**). The ability to probe transitions for σ excitation is unique to the aforementioned energy range and allows for distinguished absorption spectra for hydrocarbons, which facilitates isomer-resolution, whereas typical UV-Visible spectroscopy is limited to ~ 6.2 eV, which is not enough energy to facilitate σ excitation[78]. The GC is also equipped with a thermal conductivity detector (TCD) that measures small species including He, O_2, CO, CO_2, methane, and N_2.

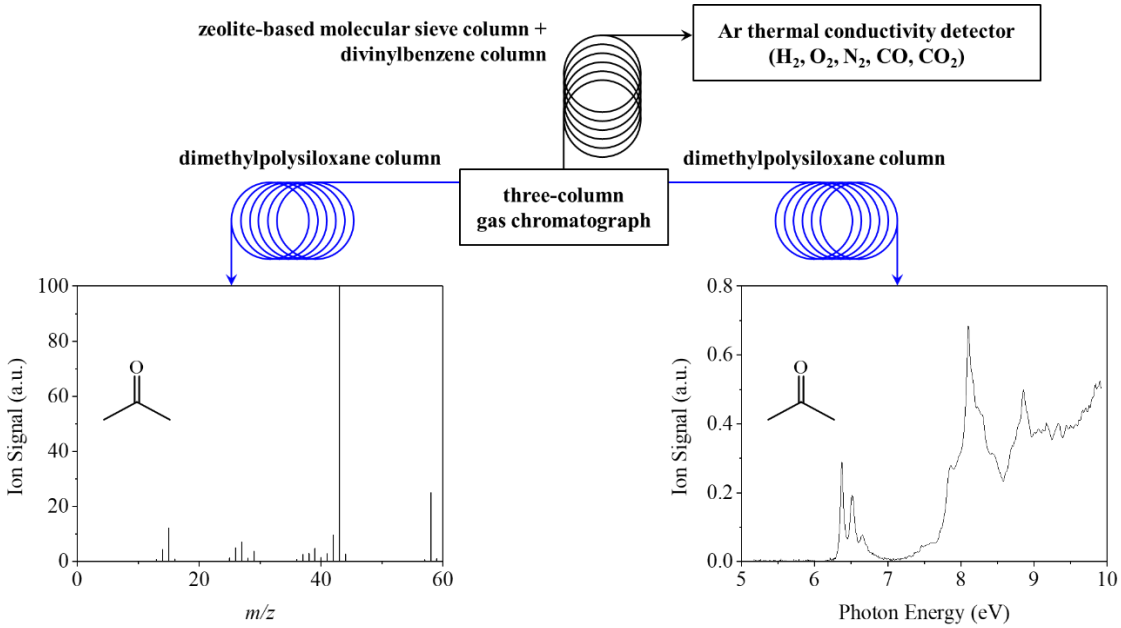

Figure 14. Two identical GC columns independently supply gas-phase sample to EI-MS and VUV absorption spectrometer. A third column supplies a thermal conductivity detector.

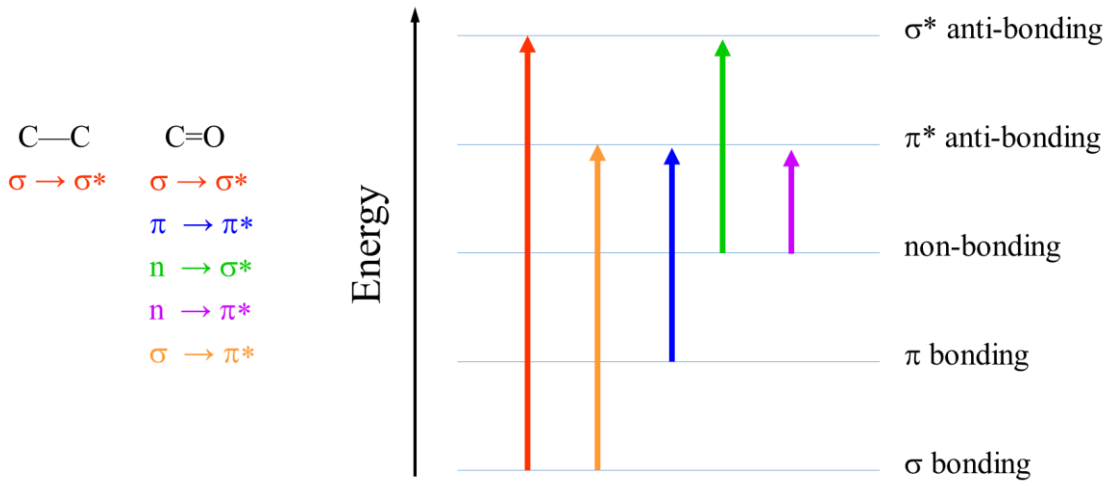

Figure 15. Accessible electronic transitions where a transitions available to representative C-C and C=O bonds are denoted by color and from left to right: $\sigma \rightarrow \sigma^*$ (red), $\sigma \rightarrow \pi^*$ (orange), $\pi \rightarrow \pi^*$ (blue), $n \rightarrow \sigma^*$ (green), and $n \rightarrow \pi^*$ (purple).

In addition to the diagnostics discussed above, an additional piece of equipment was developed and used in conjunction. Because sonic sampling technique keeps samples at low pressures, a custom compression cell was utilized to compress gas samples to greater than atmospheric pressure. This was necessary as the inlet of the gas-chromatograph required a positive pressure to collect sample for measurement. The compression cell is a simple piston controlled via an actuator and regulated to a pressure of 2 atm. See **Figure 11** for reference.

Details of instruments and techniques are discussed herein. The two identical columns are Agilent PONA type (paraffins, olefins, naphthalenes, and aromatics) 100 m in length, with 250 μm inner diameter, and a 0.5 μm film thickness. The EI-MS of 70 eV electrons is equipped with single, heated gold-plated quartz quadrupole and a triple-axis

detector. The detection limit is <1 part-per-million (ppm) and the mass resolution is 1 amu with a mass accuracy of ± 0.005.

The VUV absorption instrument operates as follows. White light is supplied from a deuterium lamp and is directed through the flow cell using high-reflectivity mirrors positioned at the inlet and outlet. The outlet mirror directs the light to a diffraction grating, which supplies high-resolution separation (<4 meV) onto a CCD detector producing an output voltage corresponding to a photon energy. The output signal is processed via an A/D converter and sent to a data-acquisition system for post-processing. The optical environment external to the absorption cell is maintained with N_2 to purge O_2 and H_2O from the system, as both are strong absorbers at ~10^{-18} cm^{-2} (at 8.7 eV) and ~10^{-17} cm^{-2} (at 9.7 eV), respectively. While N_2 does absorb slightly, the maximum absorbance over the energy range at which measurements occur is negligible (~10^{-21} cm^{-2}). Prior to each absorption measurement, a reference scan measuring background absorbance and a darks scan where the lamp is blocked are collected to enable background subtraction and to capture incident light (I_0), respectively. Ambient gas flow of N_2 supplied by the GC column is continuous and included within all background scans. Detection limits are <1 ppm. To quantify absorbance as a function of photon energy, **Equation 4** was utilized where I_0 corresponds to the incident light and I(E) is the residual intensity of the white light after passing through the flow cell. The absorption cross-section was quantified using the Beer-Lambert law, which includes the flow cell path length in cm (L) and the gas-phase number density of absorbing species (N) in molecules cm^{-3} (**Equation 5**).

$$A(E) = log\frac{I_0}{I(E)} \quad (4)$$

$$\sigma(E) = A(E)\ln(10)(NL)^{-1} \quad (5)$$

Specific method development for each instrument will be discussed in detail in Section 2.3.

This suite of diagnostics provided a multi-dimensional set of data shown in **Figure 16** including time-resolved chromatographs corresponding to each detector, mass spectra, TCD, and VUV absorption spectra, which were used in conjunction with reference measurements to identify and quantify detected species from jet-stirred reactor experiments.

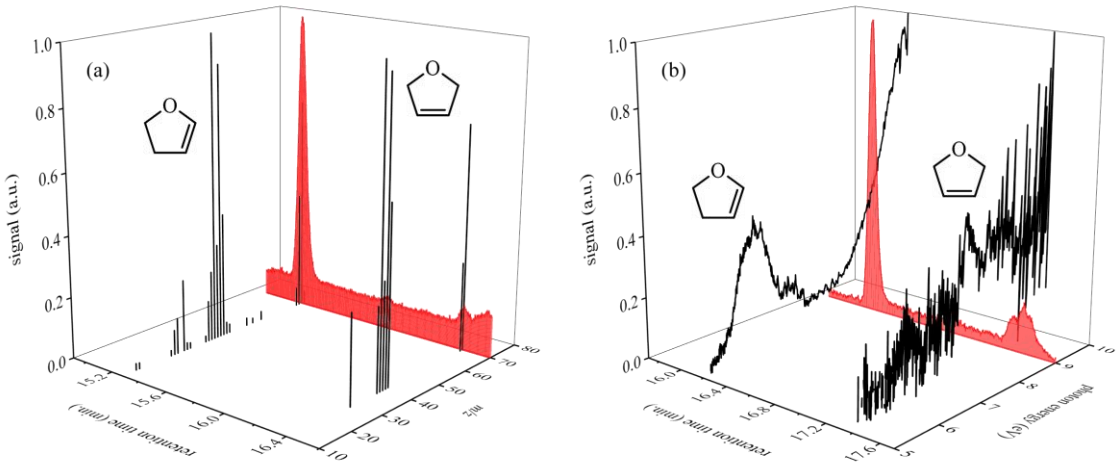

Figure 16. Electron-impact mass spectra (a) and vacuum ultraviolet absorption spectra (b) with corresponding chromatograms for 2,3-dihydrofuran and 2,5-dihydrofuran from tetrahydrofuran oxidation.

2.2.1 Reference measurements

Reference measurements were collected of ~150 predicted species relevant to the work herein and other ongoing combustion projects. Binary mixtures of a given species diluted in N_2 were made manometrically at 2000 ppm when possible given vapor pressure constraints. High-purity liquid chemicals were degassed using the freeze-pump-thaw method in which a reservoir of the liquid vacuum-sealed to a manifold is frozen using liquid N_2 and the remaining gas is pumped out using an attached vacuum pump. This

ensures all gases are removed from the manifold system so that the only the vapor phase of the chemical is present. The gas-phase was introduced into a heated stainless-steel cylinder at a pressure ~ 8 Torr, then diluted with N_2 to 2000 ppm. Binary mixtures were statically mixed for at least 1 hour. Finally, each mixture was supplied to the GC-EIMS-VUV to measure multi-dimensional data (**Figure 16**) to serve as calibration standard. VUV spectra uncertainties are highest in energy regions where the measured absorbance falls below 2% of the maximum absorbance.[78–80]

An example set of absorption cross-section references of cyclopentane, cyclopentene, and tetrahydrofuran are shown in **Figure 17** and highlight the effects of π bonding and an ether functional group on measured electronic transitions. The π-bond in cyclopentene enables low energy $\pi \rightarrow \pi^*$ transitions, which is observed as an electronic excitation at ~ 6.9 eV. Specifically, the π-bond decreases the gap between the highest occupied molecular orbital (HOMO) and lowest unoccupied molecular orbital (LUMO), facilitating $\pi \rightarrow \pi^*$ excitation.[78–80] Furthermore, the succession of narrow bands following the peak at ~ 6.9 eV can likely be attributed to vibrational excitations. Tetrahydrofuran is a weaker absorber as evidenced by the reduced absorption cross-section in comparison to cyclopentene. Because of the ether group in tetrahydrofuran, non-bonding transitions are accessible. The peak at ~ 6.5 eV is attributed to an $n \rightarrow \sigma^*$ electronic transition.[78–80] In contrast, because cyclopentane only has σ bonds, only $\sigma \rightarrow \sigma^*$ transitions are possible, which is why absorption is only strong at high energies required to enable that electronic transition.

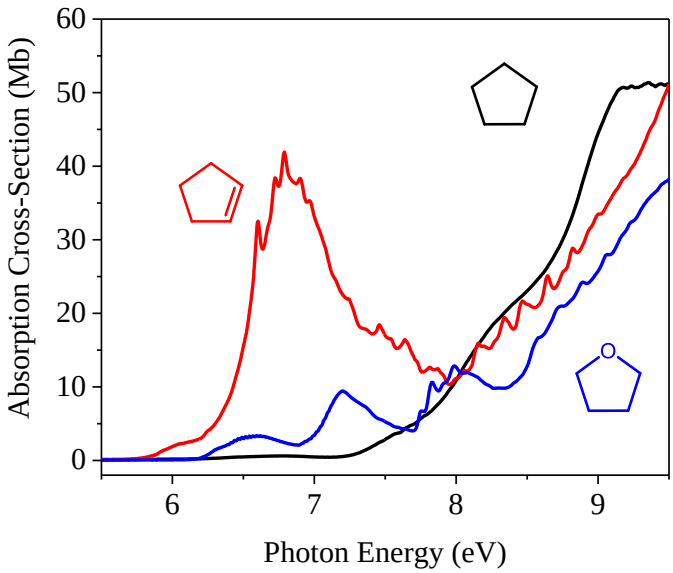

Figure 17. Absorption cross-section measurements of cyclopentane (black), cyclopentene (red), and tetrahydrofuran (blue).

2.3 DEVELOPMENT OF IDENTIFICATION AND QUANTIFICATION TECHNIQUES

2.3.1 Gas chromatography method development

Peak separation was achieved using an optimized temperature ramping profile in which the initial temperature of 40°C is held for 5 minutes, ramped to 110°C at a rate of 5°C per minute, held for 5 minutes, ramped to 280°C at a rate of 20°C per minute, and finally held for 5 minutes (**Figure 18**). This method was optimized by multiple parameters including temperature ramp rate, hold time, temperature set point, and number of temperature ramping steps.

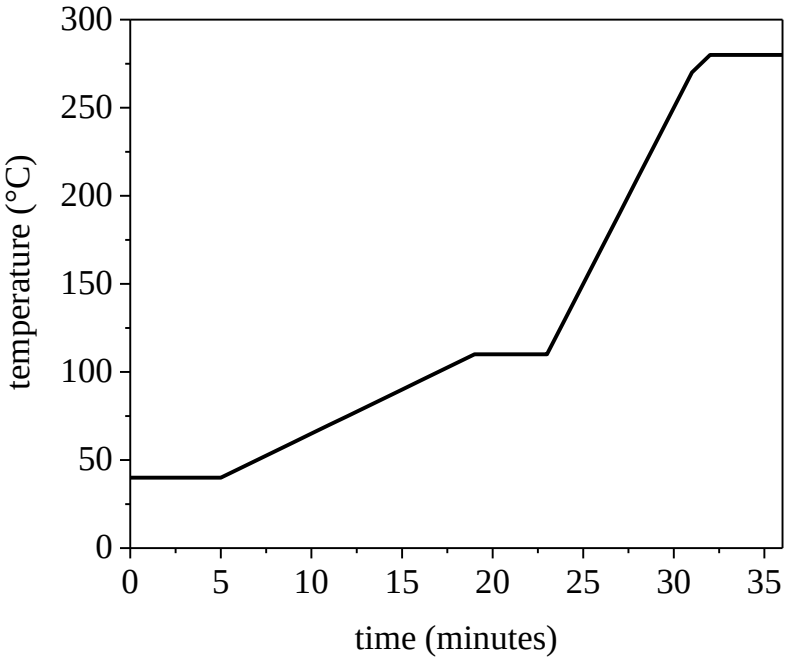

Figure 18. Temperature ramping profile used for all reference measurements and experiments.

To explore each parameter in depth a series of experiments were conducted where combustion samples of identical composition and concentration were analyzed using various GC methods. These samples consisted of multiple components that co-eluted from 11 to 14 minutes, including acetaldehyde, propene, water, and oxirane. Method variables were individually adjusted and the change in elution of species was observed (**Figure 19**).

First, upon reaching a temperature set point, the time at which the temperature was held constant had no effect on co-elution. Lowering the rate of temperature ramping increased peak separation; however, at the detriment of the total method time. The above temperature profile (**Figure 18**) was employed to maximize peak separation and maintain a realistic method runtime at 36 minutes to ensure combustion experiments could occur in a timely manner.

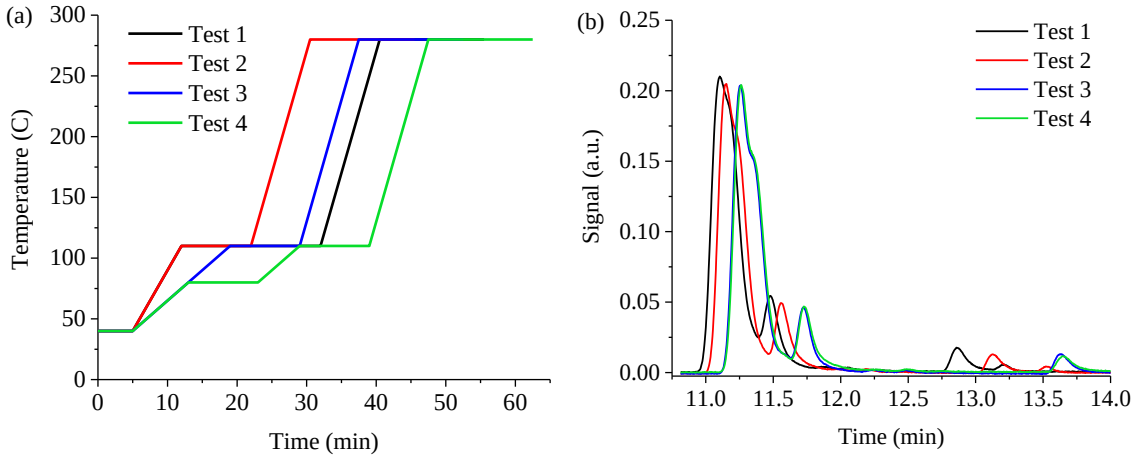

Figure 19. Temperature ramping profiles (a) adjusted to optimize peak separation (b). Tests 3 and 4 (blue and green, respectively) yielded the best peak separation but at the cost of longer run times totaling 53 and 63 minutes, respectively.

Another method that was developed was for syringe-injection of liquids into the GC. While the majority of reference measurements were made in the gas-phase from the vapor-phase of a liquid, occasionally the vapor pressure was too low to capture enough in the gas-phase. Therefore, the liquid was directly injected into the GC for reference measurement. As this was not the standard procedure, a new method was developed.

The primary concern was that with a pure liquid, saturation limits would be surpassed and the accompanying signal would be too saturated to use. To prevent saturation, the split ratio and injection volume were tested and adjusted once optimized. An injection volume of 0.2 µL and a split ratio corresponding to a dilution factor of 2.5 were used, where the dilution factor is in reference to the gas-phase method split ratio. This method will be used in future work where gas-phase reference measurements are not possible (**Appendix A**).

2.3.2 On-column reference collection

As discussed in Section 2.2.1, EI-MS and VUV absorption reference measurements were conducted on all species relevant to ongoing combustion experiments including the work herein. In EI-MS measurements, gas-phase species are ionized with 70-eV electrons and detected as a function of mass-to-charge ratio (*m/z*). Each parent molecule has a characteristic mass spectrum classified by a fragmentation pattern of ion fragment peaks of varying abundance, the relative proportions of which depend on molecular structure. Fragmentation patterns are determined most commonly by conventional mechanisms including α-cleavage, inductive effect, hydrogen rearrangement, and transannular cleavage (**Figure 20**).[81] While EI-MS is frequently utilized in combustion experiments, fragmentation patterns are rarely explored in depth. Instead isomeric structure is derived from analysis of logical neural losses from the parent ion, M^+, (i.e. $[M\text{-}H_2O]^+$, $[M\text{-}CH_3]^+$, etc.).[82,83] Exclusive reliance on logical neutral losses and fragmentation patterns introduces uncertainty, especially when parent cations are unstable and the ion peak at the corresponding *m/z* is absent. Additionally, although fragmentation mechanisms can qualitatively predict relative ratios of fragment peaks, constitutional isomers often yield ions at the same *m/z*, making it difficult to predict quantitative ion ratios compounding the uncertainty. Therefore, direct reference measurements of mass spectra are necessary.

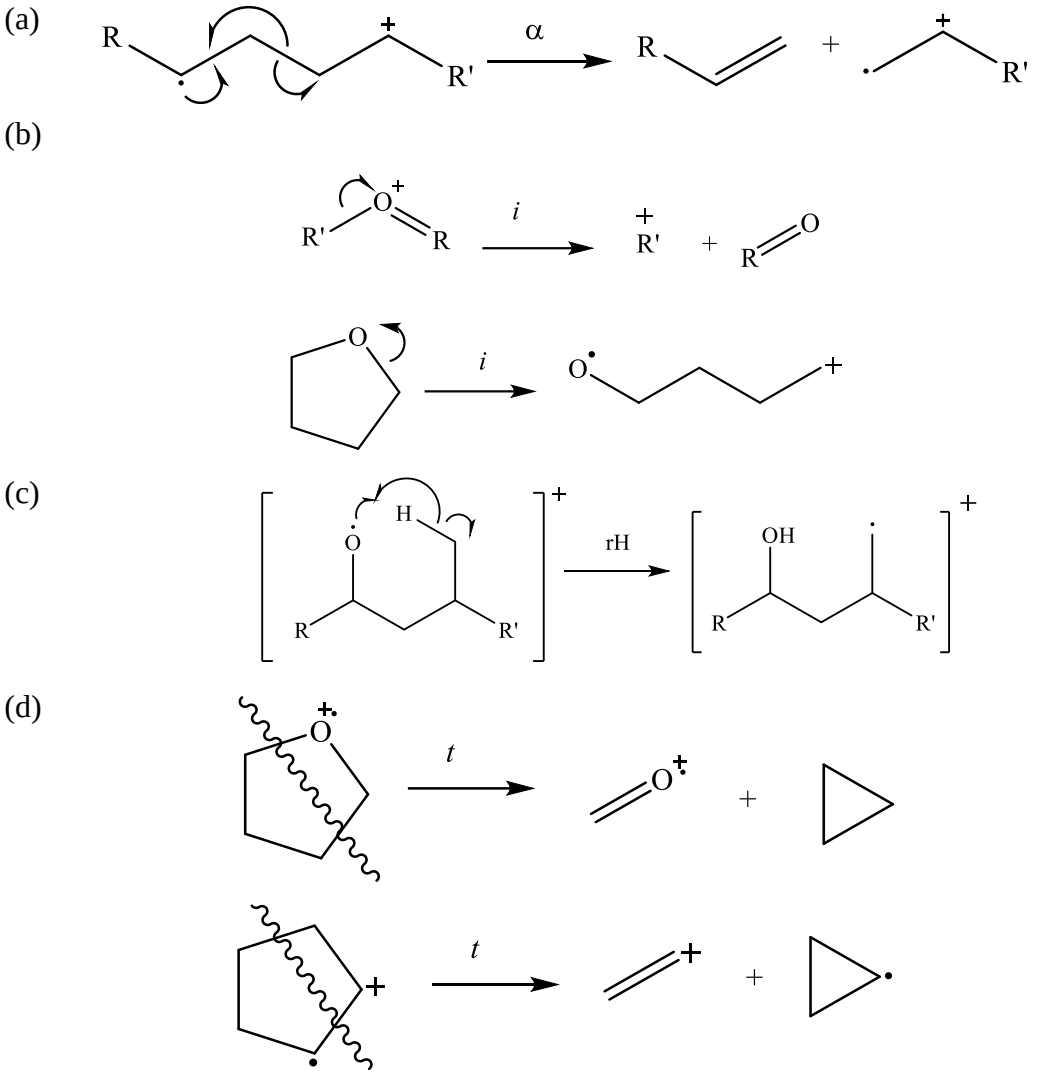

Figure 20. Fragmentation mechanisms: (a) α-cleavage, (b) inductive effect, (c) hydrogen rearrangement, and (d) transannular cleavage.

To further explore the need for reference mass spectra and to contribute new mass spectra to the community, EI-MS were measured for 29 cyclic ethers, an important class of intermediate in low-temperature combustion, where 10 mass spectra were measured for the first time in Koritzke et al.[84] Fragmentation mechanisms were discerned and common patterns among species of similar molecular structure were identified. Of note, for seven species, parent ion peaks were absent necessitating reference spectra. These species

included some of the most highly functionalized of those measured such as (2-methyloxiranyl)methanol, 3,3-dimethyloxetane, and 2-methyl-1,3-dioxolane. For species for which there were existing mass spectra data in NIST and/or literature, the measurements of the work herein were cross-referenced using peak ratios – defined as the abundance of $(m/z)_1$ divided by the abundance of $(m/z)_2$.

Select mass spectra and fragmentation mechanisms are depicted for oxirane, oxetane, oxolanes, and oxane species, including *cis*-2,3-dimethyloxirane, 3,3-dimethyloxetane, tetrahydrofuran, and tetrahydropyran, respectively. These species are not only relevant for this work, but are useful for other areas of research. For example, *cis*- and *trans*-2,3-dimethyloxirane are intermediates of the low-temperature combustion of *n*-butane and continue to undergo chain reactions, which play a larger role in the overall reaction mechanism of *n*-butane. Notably stereochemistry influences which reaction pathways are accessible due to steric effects, which causes a difference in yields of products derived from each isomer.[57] Therefore, it is imperative to have accurate references for each isomer to aid experimental efforts in investigating this combustion behavior.

The mass spectrum of *cis-2*,3-dimethyloxirane (*m/z* 72) and proposed fragmentation mechanisms are presented in **Figure 21** where there is a weak parent peak.[84] The fragment peak at *m/z* 43 is produced from transannular cleavage and that at *m/z* 27 is derived from inductive cleavage followed by hydrogen rearrangement and an α-cleavage step. The mass spectrum of *trans*-2,3-dimethyloxirane was measured as well, and the fragmentation patterns differed negligibly. The difference in peak ratios between the highest abundance peak and parent peak was 0.5% for *cis*- versus *trans*-2,3-dimethyloxirane.

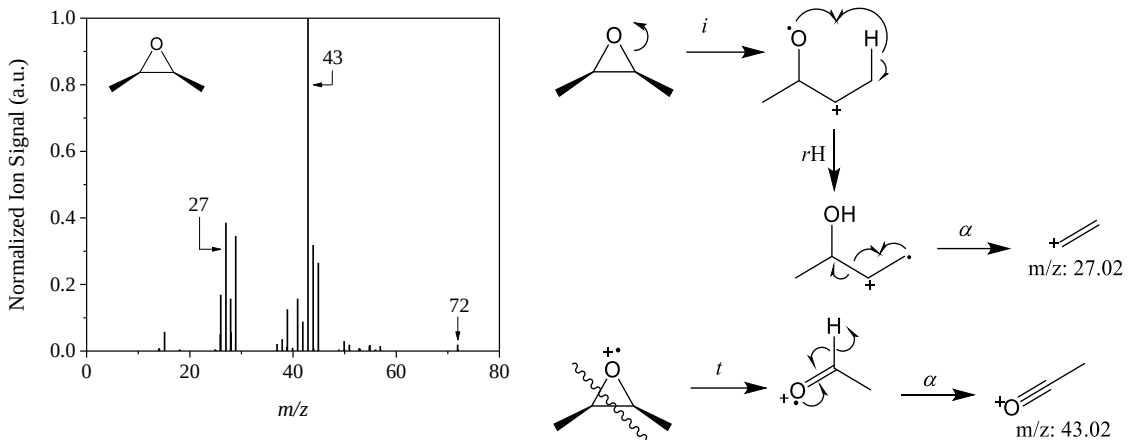

Figure 21. Mass spectrum of *cis*-2,3-dimethyloxirane (*m/z* 72) and fragmentation mechanisms for *m/z* 27 and *m/z* 43.

The mass spectrum of 3,3-dimethyloxetane (*m/z* 86) was reported for the first time and the parent peak was not detected (**Figure 22**). The most abundant fragment peak is at *m/z* 56 and is produced via conventional fragmentation mechanisms consisting of an α-cleavage and an inductive cleavage in either order. As described by Dagaut et al.[85], 3,3-dimethyloxetane is a combustion intermediate of *neo*-pentane, a component of gasoline, and a simple branched alkane for functional group studies. Especially due to the lack of a parent peak and relevance to *neo*-pentane combustion experiments, the reference of 3,3-dimethyloxetane was necessary.

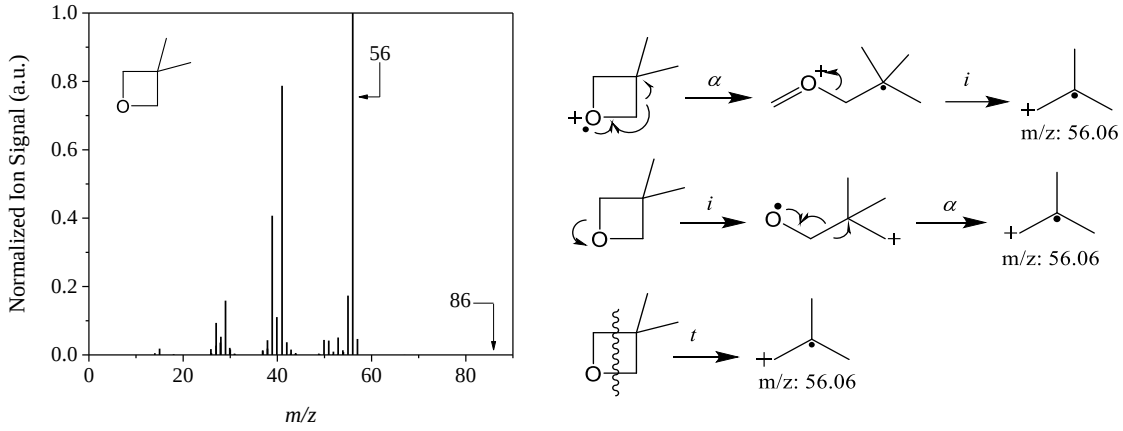

Figure 22. Mass spectrum of 3,3-dimethyloxetane (*m/z* 86) where the parent peak is absent and fragmentation mechanisms for *m/z* 56.

Tetrahydrofuran is a combustion intermediate of *n*-butane that continues to undergo chain reactions contributing to the overall reaction mechanism and ȮH budget. It is also the focus of the work herein. Therefore, an EI-MS reference was measured where the parent peak is in high abundance at *m/z* 72 (**Figure 23**). Fragmentation of tetrahydrofuran is not as facile as other species as indicated by the abundant parent peak. Fragment ions can be explained via conventional fragmentation mechanisms, namely the peak at *m/z* 42, which is formed via inductive cleavage then subsequent α-cleavage, or vice versa.

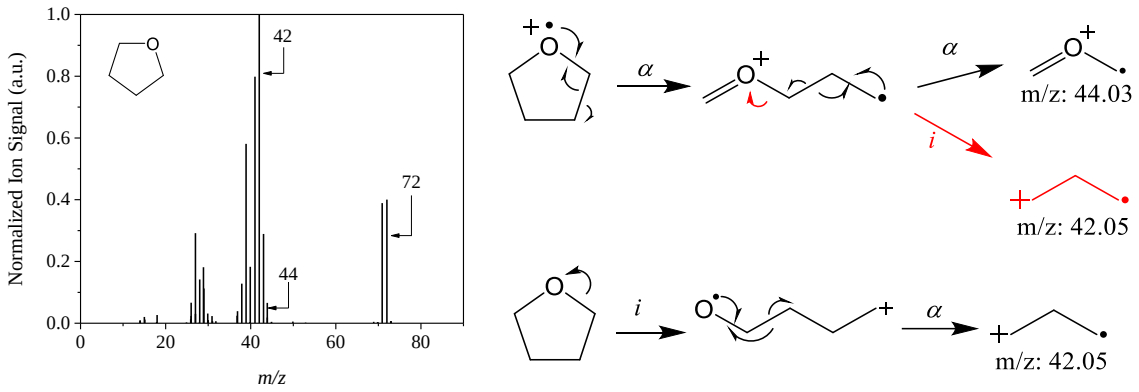

Figure 23. Mass spectrum of tetrahydrofuran (*m/z* 72) and fragmentation mechanisms for *m/z* 42 and *m/z* 44.

The mass spectrum of tetrahydropyran (*m/z* 86) and fragmentation mechanisms are presented in **Figure 24**, where conventional mechanisms explain fragment peaks at *m/z* 28, *m/z* 41, and *m/z* 56. Tetrahydropyran is an intermediate of *n*-pentane oxidation where the presence of oxygen adds to the complexity of subsequent consumption reaction mechanisms. Namely, the ether functional group restricts second O_2 reactions and enables facile ring-opening reactions in tetrahydropyran in comparison to cyclohexane.[39] While EI-MS has been used to identify tetrahydropyran in *n*-pentane experiments, no mass spectrum was reported.[64]

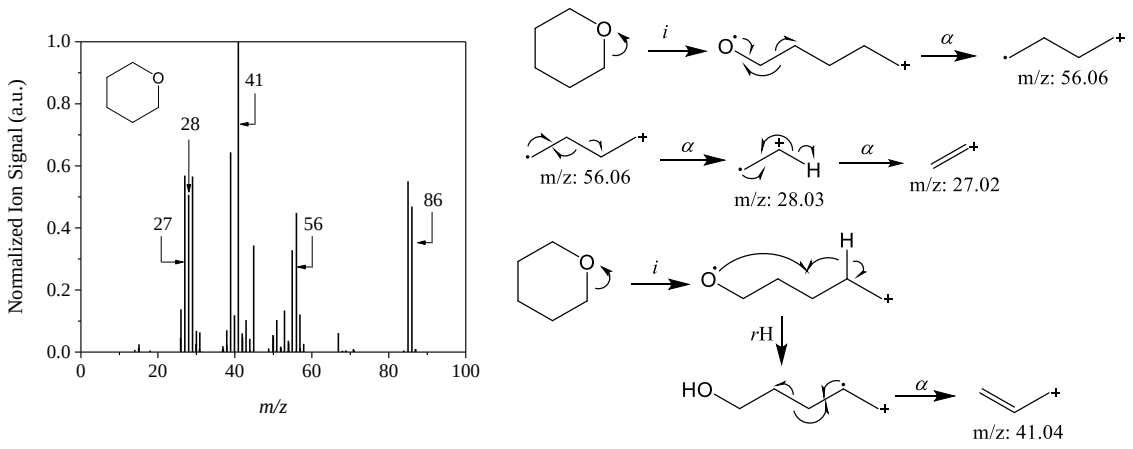

Figure 24. Mass spectrum of tetrahydropyran (*m/z* 86) and fragmentation mechanisms for *m/z* 27, *m/z* 28, *m/z* 41, *m/z* 56.

The purpose of the work of Koritzke et al.[84] was to not only provide reference EI-MS spectra, but to also explain fragmentation patterns beyond logical neutral losses to aid in deeper identification efforts using mass spectra. While conventional fragmentation mechanisms were applied to all mass spectra to discern patterns in observed peaks, for complex cyclic ethers, these mechanisms were unable to explain abundant ion peaks. As a result, fragmentation patterns may not always provide unambiguous evidence for species identification for the purpose of discerning molecular structure and constitutional isomers. Therefore, direct measurements of reference mass spectra are required.

In addition to EI-MS spectra, VUV absorption spectra have been measured for approximately 150 relevant species where binary mixture consisting of analyte and N_2 diluent was flowed through the GC column, then passed through the VUV absorption cell to measure absorbance, to mimic the method in which experimental samples would undergo analysis. Raw absorption signal was assigned to the known concentration of analyte as determined by binary mixture composition.

2.3.3 Mass spectrometry identification and quantification method development

Mass spectra references were intended to be used for both identification and quantification which could be cross-checked with that of VUV absorption. However, mass spectrometer signal was unstable, the reasons for which remain unknown despite significant time investment. Therefore, mass spectra were used exclusively for qualitative identification only. Reference spectra were measured for each species individually then added to a custom library within the software of the instrument, which allowed for automatic library matching between a given experimental sample and the closest matching reference spectrum in regard to fragment ion peaks.

In order to conduct quantification, multiple methods were explored. First, external calibration curves were established for each species, which consisted of three measurements where concentration versus chromatographic peak area was plotted. A measurement of unknown concentration with known identity and measured signal could be plotted against the calibration curve to determine concentration. A second method that was explored was to quantitatively compare peak ratios of a reference spectrum with those in spectrum measured from an experimental sample. However, complications arose from both methods as it was not possible to establish a consistent quantitative signal response.

Many attempts were made to reduce instrument and post-processing variability to achieve reproducible signal. The most consistent challenge was an unpredictable electron multiplier voltage (EMV) within the detector. Naturally, as the electron multiplier ages, the voltage must be increased to maintain the same signal level over time. However, compared to the applied voltage, a consistent signal response could not be established even within the same day. Contamination was a concern and although a bake out was performed,

maintenance was sought and completed on the mass spectrometer including source cleaning, replacement of filaments and inlets, and updated tuning. Additionally, operation was adjusted to keep either EMV or detector gain constant in order to determine if a consistent signal could be acquired, but regardless of this change, ion signal continued to vary with time. Other variables were also investigated including autotuning frequency and procedure, day-to-day change in EMV, and effect of chemical species on signal output. An attempt was made to use an internal standard of reference gas consisting of 10,000 ppm each of H_2, CO, CO_2, methane, ethane, propene, *iso*-butane, and *n*-butane, and diluted with N_2. However, procedurally, there was no feasible way to simultaneously introduce reference gas to the GC column with experimental or reference samples rendering this possibility obsolete.

Still, quantification of small species was achieved with an isolated TCD that was independent of signal fluctuations observed in the mass spectrometer. The primary means of identifying species via TCD was retention time only. Retention times were known for H_2, CO, CO_2, N_2, and methane as determined from reference gas upon set up of the instrument. However, that of oxygen was unknown. A binary mixture of oxygen as the analyte and diluted with N_2 was made at 1000 and 2000 ppm and measured as with any reference mixture. A new peak was observed on the TCD chromatogram and was assigned to oxygen. In order to quantify, reference peak areas were associated with known concentrations measured from reference gas and the separate oxygen reference. Experimental concentrations were determined by utilizing a simple ratio of concentration to signal and comparing that of the reference peak areas with measured experimental signal.

2.3.4 Absorption spectroscopy identification and quantification method development

Prior to identification and quantification, optimization of the VUV absorption instrument was necessary to maximize signal output. This was essential because given our dilute experimental conditions, the detected low-temperature combustion intermediates are low in concentration often at tens to hundreds of ppm. By increasing signal output, it was possible to ensure that all products, even those at low concentrations, were being detected at high signal-to-noise ratios.

The most effective component to improve VUV absorption signal was the makeup gas pressure. Similar to split ratio in gas chromatography, the makeup gas pressure correlates to the amount of diluent gas that is introduced independently from the sample where as makeup gas pressure increases, the concentration of diluent gas increases, in turn further diluting the sample (**Figure 25**). Ideally, the makeup gas pressure could be lowered to reduce the amount of diluent boosting the signal of analytes.

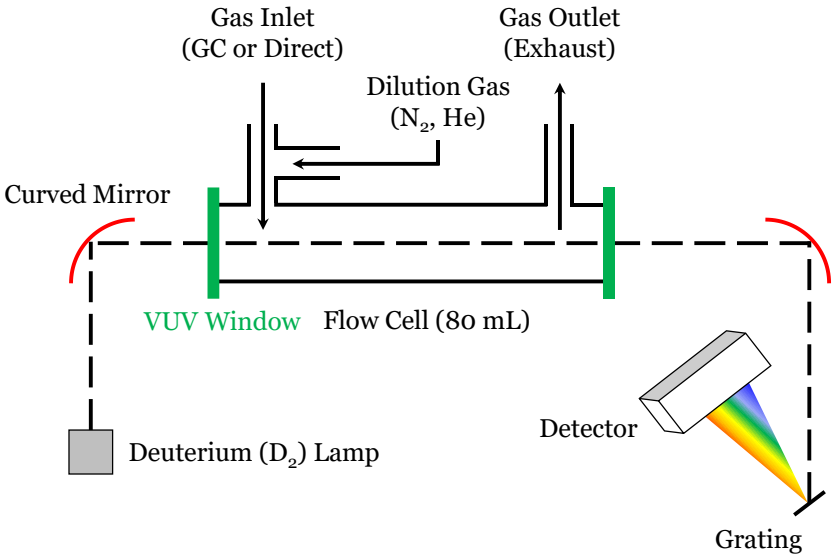

Figure 25. Schematic of VUV absorption instrument where gas-phase sample introduced via GC meets makeup gas, which acts as a diluent, and the resulting diluted mixture passes through the flow cell.

Makeup gas pressure is the gauge pressure measured within the flow cell regulated by the flow coming into the VUV instrument and that going out. The inlet pressure is supplied by a constant flow of N_2 gas running through the GC column. The outlet pressure can be regulated in a number of ways. First, the exit flow can be directed to an external vent held at slight negative pressure relative to ambient. Alternatively, outlet flow is regulated via a pressure controller, which can either hold pressure constant at a fixed set point, or can allow flow to pass through a regulated valve that is opened to a fixed percentage of full-scale range. While the inlet supply remained unchanged due to the constant flow of gas through the GC, outlet control was tested to determine which method could reach the lowest makeup gas pressure without falling subject to slight pressure fluctuations caused by limits in the pressure controller or ambient pressure.

With an increase in makeup gas pressure, analytes that were higher in concentration, such as unconsumed fuel, would reach the saturation limit at highest abundance of the detected peak. An example is shown in **Figure 26** for tetrahydrofuran, the experimental fuel that is in excess after combustion, where there is significant saturated signal at energies greater than ~ 8.5 eV. Although this was a concern, the quantification method that was developed circumnavigated this challenge and will be discussed further in this section.

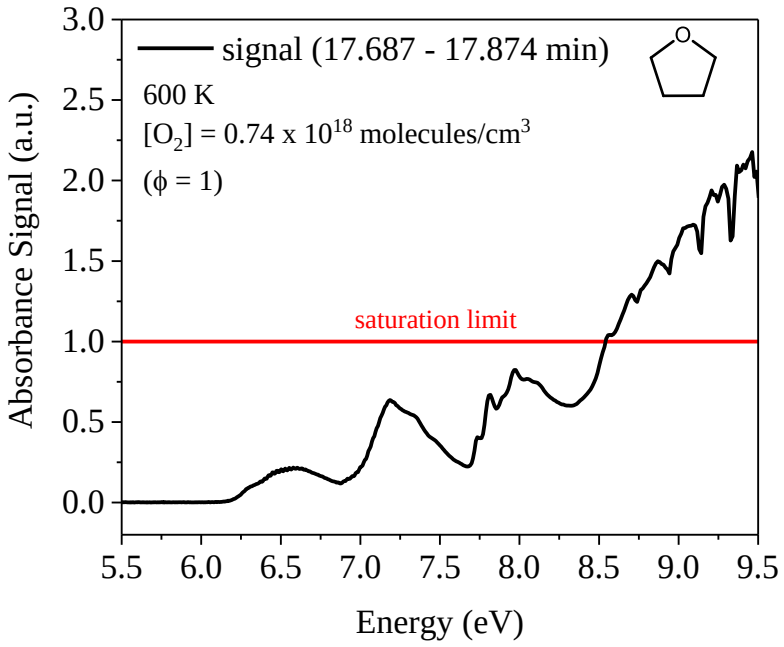

Figure 26. Absorbance signal of tetrahydrofuran, the experimental fuel in excess, where signal is saturated at energies above ~ 8.54 eV where signal surpasses the saturation limit at an absorbance of 1, which in this case equates to 7284 ppm.

Other variables that were considered to optimize signal output were detector exposure time, the number of spectra to average, the number of averages taken, scan time, and flow cell and transfer tube temperatures. It was determined that these variables were

best left unchanged from the initial settings as the set points were within limits imposed by the detector.

Detection limit experiments were conducted by making binary mixtures of 2-butanone, the experimental fuel at the time, at 1 ppm and 10 ppm. Prior to optimizing the makeup gas pressure, the detection limit was 10 ppm. However, after optimization, the signal increased significantly at lower makeup gas pressure, increasing signal-to-noise and extending the detection limit to 1 ppm (**Figure 27**).

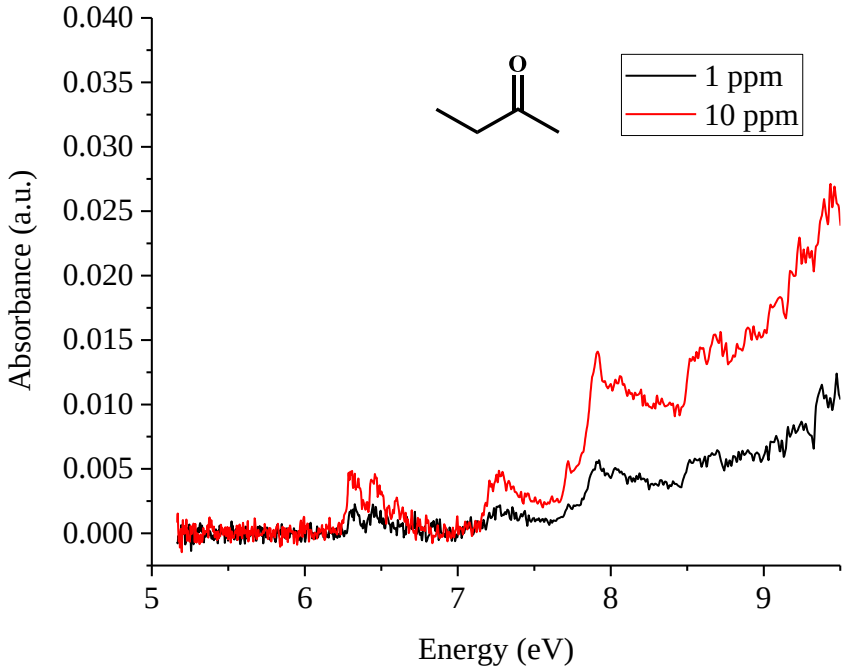

Figure 27. Absorbance spectra for 2-butanone reference made at 1 ppm and 10 ppm.

In order to identify detected species, the absorption spectrum of an unknown species was cross-referenced with our collection of reference spectra, which were measured individually as discussed in Section 2.2. Isomer-resolved identification was

possible due to distinct spectral features observed in absorption measurements resulting from unique electronic transitions including $\sigma \rightarrow \sigma^*$, $n \rightarrow \sigma^*$, $\pi \rightarrow \pi^*$, and $n \rightarrow \pi^*$.

Many methods were explored in order to quantify absorption spectra, a summary of which is presented in **Figure 28**. To summarize, two types of raw data could be extracted – a chromatogram and an absorbance spectrum, where in the former analyte peaks were integrated and analyzed and in the latter background subtracted absorbance spectra were analyzed via averaging or summing techniques. Definitions for terms used for quantification are written in **Table 1**.

Table 1. Definitions of quantification terms including background subtracted average and sum.

Term	Definition
background spectrum	representative absorbance spectrum over a given time range prior to the onset of signal that is treated in the same way as a sample peak (averaged or summed)
background-subtracted average	individual absorption spectra over a given time range are **averaged** together to produce a single representative spectrum over that time window and has an **averaged** background spectrum subtracted from it; y-axis of representative spectrum is absorbance of the averaged signal
background-subtracted sum	individual absorption spectra over a given time range are **summed** together to produce a single representative spectrum over that time window and has a **summed** background spectrum subtracted from it; y-axis of representative spectrum is qualitative and can no longer be used as a direct metric for saturation limit observation (c.f. **Figure 17**)

The quantification technique was developed over the course of one year and included optimizing the following steps: absorbance spectrum extraction and quantification procedure, both of which were optimized to reduce use-to-user variability, maximize precision and accuracy, and remain sensitive to detection constraints, such as

saturation and noise. Additionally, chromatogram peak extraction was investigated, although ultimately was not used as the method involved a cumbersome program, multi-step process, and too much user-to-user variability.

In either method, raw reference data was processed in the exact same way as sample data and they were quantified using the relationship described in **Equation 6**, where "Signal" could be an absorbance if using the absorbance spectrum or integrated peak area when using a chromatographic peak.

$$\frac{\text{Signal}_{\text{ref}}}{[\text{Conc}]_{\text{ref}}} = \frac{\text{Signal}_{\text{sample}}}{[\text{Conc}]_{\text{sample}}} \quad (6)$$

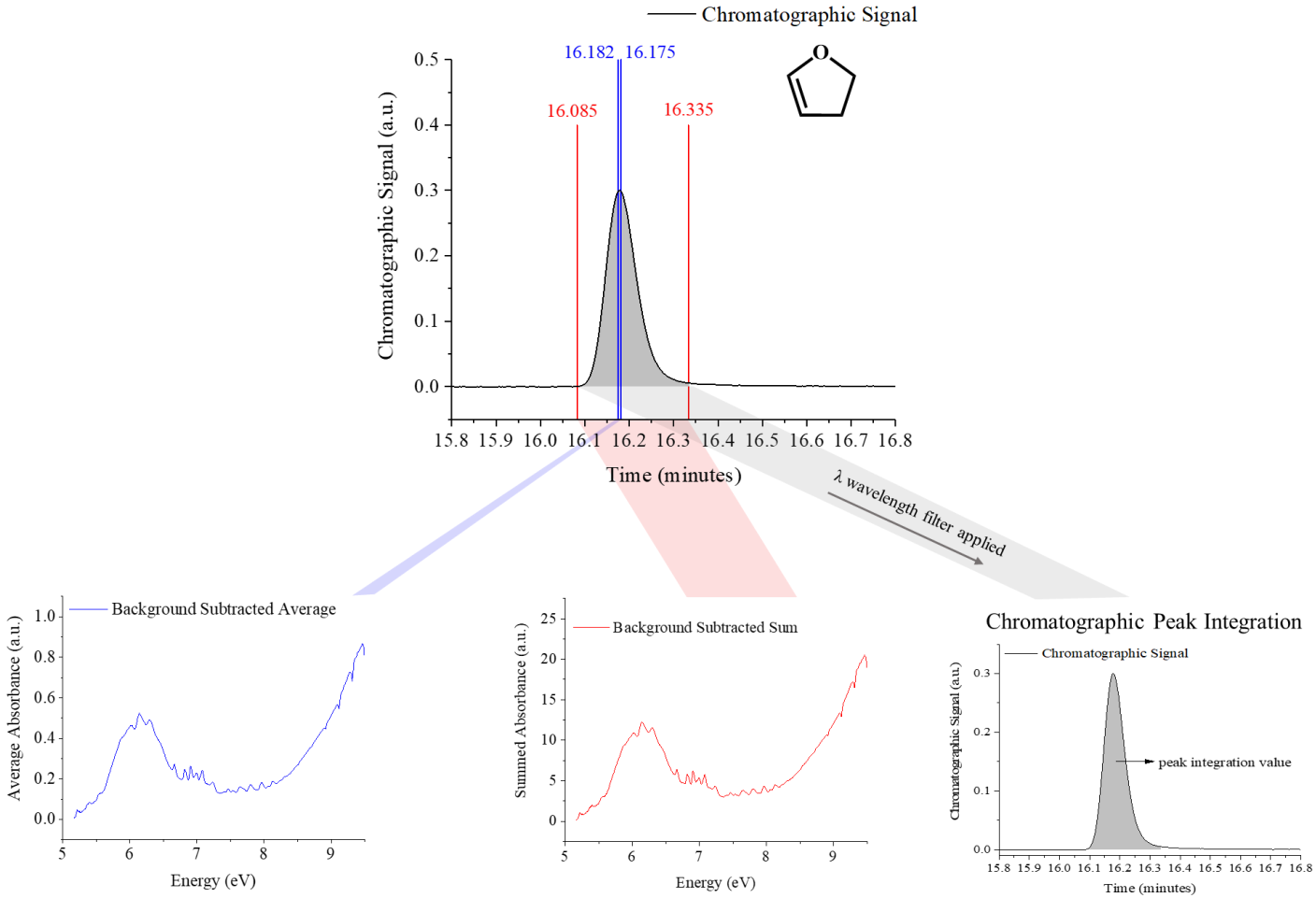

Figure 28. A summary of the ways in which VUV absorption data can be extracted including background subtracted average over a 0.01 minute Δt (blue), background subtracted sum encompassing the entire chromatographic peak (red), and chromatographic peak integration in which a wavelength filter is applied to reduce contributions from energy regions with signal-to-noise ratios that approach the detection limit.

The main procedure to extract an absorption spectrum is to place cursors on the chromatogram over a time range (Δt) encompassing the entire peak or a portion of it. Background cursors are placed before the onset of any signal. The absorption signal at each scan over the range selected is either averaged or summed and from the resulting spectrum, that of the background is subtracted (**Table 1**). While averaging and summing were both possible and used, averaging was the primary method. Both techniques will be discussed further in this section.

The influence of the time range selected was investigated so as to determine the influence on the extracted absorbance spectrum and to establish a reproducible procedure for each user. Encompassing a larger Δt decreased the average absorption signal because as more scans were included, the number to average increased and while the overall signal decreased because the tail of peaks, which had lower signal-to-noise, were being included (**Figure 29**). Based on this assessment, only the center of the peak where the highest signal was observed was included for data extraction. Additionally, cursors were placed to always encompass three scans, which corresponded to a Δt of ~ 0.01 minutes, to reduce user-to-user variability and to continue to be able to average.

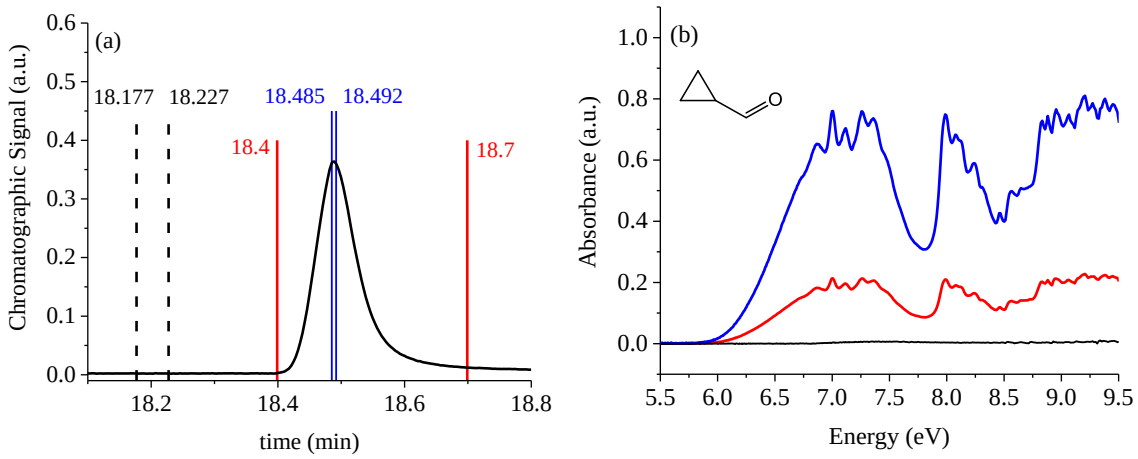

Figure 29. Chromatographic signal (a) and associated absorbance spectra (b) of cyclopropane carboxaldehyde reference where selection of background is in black prior to the onset of signal. Time range in red corresponds to the absorbance signal and red and likewise for that in blue where the narrower Δt (blue) produced an absorbance spectrum of better signal-to-noise.

When summing absorbance signal over a time range, the entire peak or a select portion of the peak can be used. When the entire peak is encompassed, the data extraction technique becomes more sensitive as the user decides where a peak starts and ends. Unfortunately, a full-width half-maximum (FWHM) method could not be adopted as it was not a feature within the instrument software and could not be easily calculated for a large data set. An attempt was made to determine if all peaks had a uniform Δt that could be applied to future data extraction. The Δt of chromatographic peaks of 12 species of varying functionalization were determined, but varied from 0.311 to 0.490 minutes (**Table 2**), where the average was 0.380 minutes, the standard deviation was 0.055, and a relative standard deviation of 14.45%. Still, given the range of peak widths and the sensitivity of an absorbance spectrum to that width (c.f. **Figure 29**), a uniform Δt was not applied.

Table 2. VUV chromatographic peak Δt for 12 species of varying functionalization where the minimum was 0.311 minutes for ethyloxirane and the maximum was 0.490 minutes for propene. The average was 0.380 minutes with a standard deviation of 0.055 and a relative standard deviation of 14.45%.

Species	**Peak Onset Time (min)**	**Peak End Time (min)**	**Δt**
ethyloxirane	16.616	16.927	0.311
1,3-butadiene	12.375	12.725	0.350
2,3-dihydrofuran	16.072	16.500	0.428
acetaldehyde	12.062	12.501	0.439
n-butane	12.43	12.801	0.371
butanone	16.325	16.704	0.379
cyclopropane carboxaldehyde	18.396	18.699	0.604
dichloromethane	14.613	14.948	0.335
iso-butane	12.062	12.430	0.368
oxirane	12.579	12.951	0.372
propene	11.572	12.062	0.490
tetahydrofuran-3-one	22.583	23.001	0.418

When using the absorbance spectrum to quantify, a concentration was calculated (**Equation 6**) at each energy step over the entire energy range measured (5.167 – 9.920 eV). Concentrations were averaged over a select energy range to minimize contributions from noise and saturation effects. The energy range was chosen based on a visual observation of the best overlap between a reference spectrum and that of a scaled sample spectrum, an example of which for 2,3-dihydrofuran is shown in **Figure 30**. The benefits of using a background subtracted absorbance spectrum to quantify were that regardless if the spectrum was averaged or summed over a consistent Δt, user-to-user variability was minimal, energy range selection was robust, and this approach provided a checks-and-balances system to observe each absorbance spectrum, which alerted the user to any spectral concerns. For example, as the detector aged, a dip in high-energy signal was observed, alerting the user that the detector needed to be replaced (**Figure 31**).

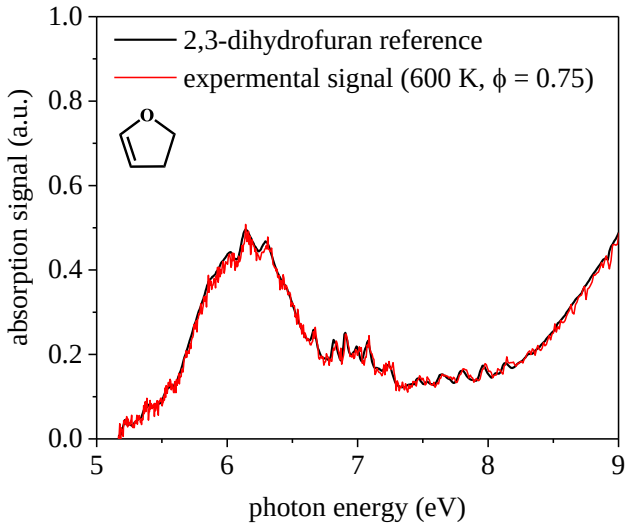

Figure 30. Absorbance signal from 2,3-dihydrofuran reference (black) overlaid with that from an experiment (red) collected at 600 K and $[O_2] = 0.99 \cdot 10^{18}$ molecules $\cdot$ cm^{-3} ($\phi = 0.75$) where experimental signal is scaled accordingly so that the energy range with the best overlap of signal can be visualized.

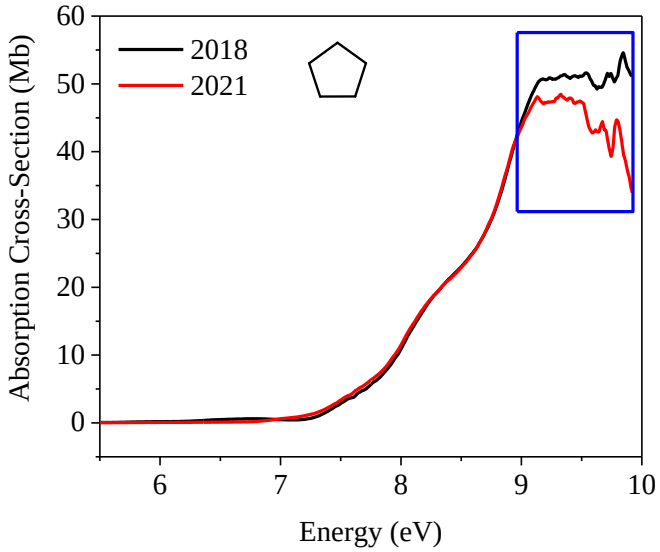

Figure 31. Absorbance cross-section spectra for cyclopentane measured in 2018 (black) and 2021 (red) where there is an observed dip in signal at high-energies > 9.1 eV. This indicates that detector maintenance is required and is only observed when using the absorbance spectrum to quantify.

The other method that was explored was chromatographic peak integration. While **Equation 6** also applied to this technique, a single concentration was calculated as there was only a single value associated with the peak integration. Because of this, wavelength filters were applied prior to integrating a peak in order to maintain the same control over noise and saturation effects. However, without observing the absorbance spectrum, it was challenging to determine what a fitting energy range was. A single peak integration value was calculated by an external program of the VUV instrument based on cursor placement around the Δt of the entire peak. While it was easier to only have a single value to work with, energy filters needed to be applied to older data retroactively, the absorbance spectrum could not be observed, and user-to-user variability was highest when determining the beginning and end of a peak for Δt cursor placement.

Ultimately, the background subtracted averaged absorbance spectrum extracted over a Δt of 0.01 minutes was used for all quantification except in certain cases of co-elution where peak distinction was not possible.

An additional method was investigated to make quantification more robust. During the initial reference measurement campaign in 2018 – 2019, references were collected at 2 psi, which is higher than current operations, as they were measured before signal optimization took place. Therefore, attempts were made to create a calibration curve to describe the relationship between makeup gas pressure and signal and/or concentration in order to scale reference measurements to the optimized makeup gas pressure of 1.1 psi. Although the relationship trend was an exponential decay, there was too much variability to assume a single calibration curve could describe the scalar for all species (**Figure 32**). Still, reproducibility was high for measurements of the same species and quantification was

accurate when reference and sample data were both measured at the same makeup gas pressure. For the jet-stirred reactor experiments herein, new reference measurements were taken at the optimized makeup gas pressure of 1.1 psi.

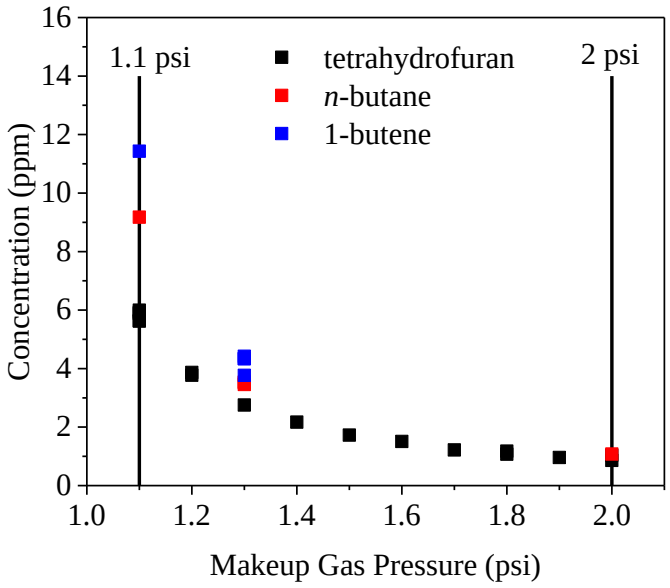

Figure 32. Calibration curve of VUV makeup gas pressure (psi) versus concentration (ppm) for tetrahydrofuran (black), *n*-butane (red), and 1-butene (blue) where the spread at 1.1 psi indicated that signal was not able to be scaled from 2 psi to 1.1 psi for all species.

Furthermore, other methods of quantification were attempted before reaching the current background-subtracted average-absorbance spectrum technique outlined previously. First, concentrations were calculated following **Equation 6** using a background-subtracted averaged-absorbance spectrum, but over four energies where the user determined the overlap between reference and sample to have minimal disagreement. This method was too arbitrary and increased user-to-user variability. An attempt was also made to calculate concentration at each energy, but rather than averaging over a select energy range, the error in concentration at each energy was calculated based on a known concentration. The concentration deemed to be most accurate was that with the lowest

error. However, this was entirely dependent on having a known concentration, which was possible for reference mixtures but not possible for experimental samples where all concentrations were unknown. This also led to coincidences where the energy with the lowest error could have been in a region with low signal-to-noise, but convenient overlap.

In the case of co-elution, two methods can be used. First, spectra could be deconvolved if one species absorbed over an energy range where the other did not (**Figure 33**). A background-subtracted averaged-absorbance spectrum over the 0.01 minute Δt at maximum peak absorbance of the multi-component peak was extracted and the concentration was calculated over the energy range where a single component absorbed. The concentration of the other component could be determined by subtracting the contribution from the first species from the total signal. Additionally, when peak resolution was unclear for convoluted peaks, library matching within the instrument software provided fitting coefficients for each matched species including when a peak is comprised of multiple components. The fitting coefficients are applied to the reference spectrum within the library, which is normalized by cross section. A non-linear fitting routine is used to fit the entire spectrum to one or more species within the library to minimize error. In order to quantify a component of unknown concentration within a multi-component match, the individual absorbance spectrum of one component is subtracted from the total signal to produce the signal of the remaining component. That remaining raw absorbance signal is then used to calculate a concentration as previously described with **Equation 6**.

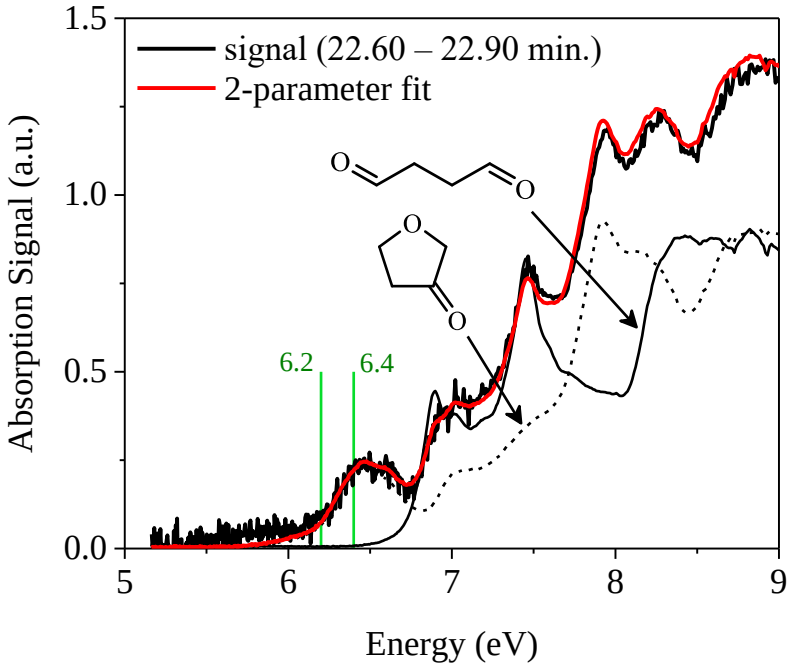

Figure 33. Convolved spectrum of tetrahydrofuran-3-one and butanedial where because tetrahydrofuran-3-one absorbs before butanedial from ~ 6 – 6.4 eV, tetrahydrofuran-3-one can be quantified within that range as the signal in that range is only attributed to tetrahydrofuran-3-one. Raw signal is from experimental conditions at 800 K and $[O_2] = 0.74 \cdot 10^{18}$ molecules $\cdot$ cm^{-3} ($\phi = 1$).

2.4 EXPERIMENTAL CONDITIONS OVERVIEW

In the present experiments, N_2 and O_2 were delivered via thermal-based mass flow controllers while gas-phase tetrahydrofuran was introduced into the JSR through a separate capillary via a temperature-programmed vapor delivery system maintained at 50 ± 1 °C. The experiments were conducted at 810 ± 4 Torr maintained via PID control, a residence time of 2.0 ± 0.1 s, and covered 500 – 1000 K in 25 – 50 K increments. The initial concentration of tetrahydrofuran remained constant at $0.14 \cdot 10^{18}$ molecules cm^{-3} (1% vol.) while O_2 varied from $0.37 – 7.40 \cdot 10^{18}$ molecules cm^{-3} (2.75 – 55%); N_2 provided the balance. Initial mole fractions are noted in **Table 3**. O_2-dependence measurements were

taken at 600 and 800 K as these were bounds of the negative temperature coefficient region at which the majority of species exhibited local maxima in concentrations.

Table 3. Initial mole fractions of all experiments.

ϕ	N_2	O_2	THF
0.10	0.440	0.550	0.01
0.25	0.770	0.220	0.01
0.50	0.880	0.110	0.01
0.75	0.917	0.073	0.01
1.00	0.935	0.055	0.01
1.25	0.946	0.044	0.01
1.50	0.953	0.037	0.01
1.75	0.959	0.031	0.01
2.00	0.963	0.028	0.01

CHAPTER 3

COMPUTATIONAL APPROACH

3.1 CHEMKIN PERFECTLY STIRRED REACTOR MODULE

The Perfectly Stirred Reactor (PSR) module of ChemKin was used to model the jet-stirred reactor experiments in this work. The purpose was to compare predictions of the existing chemical kinetics mechanisms of tetrahydrofuran by Fenard et al.[34] and Wu et al.[62] with experimental results from this work to target model deficiencies and provide directions for improvement and to examine the question as to the efficacy of the mechanisms to predict the effect of varying O_2 concentration on the competition between unimolecular decomposition of ȮOOH versus bimolecular reaction with O_2.

There are a number of outputs that were used to aid this effort. First, species concentrations were modeled with respect to temperature from 500 – 1200 K in 1 K increments where [O_2] remained constant at 5.5%. (ϕ = 1). Species profiles were also predicted as a function of O_2 where [O_2] = $0.37 – 7.40 \cdot 10^{18}$ molecules cm^{-3} (2.75 – 55%) at 600 K and 800 K, to match experimental conditions. Predictions are overlaid with experimental results in Section 4.

In addition to speciation predictions, rate-of-production analyses were used. This type of output determines the user-specified number of top reactions involved in the formation and/or consumption of a target species at a specific set of input conditions. Rate-of-production analyses are useful because insight may be gained as to which reactions the model assigns as most important, which may or may not agree with experimental

conclusions. For example, in determining the fate of dihydrofuranyl radicals, a rate-of-production analysis was performed where the top consumption reaction was attributed to the formation of furan (**Figure 57**). While this result agrees with the experimental data at 600 K, it is not the case at 800 K, indicating that other reactions may become more important. More discussion of dihydrofuranyl radicals and furan can be found in Section 4. Additionally, rate-of-production analyses are helpful in comparing multiple chemical kinetics mechanisms with each other because it may be possible to identify the cause of prediction differences. Rate-of-production analyses were used in specific cases as discussed in Section 4 to investigate specific mechanistic questions based on observed experimental results and model predictions.

Sensitivity analysis, which is a tool used to determine how sensitive certain reactions in the mechanism are to producing a species of interest using perturbation methods to the pre-exponential factor, A, for all elementary reactions, was also conducted. It is useful as it narrows the number of reactions that may require attention for improvement. Additionally, some insight was gained using Reaction Pathway Analyzer (RPA) within ChemKin, where the flux of reaction pathways from species A to species B were predicted with all intermediate species outlined. Specifically, RPA was used to determine expected reaction pathways, such as to determine how oxirane was predicted to form according to the Fenard et al.[34] mechanism (**Figure 34**).

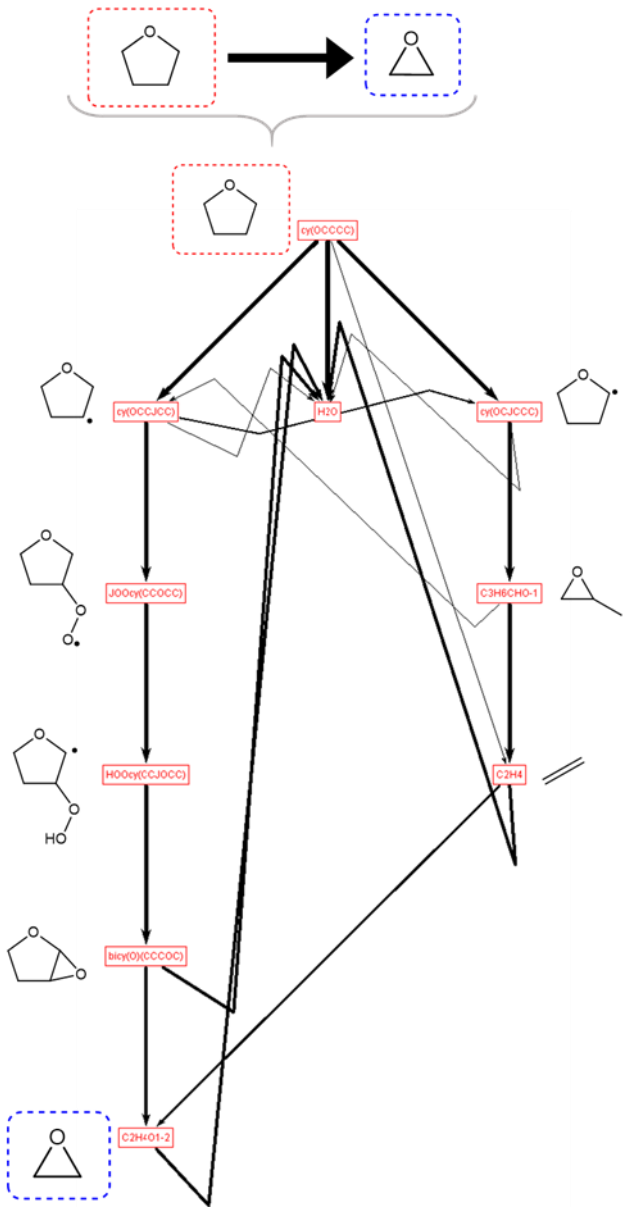

Figure 34. Output of reaction pathway analyzer in ChemKin used to determine a predicted formation pathway for oxirane from tetrahydrofuran at 600 K and O_2 = 5.5% (ϕ = 1) where each arrow represents reactions responsible for the formation of the intermediate or product shown and where the thickness of the arrows represent the percent flux of that step.

3.2 LOW-TEMPERATURE CHEMICAL KINETICS MECHANISMS OF TETRAHYDROFURAN

Two chemical kinetics mechanisms were used to predict species concentrations in order to compare to experimental results. Fenard et al.[34] created the first low-temperature sub-mechanism for tetrahydrofuran, which was added to the high-temperature combustion mechanism by Tran et al.[55] Notably, for $\dot{R} + O_2$ reactions, Fenard et al.[34] employed rate parameters optimized by Cai et al.[87] for alkanes. The rate for reaction of β-$\dot{R} + O_2$ was reduced by a factor of three to account for the weakened bond at β sites in agreement with Tripathi et al.[88] for oxidation of 2-methyltetrahydrofuran. Rate rules were adopted for formation 2,3-dihydrofuran and 2,5-dihydrofuran from similar reactions of methylcyclohexanyl. Reaction rates for ȮOOH-mediated products, butanedial and allyl formate, were estimated by Fenard et al.[34]

Wu et al.[62] updated sub-mechanisms for furan and 2,3-dihydrofuran, adding 40 new pathways and updating rate parameters in order to better predict their ignition delay time measurements by an RCM. A summary of the types of reactions that were added are shown in **Figure 35**. For furan, H-abstraction reactions by CH_3O_2, CH_2, and HCO and ring-opening reactions, including ȮH addition to form the radical HC(=O)CH=CHĊHOH, were added where rate parameters were adopted from Tran et al.[89] For 2,3-dihydrofuran additional H-abstraction reactions were included such as reaction by HOȮ, ȮH, HĊO, $ĊH_2OH$, $CH_3Ȯ$, and $Ċ_2H_5$ where rate parameters were taken in analogy with tetrahydrofuran by Fenard et al.[34] While ring-opening reactions for 2,3-dihydrofuran were included, because of a lack of thermal and kinetic data, Wu et al.[62] adopted lumping procedures for these pathways. For example, 2,3-dihydrofuranyl + O_2 may form acrolein

and formaldehyde radicals via a multi-step process, but this was lumped into one step (**Figure 36**). Adjustments to rate constants were made to better predict ignition delay time measurements. Additionally, no sub-mechanism was included for 2,5-dihydrofuran.

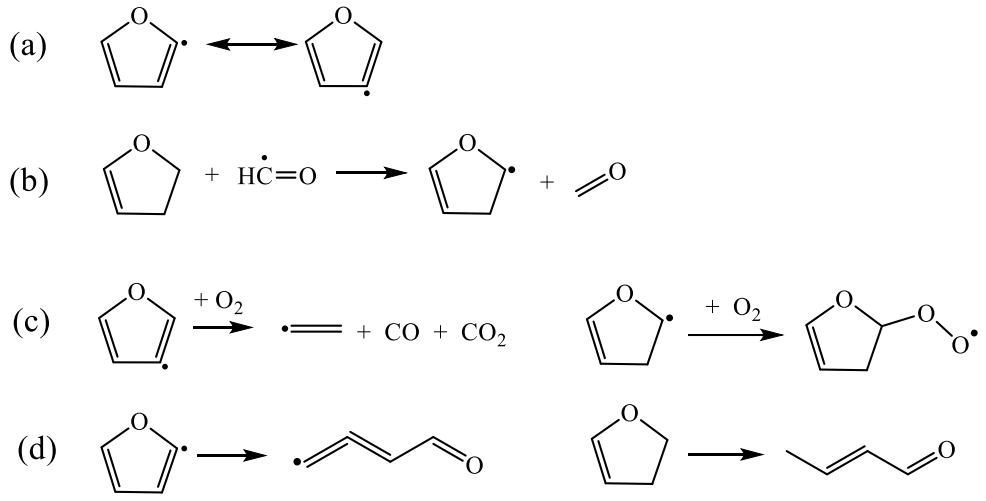

Figure 35. Examples of types of reactions included in furan and 2,3-dihydrofuran sub-mechanisms by Wu et al.[62] including rearrangement (a), H-abstraction (b), O_2-addition (c), and ring-opening (d).

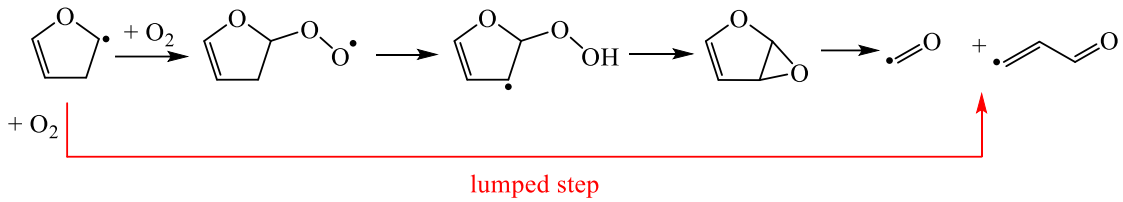

Figure 36. 2,3-dihydrofuranyl + O_2 to form acrolein and formaldehyde radicals and the lumped step adopted by Wu et al.[62] in their updated sub-mechanism. The lumped approach neglects the elementary steps and instead describes the formation of acrolein and formaldehyde radicals as a direct, one-step pathway.

CHAPTER 4

OXYGEN DEPENDENCE OF TETRAHYDROFURAN COMBUSTION AT LOW-TEMPERATURE

4.1 EXPERIMENTAL RESULTS

The combustion of tetrahydrofuran was studied with respect to oxygen-dependence ($[O_2] = 0.37 – 7.40 \cdot 10^{18}$ molecules cm^{-3} (2.75 – 55%)), temperature-dependence (T = 500 – 1000 K), and at a pressure of 1.1 atm where nineteen species were detected and quantified, several of which for the first time including tetrahydrofuran-3-one, butanedial, methyloxirane, and allyl formate where the latter three were detected by JSR for the first time. Vanhove et al.[46] detected butanedial, methyloxirane, and allyl formate in rapid compression machine experiments, but species profiles were not reported. The most abundant oxygenated species were acetaldehyde, oxirane, acrolein, propanal, furan, 2,3-dihydrofuran, and tetrahydrofuran-3-one.

A summary of detected species and reaction pathways is shown in **Figure 37**. Upon H-abstraction tetrahydrofuran can form two initial radicals, α- and β-tetrahydrofuranyl, which can undergo a network of reactions. First O_2-addition leads to tetrahydrofuranylperoxy (ROȮ), which can isomerize to form hydroperoxyalkyl radical (ȮOOH). Competition ensues between unimolecular reactions forming conjugate alkenes, 2,3-dihydrofuran and 2,5-dihydrofuran, and β-scission products including butanedial and allyl formate. Bimolecular reaction with O_2, i.e. ȮOOH + O_2 = ȮOQOOH, which leads to ketohydroperoxide formation (HOOQ'=O) and chain-branching. Two other mechanisms

unrelated to ȮOOH also lead to conjugate alkene + HOȮ and are shown in **Figure 38**: direct/concerted (from ROȮ) and formally direct (from Ṙ + O_2).

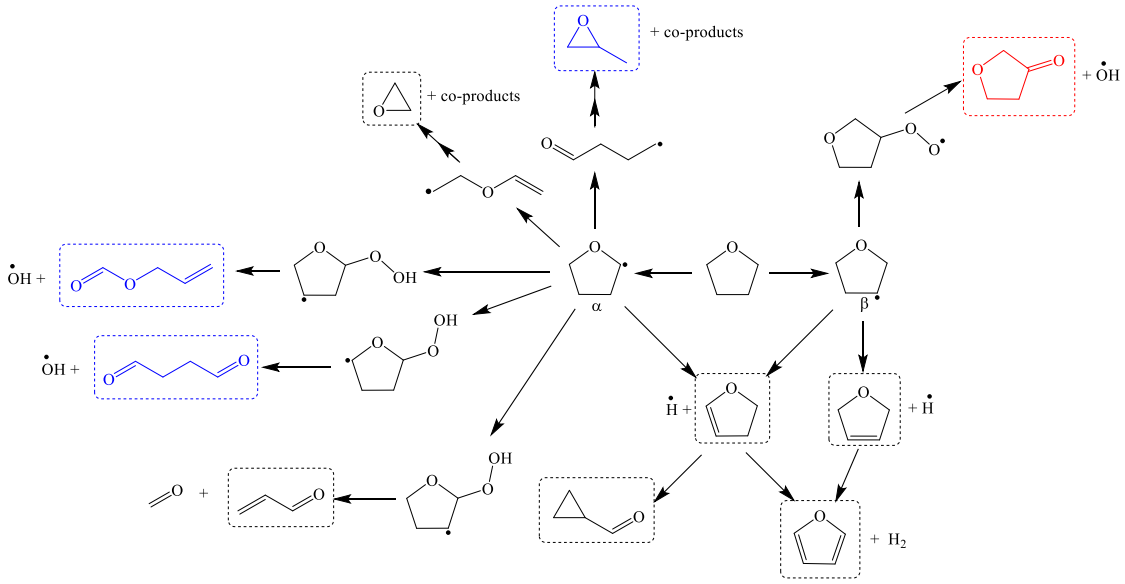

Figure 37. Pathways of tetrahydrofuran where boxed species were identified, isomer resolved, and quantified. Species detected for the first time in this work are in red and those detected for the first time by JSR are in blue. Additional species that were quantified include acetaledehyde, 1-butene, propanal, carbon monoxide, carbon dioxide, oxygen, and methane.

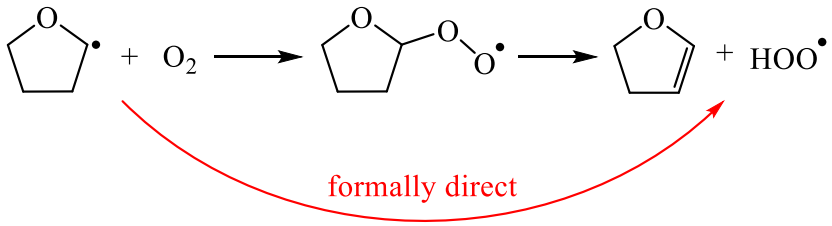

Figure 38. Formation of 2,3-dihydrofuran, a conjugate alkene of tetrahydrofuran, via two pathways: direct from ROȮ (black) and formally direct from α-tetrahydrofuranyl + O_2.

Because reaction pathways and mechanistic differences due to the presence of an ether functional group were the focus of this work, the results highlight oxygen-dependence as the concentration of O_2 provides a direct probe into which pathways are accessible and dominant within the low-temperature combustion scheme.

4.1.1 Dihydrofurans

Two dihydrofuran isomers form in tetrahydrofuran combustion – 2,3-dihydrofuran and 2,5-dihydrofuran (**Figure 39**). Temperature dependence of the species profiles (**Figure 40**) indicates negative temperature coefficient (NTC) behavior of tetrahydrofuran from ~625 K to 700 K, which is a similar range covered in the measurements by Vanhove et al.[46] and model predictions from the Fenard et al.[34] and Wu et al.[62] mechanisms. Both mechanisms reproduce the temperature dependence of the two conjugate alkene isomers and the revisions by Wu et al.[62] bring the predictions closer to the experiments quantitatively particularly above 700 K. Consistent with prior experiments[46,70], 2,3-dihydrofuran is favored, due to combined effects of lower C-H bond energy on the α site and a lower barrier height for direct HOȮ-elimination.[90]

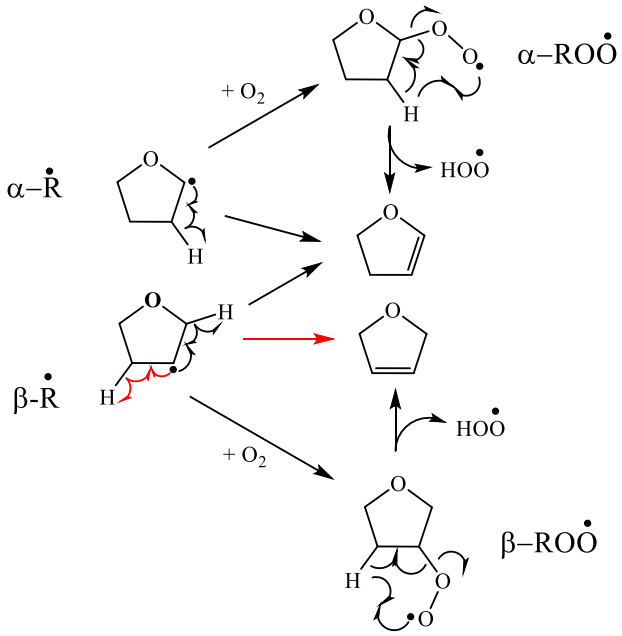

Figure 39. Formation of 2,3-dihydrofuran and 2,5-dihydrofuran from tetrahydrofuranyl radicals, α-Ṙ and β-Ṙ, and from peroxyradicals, α-ROȮ and β-ROȮ, where H-abstraction by peroxy group can occur at the H positions shown or from the β' position from α-ROȮ, yielding 2,5-dihydrofuran, and from the α from β-ROȮ, forming 2,3-dihydrofuran, the latter two reactions of which are not shown.

The maximum mole fractions of both isomers in **Figure 40**, occurring as a result of shifts in equilibria and chain-branching mechanisms as described in Section 1.1.3, correspond to the boundaries of the NTC region at ~600 K and 800 K. Both temperatures were utilized to examine O_2-dependence of products from reactions of tetrahydrofuranyl radicals and from ȮOOH reactions, such as ring-opening. O_2-variation affects the latter by perturbing the flux of ȮOOH via unimolecular reaction versus bimolecular reaction with O_2 (c.f. **Figure 5a**).

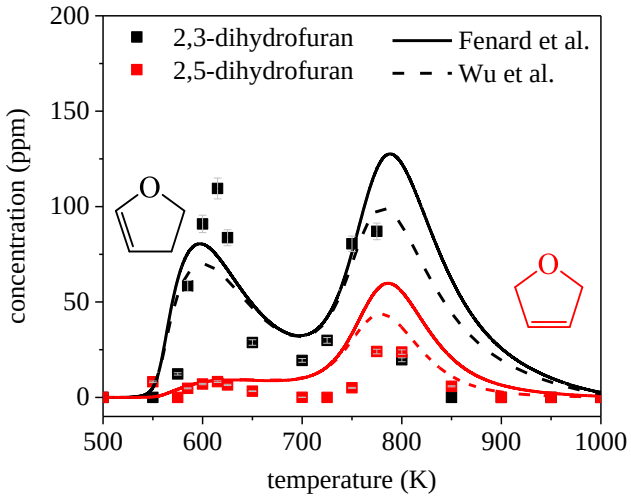

Figure 40. Temperature dependence of dihydrofuran isomers measured under stoichiometric conditions $[O_2] = 0.74 \cdot 10^{18}$ molecules $\cdot$ cm^{-3} ($\phi = 1$). Model predictions were produced using the Fenard et al.[34] mechanism (solid lines) and Wu et al.[62] mechanism (dashed lines). The NTC region is observed from ~625 K to 700 K.

β-tetrahydrofuranyl produces both 2,5-dihydrofuran and 2,3-dihydrofuran, whereas α-tetrahydrofuranyl forms only the latter. In addition to molecular structure arguments[90], 2,3-dihydrofuran is observed in higher concentrations at all O_2 conditions and at both 600 K and 800 K because of the additional formation pathway. **Figure 41** shows the concentrations of both dihydrofuran isomers measured as a function of $[O_2]$ with model predictions for comparison. Fenard et al.[34] included tetrahydrofuranyl-related reactions and dihydrofuran mechanisms. Subsequently, Wu et al.[62] added new sub-mechanisms of furan and 2,3-dihydrofuran that accounted for ring-opening, isomerization, and other consumption reactions.

At 600 K, the measurements of 2,3-dihydrofuran shown in **Figure 41a** exhibit higher O_2-dependence compared to model predictions evidenced by a difference in d[2,3-dihydrofuran]/d[O_2] where that for the experiments is 148, for Fenard et al.[34] is 105, and

for Wu et al.[62] is 84 at $[O_2] < 1 \cdot 10^{18}$ molecules cm^{-3} (**Table 4**). Above ~$1 \cdot 10^{18}$ molecules cm^{-3}, both mechanisms predict an insensitivity to higher oxygen concentration as d[2,3-dihydrofuran]/d[O_2] for both mechanisms remains positive. In contrast, the experiments reach a maximum at ~$1 \cdot 10^{18}$ molecules cm^{-3} and then decrease with increasing O_2 where d[2,3-dihydrofuran]/d[O_2] becomes negative. Similarly, at 800 K (**Figure 41b**), the experimental profile for 2,3-dihydrofuran exhibits strong positive O_2-dependence at lower concentrations of O_2 where at $[O_2] < 1 \cdot 10^{18}$ molecules cm^{-3}, d[2,3-dihydrofuran]/d[O_2] is ~95 for the experimental measurements, but only 17 for Fenard et al.[34] and 9 for Wu et al.[62] However, in contrast with the profile at 600 K, 2,3-dihydrofuran concentrations plateau with increasing O_2 rather than decrease as d[2,3-dihydrofuran]/d[O_2] remains positive at all concentrations of O_2 (**Table 4**).

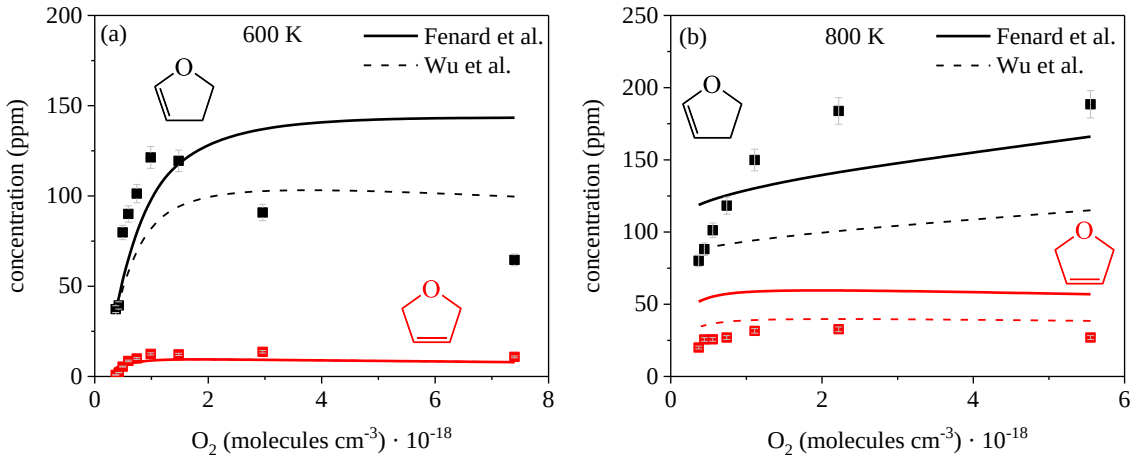

Figure 41. O_2 dependence of 2,3-dihydrofuran and 2,5-dihydrofuran concentrations measured at (a) 600 K and (b) 800 K and comparison to model predictions using Fenard et al.[34] and Wu et al.[62]. In (a), for 2,5-dihydrofuran, predictions using Wu et al.[62] are identical to Fenard et al.[34], and therefore indistinguishable.

Table 4. Average changes in concentration of 2,3-dihydrofuran with respect to $[O_2]$ at 600 K and 800 K, where distinction is made at $[O_2] = 1 \cdot 10^{18}$ molecules cm^{-3} as this is an inflection point for experimental data at 600 K.

		d[2,3-dihydrofuran]/d[O_2]		
	O_2 (10^{18} molecules cm^{-3})	this work	Fenard et al.[34]	Wu et al.[62]
600 K	< 1	148.4	105.4	84.8
	> 1	-10.0	12.4	6.0
800 K	< 1	94.8	17.4	8.8
	> 1	8.7	8.0	4.7

Wu et al.[62] revised the Fenard et al.[34] mechanism by adding H-abstraction reactions from 2,3-dihydrofuran, noting that rate parameters are lacking (c.f. **Figure 35**). In the absence of thermal and kinetic data, lumped reactions were utilized for dihydrofuranyl radicals, which is a potential a source of disagreement between the experimental and model profiles (c.f. **Figure 36**). Species profiles of 2,5-dihydrofuran show consistency between the experiment and models at 600 K. The Fenard et al.[34] and Wu et al.[62] mechanisms predict the same concentrations and overlap in **Figure 41a**. At 800 K, some disparities are evident. Both mechanisms reproduce the qualitative trend of the experiments yet the Fenard et al.[34] model overpredicts 2,5-dihydrofuran up to a factor of two. The model results from Wu et al.[62] improve upon the agreement with experimental measurements by a factor of 1.4. Despite an improvement in agreement, the sub-mechanisms produced in Wu et al.[62] focused on furan and 2,3-dihydrofuran, and did not address any additional reactions of 2,5-dihydrofuran. Developing a similar sub-mechanism for 2,5-dihydrofuran that includes additional H-abstraction, O_2-addition, rearrangement, and ring-opening reactions, may improve not only model predictions of 2,5-dihydrofuran, but also of 2,3-dihydrofuran and furan as 2,3-dihydrofuran, 2,5-dihydrofuran, and furan pathways are interconnected (c.f.

Figure 42). For example, a ring-opening consumption pathway of 2,5-dihydrofuran that is not included in current mechanisms may deplete 2,5-dihydrofuran detracting from furan formation.

4.1.2 Dihydrofuran-derived species

Two species are derived from consumption pathways of dihydrofuran isomers – furan and cyclopropane carboxaldehyde. Species profiles were measured for both as a function of temperature and oxygen concentration (**Figure 43**).

Both dihydrofuran isomers can undergo H-abstraction followed by reaction with O_2 to form furan (**Figure 42**). The temperature dependence measurement reflects NTC behavior of tetrahydrofuran from ~600 K – 650 K with local maxima mole fractions at 600 K and 800 K (**Figure 43a**). Species profile measurements with respect to O_2 show positive dependence on the concentration of O_2 at both temperatures, the scale of which is not captured by model predictions (**Figure 43c**). At 600 K, the furan concentration measurements plateau towards the highest [O_2] measured. At 800 K, furan yield increases and follows a similar trend. Both computational mechanisms predict weak O_2 dependence for both temperatures.

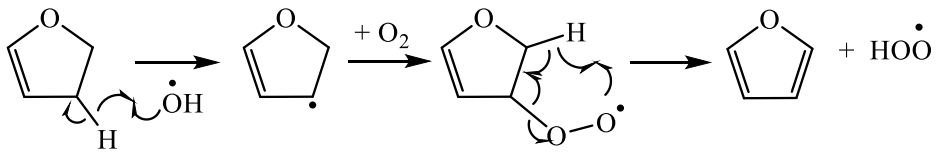

Figure 42. Formation of furan from 2,3-dihydrofuran via an H-abstraction to form 2,3-dihdyrofuranyl, which undergoes reaction with O_2 followed by HO_2 elimination form furan.

Because of a weaker temperature dependence for the production of furan, below $[O_2]$ ~$1 \cdot 10^{18}$ molecules cm^{-3} the Wu et al.[62] mechanism improves upon predictions of experimental concentrations. Increased furan yield with increasing $[O_2]$ is potentially related to the decreasing yield of 2,3-dihydrofuran (c.f. **Figure 41**), which may indicate that rates for $\dot{R} + O_2 \rightarrow$ alkene + $HO\dot{O}$, as well as via $\dot{Q}OOH$ pathways require revision to account for $[O_2]$ dependence.

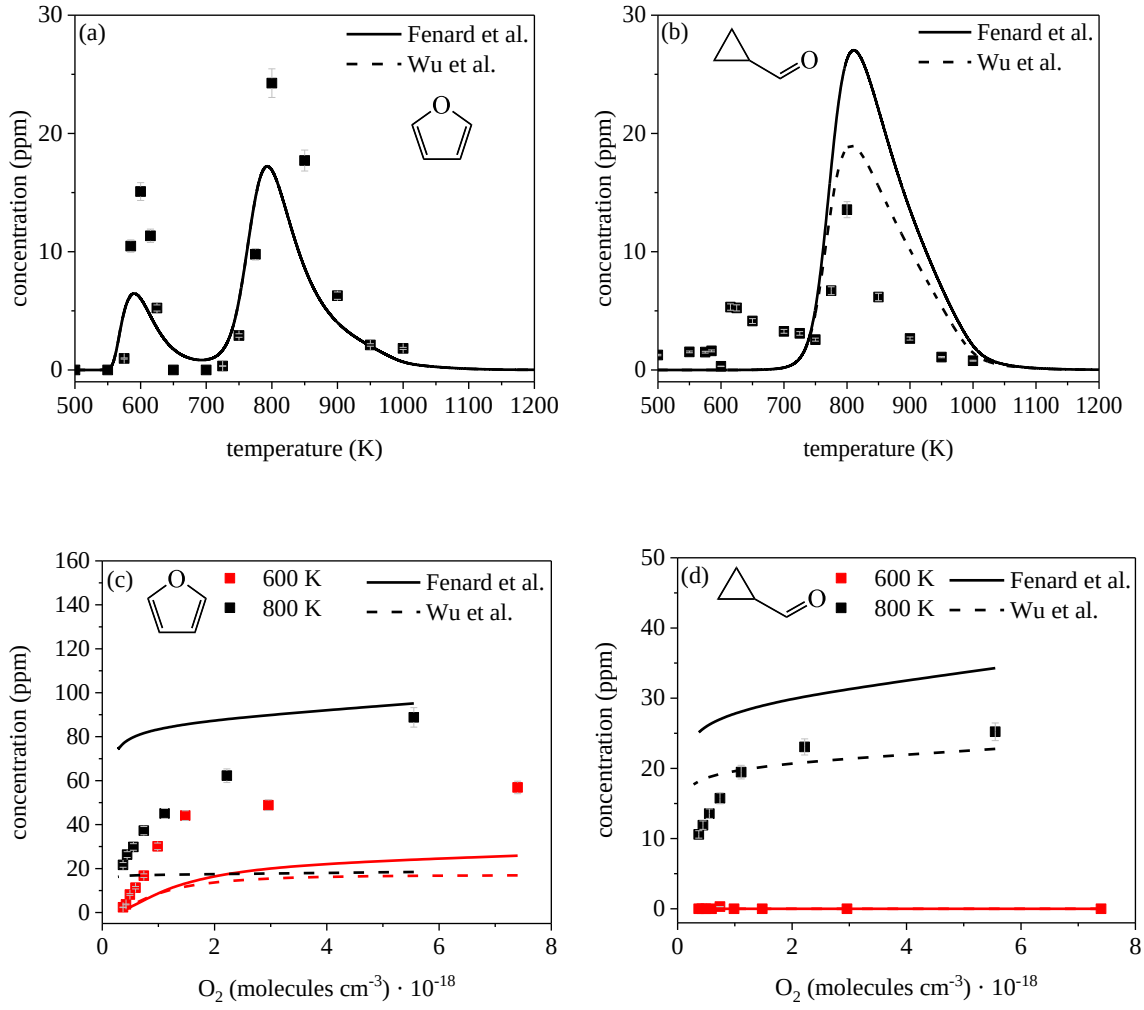

Figure 43. Temperature dependence of furan (a) and cyclopropane carboxaldehyde (b) measured under stoichiometric conditions; $[O_2] = 0.74 \cdot 10^{18}$ molecules $\cdot$ cm^{-3} ($\phi = 1$). While NTC behavior is minimal for cyclopropane carboxaldehyde, that for furan is observed from ~600 – 650 K. Oxygen-dependence of furan (c) and cyclopropane carboxaldehyde (d) are observed to be positive for both species.

Cyclopropane carboxaldehyde is derived from a rearrangement reaction of 2,3-dihydrofuran (**Figure 44**).[91] At temperatures less than 800 K, cyclopropane carboxaldehyde was detected at less than 10 ppm, sometimes not at all, which is consistent with the predicted concentrations of < 1 ppb by Fenard et al.[34] and Wu et al.[62] (**Figure 43b**). **Figure 43d** shows the dependence on O_2 at 800 K where tens of ppm were quantified,

which is in agreement with Vanhove et al.[46] Both mechanisms capture the qualitative dependence on O_2 above ~1 · 10^{18} molecules cm^{-3} (ϕ = 0.5), where the Wu et al.[62] predictions are also quantitatively consistent. The differences between the experiment and model predictions range from a factor of 0.9 to 0.2 at $[O_2] = 0.74 – 5.55 \cdot 10^{-18}$ molecules $\cdot cm^{-3}$ (ϕ= 0.75 – 0.1) and deviate up to a factor of 1.7 at $[O_2] = 0.37 \cdot 10^{-18}$ molecules cm^{-3} (ϕ = 1.5). The over prediction by both mechanisms, in comparison to the experiments, particularly towards the lower oxygen concentrations coincides with similar disparities in the predictions of 2,3-dihydrofuran (cf. **Figure 41b**), which is the sole source of cyclopropane carboxaldehyde. The disparities may result from incomplete description of 2,3-dihydrofuran reactions, such as lumped steps of O_2-addition to 2,3-dihydrofuranyl radicals (c.f. **Figure 36**).

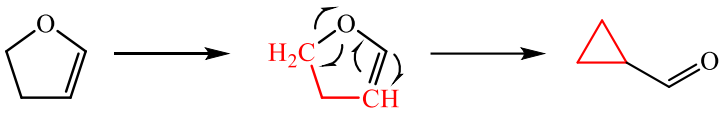

Figure 44. Rearrangement of 2,3-dihydrofuran to form cyclopropane carboxaldehyde.

4.1.3 Isomer-specific tetrahydrofuranyl products

Two species, oxirane and methyloxirane, were detected that are ascribed to ring-opening of α-tetrahydrofuranyl, which directly forms either ethene or 1-propyl depending on the β-scission reaction (**Figure 45**). Both species stem from epoxidation reactions where oxirane forms via epoxidation of ethene and methyl oxirane via epoxidation of propene (derived from oxidation of 1-propyl). **Figure 46** shows the temperature dependence and O_2 dependence of both oxirane and methyloxirane.

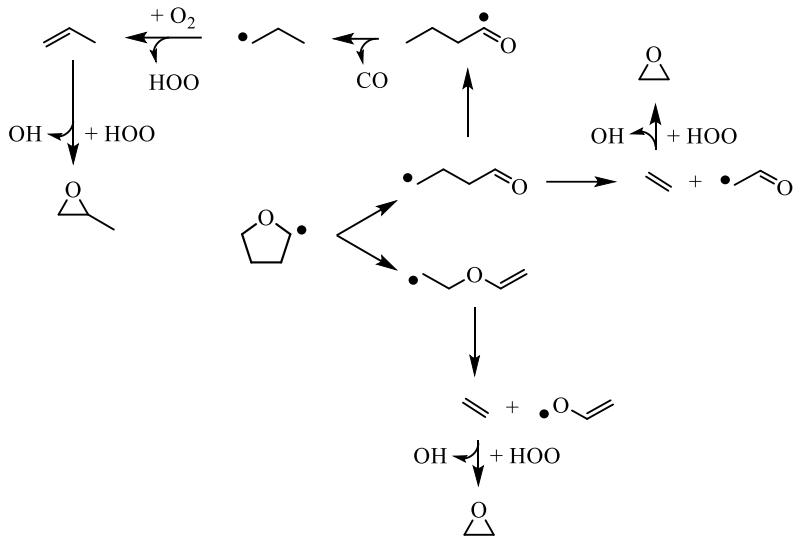

Figure 45. Oxirane and methyloxirane form via ring-opening of α-tetrahydrofuranyl radicals and subsequent epoxidation of ethene and propene, respectively.

To account for oxirane formation, Fenard et al.[34] include epoxidation of ethene and thermal decomposition of 2,3-epoxytetrahydrofuran and 3,4-epoxytetrahydrofuran, which are cyclic ether products formed exclusively from ȮOOH (**Figure 47**). However, no cyclic ethers were detected in the present experiments or in Vanhove et al.[46] The thermal stability of 2,3-epoxytetrahydrofuran 3,4-epoxytetrahydrofuran in the gas phase are unknown. Additionally, separate thermal decomposition experiments were performed on 3,4-epoxytetrahydrofuran to determine if under these conditions, oxirane is formed and the results confirm that no oxirane is formed. The synthesis of 2,3-epoxytetrahydrofuran is too complicated and therefore a chemical could not be obtained to use for thermal decomposition experiments. The possibility formation of oxirane from 2,3-epoxytetrahydrofuran remains unclear. However, the direct pathways to ethene and propene (via 1-propyl oxidation, **Figure 45**) from α-tetrahydrofuranyl provides a means for modeling the competition between radical ring-opening and reaction with O_2.

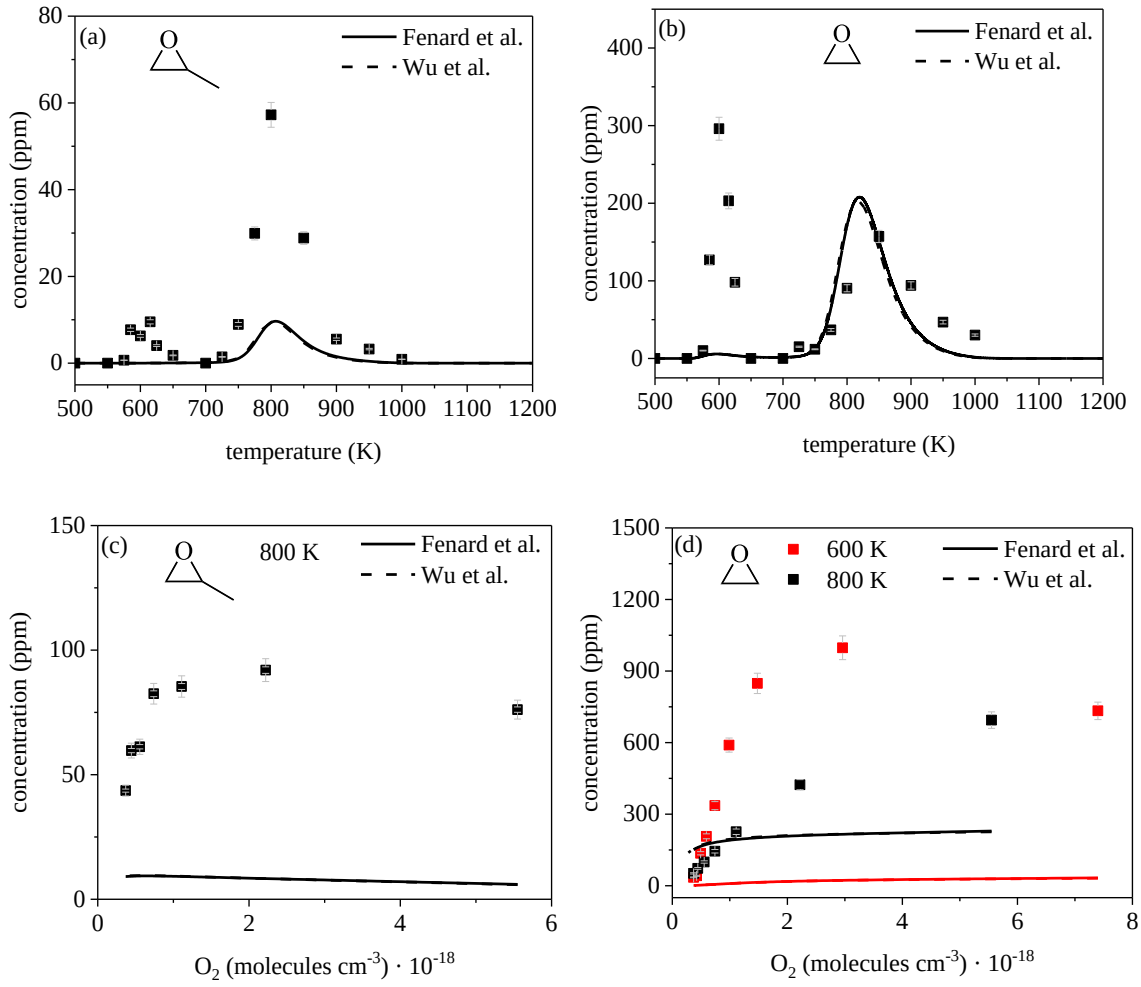

Figure 46. Temperature dependence of methyloxirane (a) and oxirane (b) measured under stoichiometric conditions; $[O_2] = 0.74 \cdot 10^{18}$ molecules $\cdot$ cm^{-3} ($\phi = 1$). NTC behavior is observed for both species around ~600 – 700 K, where oxirane exhibits much stronger behavior than methyloxirane. Oxygen-dependence of methyloxirane (c) and oxirane (d) indicate positive dependence at both temperatures for oxirane and at 800 K for methyloxirane.

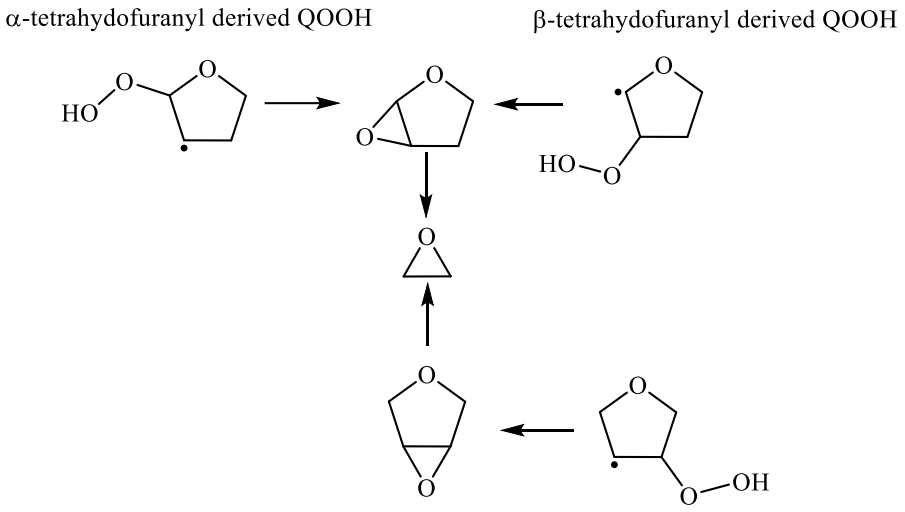

Figure 47. Reaction pathways of formation of oxirane from 2,3- and 3,4-epoxytetrahydrofuran included in Fenard et al.[34] mechanism.

While methyloxirane was detected by Vanhove et al.[34] using an RCM at high pressure (> 5 atm), the present work includes the first detection using a JSR in which species profiles for methyl oxirane are reported and can be used as benchmarks by which to improve upon mechanism development. **Figure 46a** shows the temperature dependence of methyl oxirane at stoichiometric conditions where $[O_2] = 0.74 \cdot 10^{18}$ molecules $\cdot$ cm^{-3} ($\phi = 1$). Local maxima of concentrations are at 600 K and 800 K, however both Fenard et al.[34] and Wu et al.[62] underpredict mole fractions at both temperatures, most significantly at 800 K by a factor of three at the maximum. Oxygen dependence of methyloxirane is shown in **Figure 46c**, where methyloxirane was primarily only detected at 800 K in tens of ppm with the maximum of 92 ± 4.6 ppm at $[O_2] = 2.22 \cdot 10^{-18}$ molecules cm^{-3} ($\phi = 0.25$). Both mechanisms predict the same concentrations and while the experiments exhibit clear O_2 dependence, the trend is not captured by either mechanism. One source of this discrepancy may be due to incorrectly prescribed rates for RH + $O_2 \rightarrow$ Ṙ and Ṙ + $O_2 \rightarrow$ ROȮ. While

the former reaction directly impacts the mechanism by which methyloxirane is formed, the latter is an alternative consumption pathway for Ṙ, detracting from ring-opening necessary for 1-propyl and therefore, methyloxirane formation. Additionally, upon ring-opening of α-Ṙ, the rates of subsequent elementary reactions are well understood including decomposition of $CH_3(CH_2)_2CHO \rightarrow$ 1-propyl[92,93], 1-propyl $\rightarrow$ propene[93], and epoxidation of propene to oxirane.[94,95]

Temperature dependence of oxirane is shown in **Figure 46b** where hundreds of ppm were detected and NTC behavior was observed from ~600 – 700 K. Both mechanisms slightly overpredict mole fractions centered around 800 K, but underpredict by almost 300 ppm at the local maximum at 600 K. At both temperatures, oxirane was detected in significant quantities of more than 100 ppm for $[O_2] > 0.6 \cdot 10^{18}$ molecules cm^{-3} ($\phi < 1.5$ at 600 K and $\phi < 1$ at 800 K) depicted in **Figure 46d**. Both mechanisms predict similar concentrations to one another yet do not capture the experimental O_2 dependence trend by more than an order of magnitude at 600 K and by a factor of three at 800 K.

Figure 48 shows O_2 dependence of allyl formate, which was measured by RCM by Vanhove et al.[46], but is quantified for the first time by JSR in this work. A temperature profile was not constructed as allyl formate formation was not favored at stoichiometric conditions at which all temperature measurements were taken. Allyl formate is formed exclusively from β,α'-ṪOOH, where the carbon-centered radical is on the β site on the tetrahydrofuran structure and the –OOH group is on the α site, where each group is on opposite sides of the ring, denoted by the apostrophe (**Figure 49**). β,α'-ṪOOH is derived from α-tetrahydrofuranyl radicals. Measured concentrations of allyl formate are approaching the detection limit of our instruments and therefore, it is difficult to ascertain

clear O_2-dependence trends for allyl formate, especially at higher temperature (i.e. 800 K). Still, some observations are discussed. The concentrations of allyl formate are low and approach zero towards lower [O_2], likely due to diminished rates of $\dot{R} + O_2$ causing lower rates of $\dot{Q}OOH$ formation. In contrast, towards higher [O_2], second-O_2-addition reactions consume $\dot{Q}OOH$ at higher rates, which depletes the radical pool and also diminishes the formation of allyl formate. Because the formation of allyl formate competes with second-O_2-addition to β,α'-$\dot{Q}OOH$, the quantitative species profiles, which are reported for the first time, provide a direct modeling target for assessing rate calculations of both pathways.

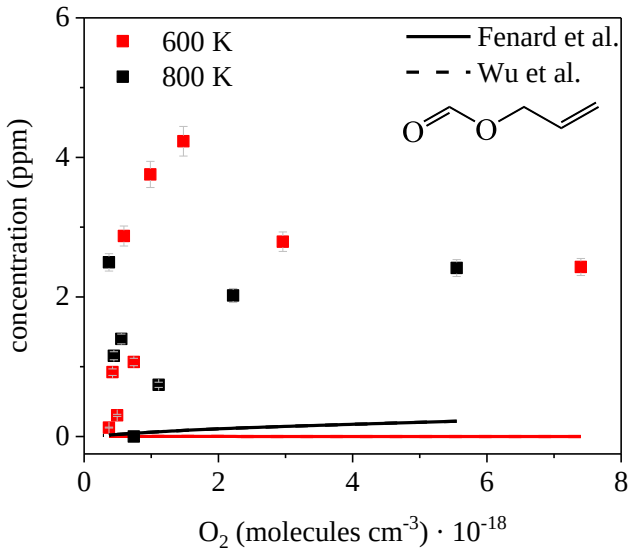

Figure 48. Oxygen dependence of allyl formate. Model predictions using the Wu et al.[62] mechanism are identical to Fenard et al.[34] and therefore indistinguishable. Measured concentrations are approaching the detection limit (~ 1 ppm) and should be scrutinized.

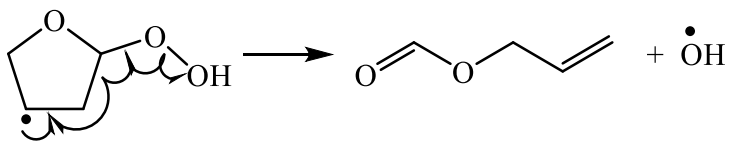

Figure 49. Formation pathway of allyl formate from β,α'-$\dot{Q}OOH$.

Following the low-temperature oxidation scheme (c.f. **Figure 5a**), two carbonyl-substituted intermediates are possible to form in tetrahydrofuran combustion – tetrahydrofuran-2-one and tetrahydrofuran-3-one (**Figure 50**). Vanhove et al.[46] reported only tetrahydrofuran-2-one in RCM experiments, yet this species was not detected in the experiments herein. Rather, tetahydrofuran-3-one was detected for the first time. **Figure 51** compares absorption and mass spectra of tetrahydrofuran-2-one with those of tetrahydrofuran-3-one, which were measured as described in Chapter 2, and confirms the identification of the species in the present work as tetrahydrofuran-3-one.

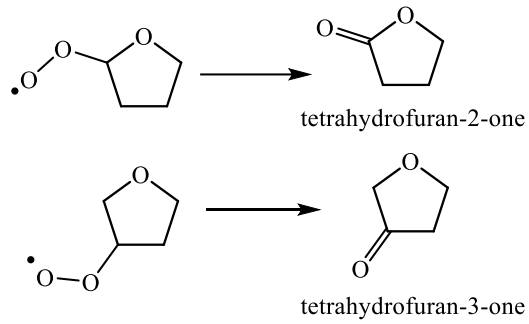

Figure 50. Tetrahydrofuran-2-one and tetrahydrofuran-3-one are possible from tetrahydrofuran combustion, the former of which was not detected in this work.

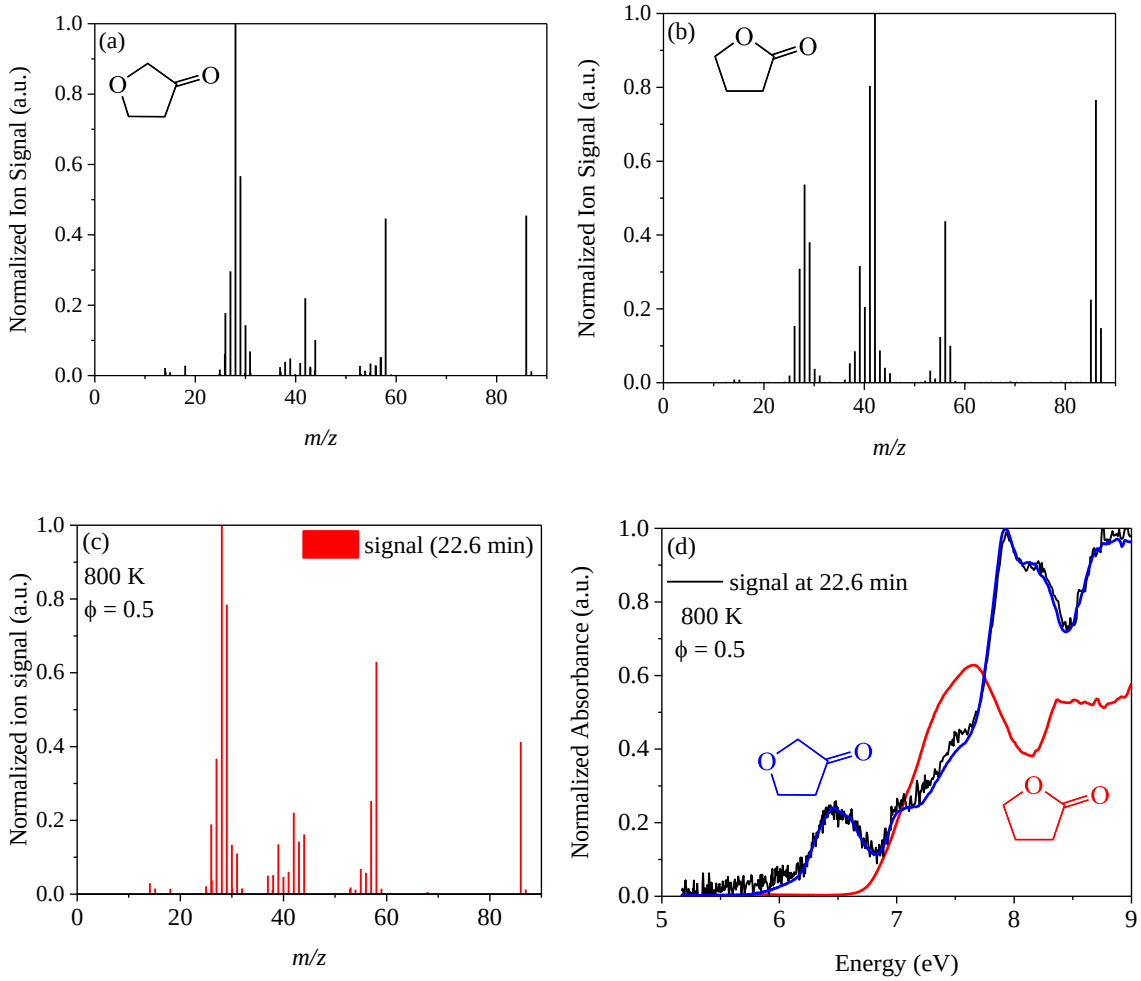

Figure 51. Mass spectra of tetrahydrofuran-3-one (a) and tetrahydrofuran-2-one (b) measured as described in Chapter 2 where fragment ion peaks are distinct allowing for identification of experimental signal (c) using mass spectra. Absorbance spectra (d) were used for identification and quantification where experimental signal (black) and reference signals of tetrahydrofuran-2-one (red) and tetrahydrofuran-3-one (blue) are shown for comparison.

Temperature and oxygen-dependence for tetrahydrofuran-3-one, which may arise from several pathways shown in **Figure 52**, are shown in **Figure 53**. Because of the strained, four-membered transition state required, formation via decomposition of ROȮ is disfavored (**Figure 52a**). Fenard et al.[34] computed a barrier height 7 kcal/mol above the Ṙ + O_2 entrance channel at the CBS-QB3 level of theory for this pathway. Another potential pathway is via ROȮ + ROȮ → carbonyl + alcohol + O_2 (**Figure 52b**). However, because

neither of the corresponding OH-substituted tetrahydrofuran isomers were detected, a plausible third route to form tetrahydrofuran-3-one is as follows: H-abstraction by β-ROȮ, yielding β-ROOH, which then undergoes H-abstraction by ȮH or HOȮ from the tertiary carbon that leads to a highly unstable α-ȮOOH structure that decomposes into tetrahydrofuran-3-one + ȮH (**Figure 52c**).

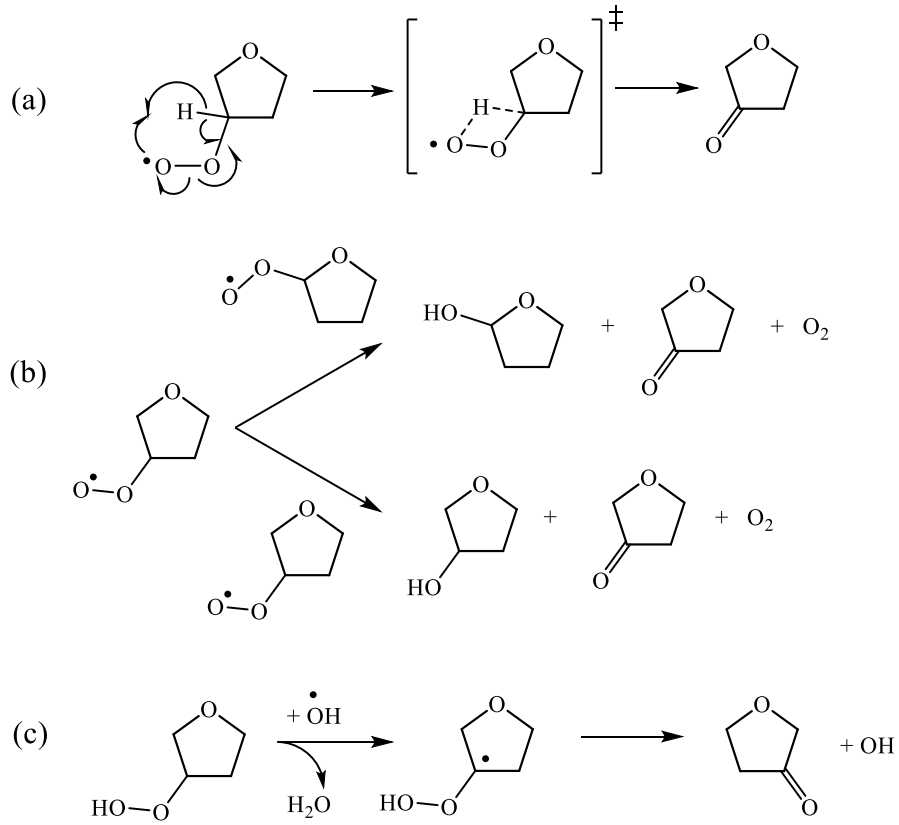

Figure 52. Potential pathways of tetrahydrofuran-3-one formation where the four-membered transition state in the decomposition of ROȮ (a) is unfavored, and co-products of reaction (b), 2- or 3-hydroxytetrahydrofuran, were not detected in current experiments, suggesting reaction (c) is more plausible.

Model predictions using the mechanisms of Fenard et al.[34] and Wu et al.[62] capture qualitative trends in both temperature and oxygen-dependence for tetrahydrofuran-3-one. However, both models severely underpredict concentrations by a factor of 10^5 at 600 K and 10^3 at 800K. This could be attributed to a lack of understanding of tetrahydrofuran-3-one formation pathways as the primary formation pathway indicated by rate-of-production analyses is a single step reaction of β-ROȮ → tetrahydrofuran-3-one + ȮH (**Figure 54**). Additionally, mole fractions are underpredicted to a greater degree at lower temperatures, which may be because uncertainty in peroxyradical reaction rates is compounded as these reactions are more dominant at lower temperatures.

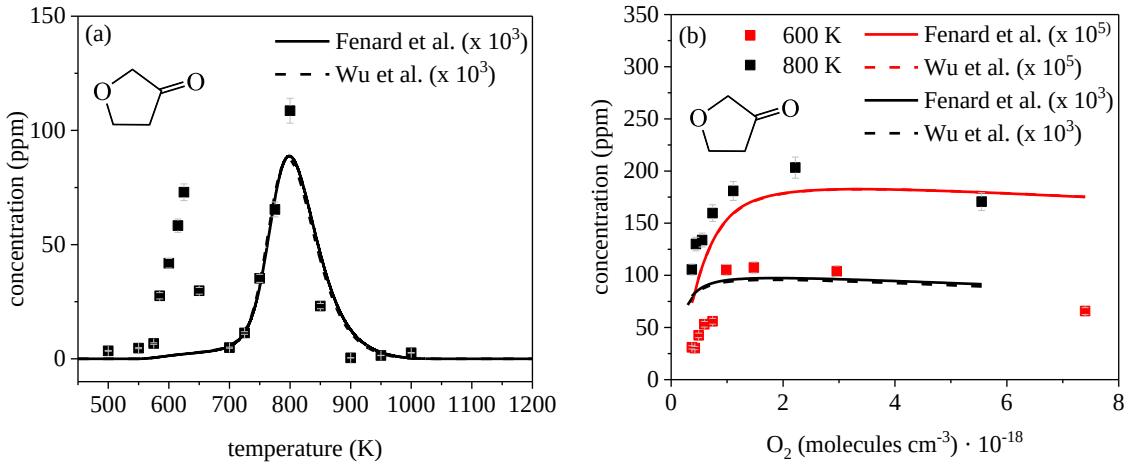

Figure 53. Temperature dependence (a) where model predictions are multiplied by 10^3 to maintain scale with experimental results. O_2 dependence (b) of tetrahydrofuran-3-one at 600 K and 800 K. Predictions using mechanisms of Fenard et al.[34] and Wu et al.[62] are < 1 ppm and are therefore scaled by 10^5 for predictions at 600 K and by 10^3 for those at 800 K.

Top 3 Reactions	Rate-of-production yield at 600 K		
	ϕ = 0.1	ϕ = 0.25	ϕ = 2
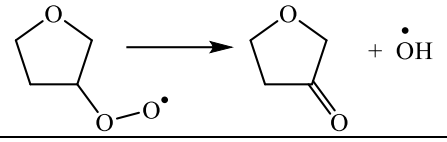	2.51E-14	2.42E-14	7.69E-15
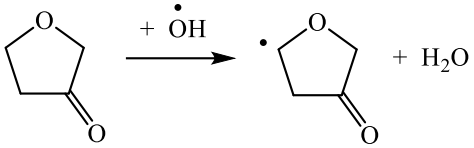	-3.38E-15	-2.36E-15	-1.01E-16
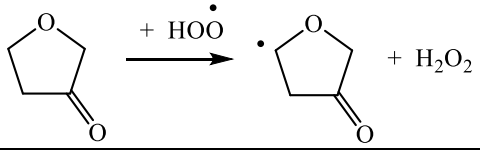	-1.85E-15	-1.46E-15	-1.22E-16

Top 3 Reactions	Rate-of-production yield at 800 K		
	ϕ = 0.1	ϕ = 0.25	ϕ = 2
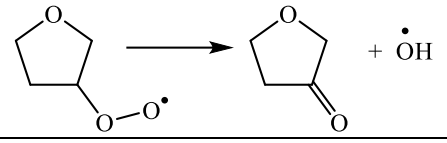	2.52E-12	2.48E-12	1.55E-12
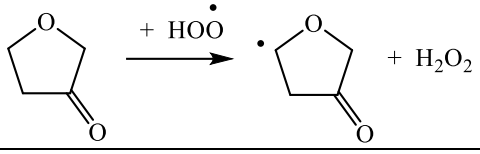	-7.97E-13	-7.65E-13	-4.15E-13
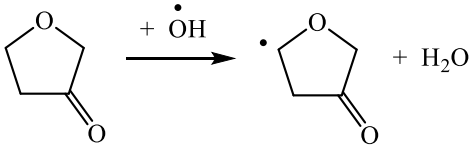	-4.63E-13	-4.19E-13	-2.21E-13

Figure 54. Rate-of-production analyses for tetrahydrofuran-3-one of the top three reactions at 600 and 800 K where the primary formation pathway is that of β-ROȮ → tetrahydrofuran-3-one + ȮH. Negative rate-of-production yields indicate that the reaction shown occurs in the reverse direction.

Figure 55a shows VUV spectra for tetrahydrofuran-3-one and butanedial, both of which were detected directly and quantified for the first time. **Figure 55b** is a representative spectrum for butanedial deconvolved from the spectrum in Figure 20a and used subsequently for quantification of temperature dependence (**Figure 55c**) and O_2

dependence (**Figure 55d**). The measurement procedure for the reference spectrum and quantification procedure for butanedial was as follows. Because butanedial is 40% aqueous solution, measuring a direct and isolated quantitative reference was not possible. Instead a ternary gas phase mixture was made composed of butanedial and water (from the aqueous chemical) diluted in N_2. The procedure to make this mixture was identical to that outlined in Section 2. The components were separated by gas-chromatography and detected via VUV absorption. Using a separate reference of water with a known concentration, the partial pressure of the individual components in the ternary mixture could be back-calculated based on Dalton's Law (**Equation 7**), and therefore concentrations could be assigned each component in the mixture. The isolated VUV absorption spectrum measured for butanedial from the ternary mixture was associated with the concentration calculated above and was used as the reference to quantify butanedial signal detected experimentally. While butanedial did co-elute with tetrahydrofuran-3-one, the process of deconvolution outlined in Section 2 allowed for isolation of butanedial signal, which was quantified using the reference as described above.

$$P_{cylinder} = P_{butanedial} + P_{water} + P_{nitrogen} \quad (7)$$

The temperature dependence of butanedial (**Figure 55c**) shows peak yields occurring near ~625 K and ~775 K, the latter of which is captured by model predictions using Fenard et al.[34] and Wu et al.[62] Quantitative disparities are evident in both the onset temperature where butanedial is detected, ~550 K (model) and ~580 K (experiment), and in the temperature at which peak yield occurs – both of which may result from inaccurate rates of ring-opening for α,α'-ȮOOH → butanedial + ȮH (c.f. **Figure 9**), where the

localized radical and the –OOH group reside on opposing carbon atoms adjacent to the ether group (i.e. α carbon). Oxygen dependence of butanedial concentration at 600 K and 800 K is shown in **Figure 55d**. Model predictions at each temperature were reduced by a factor of six in **Figure 55d** to maintain scale with experimental results. At both temperatures, the concentration of butanedial increases with increasing oxygen concentration until reaching an inflection point occurring near stoichiometric concentration of O_2, after which butanedial concentration decreases. The inflection is the result of a balance of competing reactions derived initially from α-tetrahydrofuranyl radicals, α-Ṙ, that are directly affected by temperature and oxygen concentration. Namely, the ring-opening reaction α-Ṙ → products, the association reaction α-Ṙ + O_2 → α-RȮ, the ring-opening reaction α,α'-ȮOOH → butanedial + ȮH, and second-O_2 addition that consume α,α'-ȮOOH and inhibit butanedial formation.

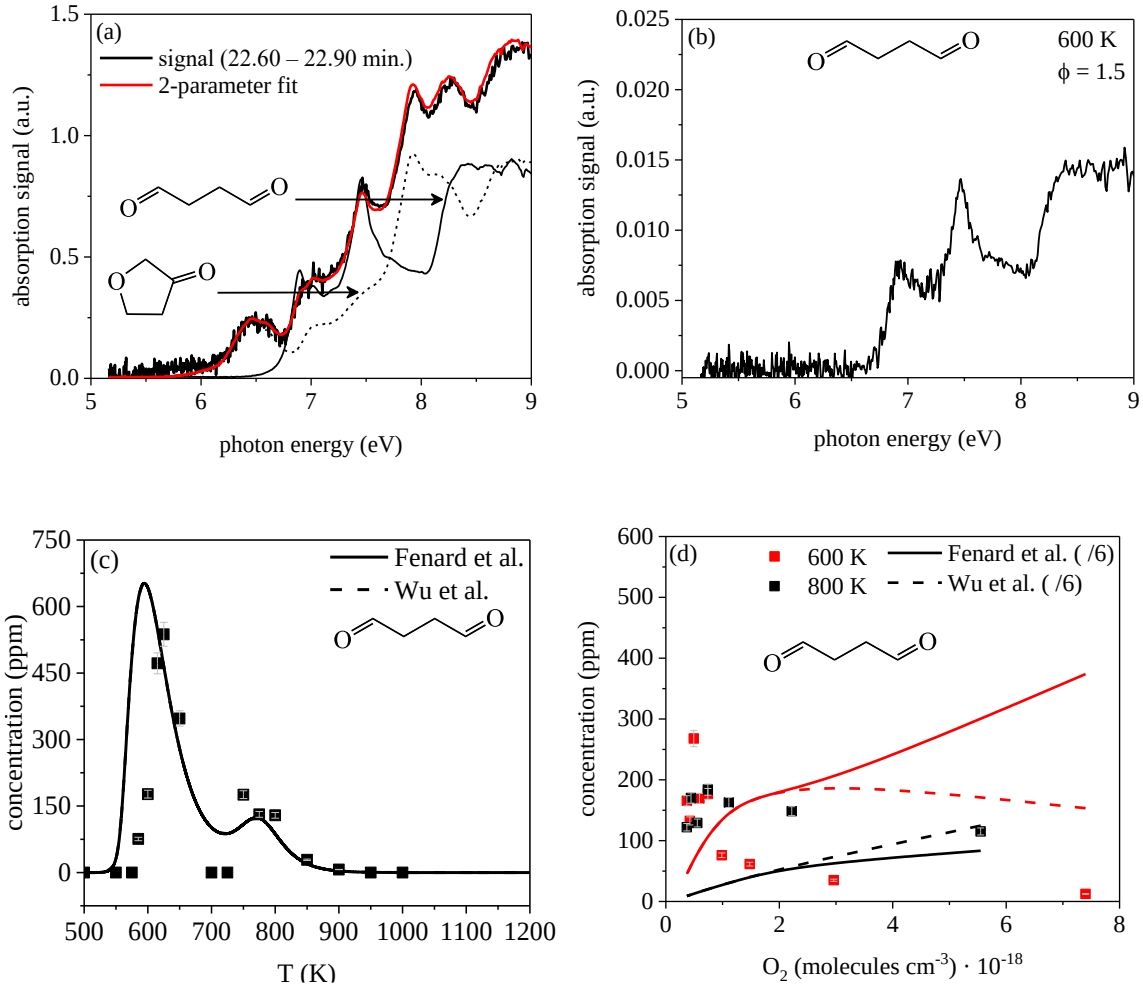

Figure 55. (a) VUV absorption signal measured over the retention time window 22.60 – 22.90 min. and comparison to reference spectra of butanedial and tetrahydrofuran-3-one at 800 K, $[O_2] = 0.74 \cdot 10^{18}$ molecules · cm^{-3} ($\phi = 1$). (b) Extracted absorption spectrum of butanedial from co-eluted signal. (c) Temperature dependence of butanedial concentration at $[O_2] = 0.74 \cdot 10^{18}$ molecules · cm^{-3}. (d) O_2-dependence of butanedial concentration at 600 K and 800 K where model predictions were reduced by a factor of six to maintain scale of experimental results.

4.2 DISCUSSION

The main purpose of the present work is to examine the O_2 dependence on partially oxidized intermediates from tetrahydrofuran combustion in order to provide modeling targets and to understand the implication on the balance between ring-opening of initial tetrahydrofuranyl radicals and reaction with O_2. The formation of α-tetrahydrofuranyl is

favored because the electronegativity of the C–O bond in the ether group draws electrons from the C–H bond in the α position and reduces the bond dissociation energy by ~4.5 kcal/mol.[96] From Giri et al.[97], H-abstraction from the α site is favored over the β site by more than 2:1 below 800 K. As such, a significant portion of the species detected in the present experiments are derived initially from α-tetrahydrofuranyl. However, β radicals may also contribute to the formation of ROOH (cf. **Figure 53**).

The balance of contributions from the three pathways forming dihydrofuran isomers, direct from ROȮ, sequential via ROȮ to ȮOOH, and formally direct from $\dot{R} + O_2$ remains unclear (c.f. **Figure 38**). With increasing O_2, the rate of $\dot{R} + O_2$ also increases, which increases the likelihood of accessing the ȮOOH well in the sequential path. However, an increase in the rate of $\dot{R} + O_2$ could also facilitate the direct formation pathway from ROȮ and formally direct from $\dot{R} + O_2$. The O_2-dependent measurements herein provide modeling targets for determining the extent to which the three pathways are contributing to dihydrofuran formation at 1 atm.

Both dihydrofuran isomers exhibit an increase in concentration with $[O_2]$ from 600 K to 800 K. However, 2,3-dihydrofuran decreases at oxygen concentrations above stoichiometric conditions ($[O_2] = 0.74 \cdot 10^{-18}$ molecules $\cdot$ cm^{-3}, or $\phi = 1$) at 600 K indicating either that at higher $[O_2]$, HOO-elimination from tetrahydrofuranyl by O_2 is diminished or that consumption reactions of 2,3-dihydrofuran are more $[O_2]$ dependent than is prescribed in the chemical kinetics mechanisms. Additionally, because negative O_2-dependence behavior is not observed at 800 K, this may indicate that at higher temperature, 2,3-dihydrofuran is less susceptible to low-temperature combustion pathway competition.

Quantitative discrepancies exist between the experiments and model predictions for the dihydrofuran isomers. To examine differences between Fenard et al.[34] and Wu et al.[62] models, rate-of-production analyses were conducted on several species at 600 K and 800 K oxygen concentrations corresponding to ϕ = 0.25, 1, and 2, where selected equivalence ratios represented local concentration maxima for the majority of species, stoichiometric conditions, and the high-end extreme, respectively (**Figure 56**). Fenard et al.[34] predicts that 2,3-dihydrofuran primarily undergoes H-abstraction to form 2,3-dihydrofuranyl radical, which can either form furan upon reaction with O_2 or undergo ring-opening into C_2H_4 + CH_2O + H$\dot{C}$O. Wu et al.[62] included new ring-opening reactions that were not in the initial Fenard et al.[34] mechanism. Although, due to a lack of measurements, the reactions were modeled using a lumping procedure as described in Chapters 1 and 3. Despite the changes, the rate-of-production analyses indicated that the pathways to furan were more dominant than ring-opening reactions. Therefore to improve upon model predictions, it may be helpful to scrutinize the calculated rate for 2,3-dihydrofuranyl → furan, which was adopted from Dubnikova et al.[99] and expand lumped mechanisms of 2,3-dihydrofuran ring-opening. In addition, including a revised sub-mechanism for 2,5-dihydrofuran reactions and specifically for 2,5-dihydrofuranyl radical ring-opening pathways may improve agreement.

One specific aspect that remains unclear for dihydrofuran reactions is the competition for $\dot{O}$H between abstraction pathways and addition pathways, the latter leading to two possible carbon-centered, OH-substituted radicals 2-hydroxy-tetrahydrofuran-3-yl or 3-hydroxy-tetrahydrofuran-2-yl. OH-addition to 2,3-dihydrofuran is neglected in Fenard et al.[34] (only abstraction and disproportionation reactions are included).

a)

600 K	800 K	ϕ = 0.25
-1.26E-10	-5.25E-10	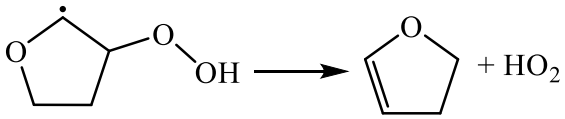
5.37E-10	3.22E-10	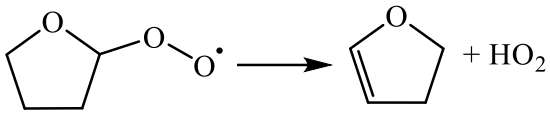
3.10E-11	5.14E-10	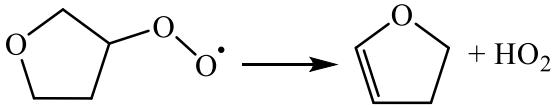
1.67E-09	6.57E-10	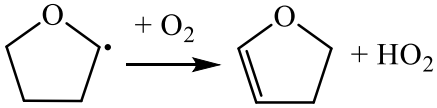
2.59E-10	2.95E-09	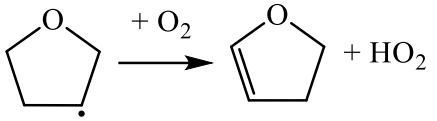
-3.58E-12	1.23E-10	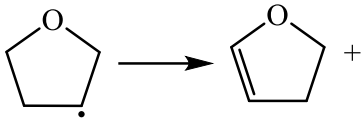
-1.90E-10	-3.99E-10	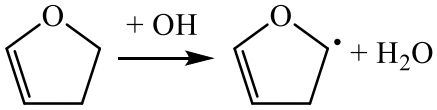
-6.69E-10	-1.03E-09	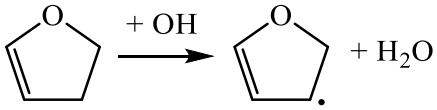
-3.23E-10	-4.59E-10	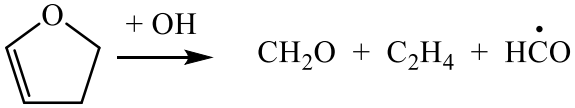
-8.42E-15	-4.93E-10	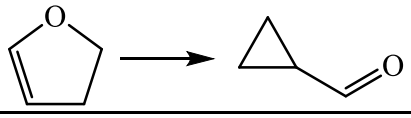

b)

600 K	800 K	ϕ = 1
-3.46E-11	-3.91E-10	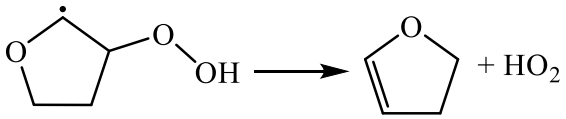
1.90E-11	4.24E-10	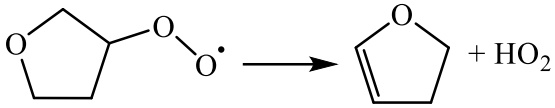
5.96E-10	1.52E-10	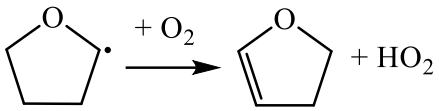
1.22E-10	2.41E-09	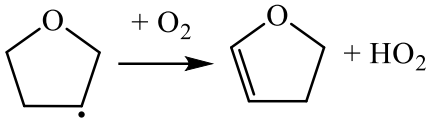
-7.06E-13	5.63E-10	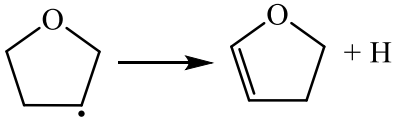
-2.05E-12	-1.02E-10	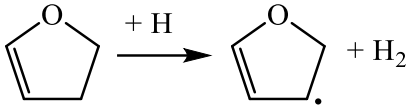
-3.63E-11	-2.91E-10	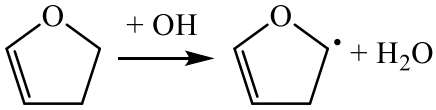
-1.28E-10	-7.50E-10	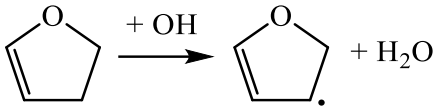
-6.19E-11	-3.35E-10	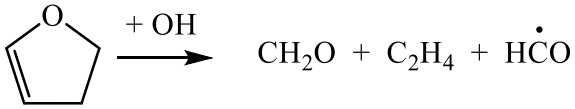
-5.57E-15	-4.35E-10	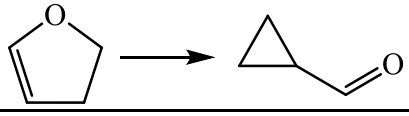

c)

600 K	800 K	ϕ = 2
-3.46E-11	-3.91E-10	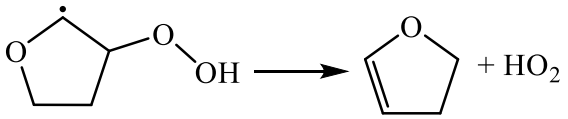
1.90E-11	4.24E-10	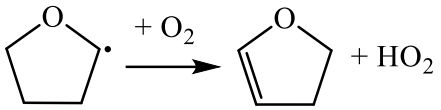
5.96E-10	1.52E-10	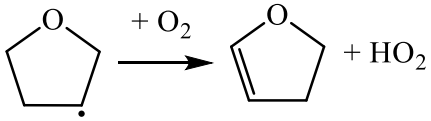
1.22E-10	2.41E-09	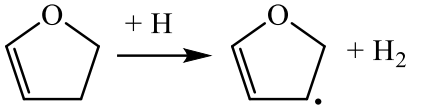
-7.06E-13	5.63E-10	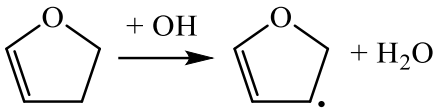
-2.05E-12	-1.02E-10	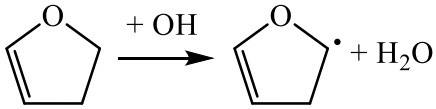
-3.63E-11	-2.91E-10	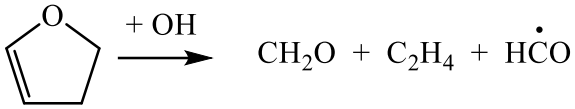
-1.28E-10	-7.50E-10	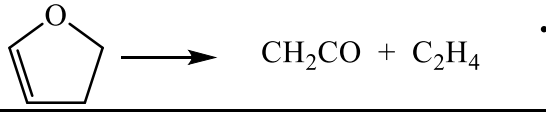
-6.19E-11	-3.35E-10	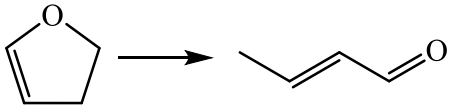
-5.57E-15	-4.35E-10	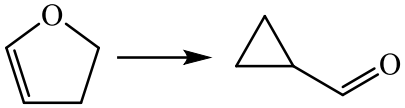

Figure 56. Rate-of-production analyses comparison for 2,3-dihydrofuran (cy(OC*CCC)) predictions from Fenard et al.[34] and Wu et al.[62] at ϕ of 0.25 (a), 1 (b), and 2 (c) at 600 and 800 K. Although, new sub-mechanisms were added by Wu et al.[62], rate-of-production analyses produced identical results to Fenard et al.[34]

To improve predictions of furan concentration, Wu et al.[62] included additional H-abstraction and ring-opening reactions. The large discrepancy observed with the present experiments for furan is likely due to deficiencies in the rates and reactions prescribed for dihydrofuranyl + O_2 and other reactions. The experiments show strong O_2 dependence indicating that with high [O_2], furan formation via HOO-elimination from dihydrofuran isomers is favored or, alternatively, subsequent consumption pathways of furan are deficient in the mechanism. Based on rate-of-production analyses, the main formation pathway is prescribed to HOO-elimination and H_2O_2-elimination from dihydrofuran radicals at 600 K and H_2-elimination from 2,5-dihydrofuran at 800 K (**Figure 57**). However, in comparing O_2-dependence of furan to that of dihydrofuran isomers, a direct and isolated relationship is not observed, rather an unfolding of the competition of pathways. At 600 K, the concentration of furan increases with increasing O_2, where 2,3-dihydrofuran and 2,5-dihydrofuran increase then decrease with O_2. Therefore, the dihydrofuran isomers are consumed to form furan. However, at 800 K, furan and both dihydrofuran isomers increase with O_2, indicating that the formation and consumption pathways of both dihydrofuran isomers and furan unfold in a different way than at 600 K.

a)

Top 5 Reactions	Rate-of-production yield at 600 K		
	ϕ = 0.25	ϕ = 1	ϕ = 2
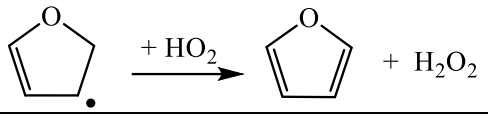	2.51E-10	4.76E-11	9.79E-12
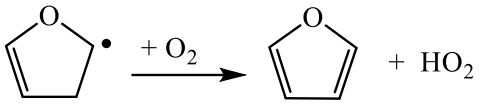	1.81E-10	3.20E-11	6.09E-12
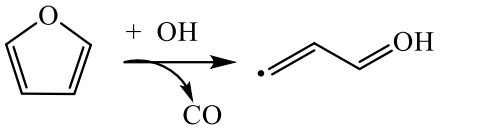	2.71E-11	7.49E-12	1.79E-12
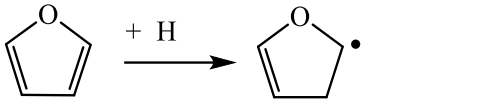	2.83E-12	2.81E-12	1.04E-12
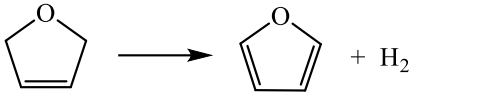	1.56E-15	1.47E-15	8.01E-16

b)

Top 5 Reactions	Rate-of-production yield at 800 K		
	ϕ = 0.25	ϕ = 1	ϕ = 2
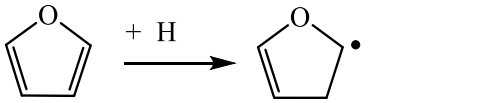	4.32E-10	3.70E-10	3.21E-10
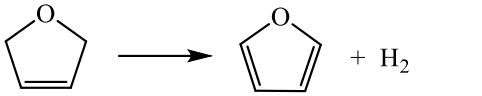	1.76E-10	1.65E-10	1.40E-10
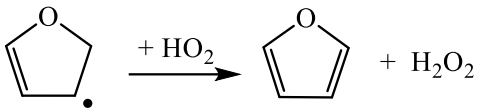	4.86E-11	3.88E-11	3.38E-11
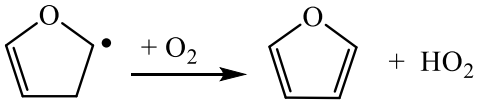	7.45E-11	1.39E-11	5.42E-12
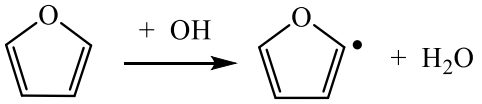	-9.66E-13	-7.94E-13	9.93E-13

Figure 57. Rate-of-production analyses for furan predictions from Fenard et al.[34] and Wu et al.[62] at ϕ of 0.25, 1, and 2 at 600 K (a) and 800 K (b). Although, new sub-mechanisms were added by Wu et al.[62], rate-of-production analyses produced identical results to Fenard et al.[34]

Lifshitz[91] proposed rearrangement of 2,3-dihydrofuran as the mechanism responsible for cyclopropane carboxaldehyde, which can subsequently isomerize to form 2-butenal (**Figure 58**). At 600 K, cyclopropane carboxaldehyde was predicted at ppb levels and was not experimentally detected. At 800 K, the Fenard et al.[34] mechanism overpredicts cyclopropane carboxaldehyde where the revisions by Wu et al.[62] provided some improvement compared with the experiments herein. The differences in the model predictions is potentially attributed to the revised sub-mechanism for 2,3-dihydrofuran that includes consumption reactions that were previously not considered and consume some of the flux towards the cyclopropane carboxaldehyde pathway. Within the mechanism, the pathway from 2,3-dihydrofuran to cyclopropane carboxaldehyde is a single, concerted step. Because similar quantities were detected in both the present experiments and the JSR experiments in Vanhove et al.[46], the consistency indicates that the quantity produced is reproducible. However, because the model predictions do not capture O_2-dependence nor quantitative amounts, rates of elementary reactions leading to cyclopropane carboxaldehyde may require scrutiny, including RH + O_2 → Ṙ, Ṙ + O_2 → ROȮ, ROȮ → 2,3-dihydrofuran, and 2,3-dihydrofuran → cyclopropane carboxaldehyde, where Ṙ and ROȮ may be α- or β-derived. This network of reactions is especially important to understand given the importance of conjugate alkenes in cyclic ether oxidation.

Moreover, cyclopropane carboxaldehyde and 2,3-dihydrofuran are also connected to 2-butenal, which was not detected in the present experiments, via a network of rearrangements (**Figure 58**). Vanhove et al.[46] detected 2-butenal at relatively low concentrations (~10 ppm). Because 2-butenal was not detected in the present experiments, this may indicate that rather than the rearrangement reactions not occurring, that the

experimental conditions were not favorable for steady state detection of 2-butenal. Namely, residence time and pressure were unchanged in the current experiments, which could facilitate 2-butenal detection. For example, it is possible that 2-butenal requires a longer time to form at concentrations within our detection limit, so a residence time of 4 seconds rather than 2 seconds could facilitate detection of 2-butenal.

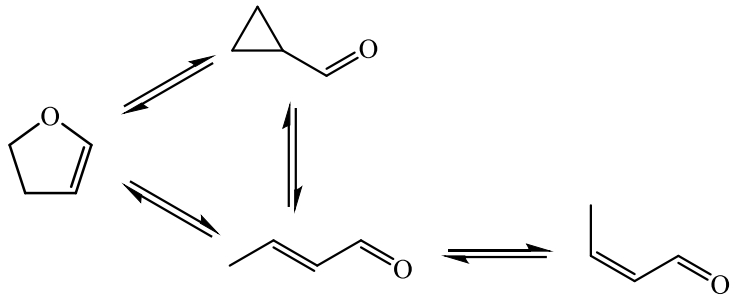

Figure 58. Rearrangements that can occur between 2,3-dihydrofuran, cyclopropane carboxaldehyde, and *trans*- and *cis*-2-butenal.

Aside from the formation of 2,3-dihydrofuran and 2,5-dihydrofuran, tetrahydrofuranyl radicals can undergo O_2-addition to form peroxy radicals or ring-opening reactions. In the case of α-tetrahydrofuranyl, the latter leads to methyloxirane (derived from epoxidation of propene) and oxirane (formed via epoxidation of ethene). Fenard et al.[34] note that competition from $\dot{R} + O_2$ outcompetes epoxidation. However, epoxidation rates are well-characterized[94,95,100] and the mechanism employs rate rules for alkyl radicals from corresponding reactions of 2-buyltetrahydrofuran calculated by Cai et al.[87] Because rates of O_2-addition to cyclic ether radicals are largely unknown at combustion conditions[26], high-level theoretical computations using variable-reaction-coordinate transition state theory (VRC-TST) are required. Doner et al.[101] approximated rates of O_2-addition to stereoisomers of 2,4-dimethyloxetanyl using phase-space theory, yet a broader

series of calculations are required given the diversity of molecular structure of cyclic ethers.

Despite discrepancies between model predictions and experimental data for tetrahydrofuran-3-one and butanedial, the first set of speciation data was measured in this work to provide a benchmark for future computational work. Specifically, the role of ROOH reactions as they pertain to tetrahydrofuran-3-one formation, remain unclear. Additionally, the sensitivity of butanedial to ȮOOH unimolecular and bimolecular reaction competition remains a deficiency within the mechanisms.

Overall, in order to improve agreement between experimental results and model predictions, a nuanced, species-specific approach is needed. Rates of RH + O_2 → Ṙ and Ṙ + O_2 → ROȮ should be scrutinized as subsequent pathways cannot be properly modeled should these rates require attention via higher-level theory calculations. Additionally, improving rates of ring-opening reactions of α-Ṙ could have a significant quantitative impact on several species that were detected at tens to hundreds of ppm (i.e. oxirane, methyloxirane, butanedial) and underpredicted by several orders of magnitude where α-Ṙ ring-opening either directly leads to oxirane and methyloxirane or reduces the concentration of α-Ṙ needed to form intermediates that are central to other pathways such as α,α'-ȮOOH in butanedial formation.

CHAPTER 5

CONCLUSIONS AND PROJECTIONS

Isomer-resolved speciation measurements were conducted on tetrahydrofuran oxidation using a jet-stirred reactor at 810 Torr from 500 – 900 K and a range of oxygen concentrations spanning one order of magnitude, which led to the first measurements of several species important to chemical kinetics modeling of tetrahydrofuran and relevant to *n*-butane cyclic ether consumption mechanism description (butanedial, allyl formate, and tetrahydrofuran-3-one). This work provided the first speciation measurements for butanedial, allyl formate, tetrahydrofuran-3-one, and methyloxirane. The measurements of O_2-dependent and temperature-dependent trends in species profiles provide insight into understanding the balance of reactions that tetrahydrofuranyl radicals undergo, such as ring-opening versus reaction with O_2. This work is the first to target O_2-dependence for this purpose to gain insight on reaction mechanisms. For example, because the formation of butanedial occurs exclusively via ȮOOH ring-opening the direct measurements herein provide a means for assessing rates prescribed in chemical kinetics mechanisms. Additionally, the work herein examines how chemical kinetics mechanisms are able to predict species concentrations over a range of O_2 concentrations to scrutinize the fidelity of current mechanisms. Because modeling disparities are evident most notably in the O_2-dependent comparisons, modeling efforts are required to determine the fate of ȮH radicals including addition to dihydrofuran isomers. Given the discrepancies of O_2-dependence speciation predictions of the work herein and given similar conclusions from the modeling

work done by Lockwood and Labbe[75], higher level theory is necessary to improve upon rate calculations to reduce uncertainty in rates for ROȮ → ȮOOH, the initiation step of tetrahydrofuran, and ROȮ ring-opening reactions. In addition, the role of ROOH species, from which tetrahydrofuran-3-one is conceivably formed in significant quantities, remains unclear. Finally, because tetrahydrofuran is a low-temperature cyclic ether product of *n*-butane, once chemical kinetics mechanisms of tetrahydrofuran are improved, so too can sub-mechanisms of tetrahydrofuran in *n*-butane chemical kinetics mechanisms.

Additional experiments may provide clarity on allyl formate speciation. Specifically, because at the current conditions allyl formate is in low steady-state concentration near our detection limit, increasing the residence time may increase the steady-state concentration by allowing more time for reaction to occur. Additionally, increasing the initial concentration of tetrahydrofuran would increase steady-state concentration of all products, which would not only clarify a trend for allyl formate, but it would increase concentrations of all products including those derived from β-tetrahydrofuranyl. This would be helpful because in comparison to α-tetrahydrofuranyl, β-tetrahydrofuranyl is less favored so products derived from β-tetrahydrofuranyl are in lower steady-state concentrations. Species that are β-derived are still important in ketohydroperoxide formation and are underpredicted by several orders of magnitude in this work and in that of Hansen et al.[72]

In order to understand the influence of the ether group on low-temperature combustion pathways, jet-stirred reactor experiments on cyclopentane, the hydrocarbon analog of tetrahydrofuran, are ongoing. Preliminary results from these experiments indicate that low-temperature combustion behavior is diminished at temperatures less than 700 K

in comparison to tetrahydrofuran, which is indicated by species profiles that only have a singular local maximum concentration at ~850 K for cyclopentane oxidation products such as cyclopentadiene, 1,2-epoxycyclopentane, and acrolein. Additionally, while no cyclic ether products were detected for tetrahydrofuran oxidation in this work or in Vanhove et al.[46], 1,2-epoxycyclopentane, one of two possible cyclic ether products for cyclopentane, has been detected indicating that without the ether group, cyclic ether products are able to more readily form or are less likely to decompose. The ongoing cyclopentane work will provide further insight into the effect of ethers on low-temperature combustion pathways.

REFERENCES

(1) Energy Information Agency. *Annual Energy Outlook 2021 with Projections into 2050*; 2022; p 33.
(2) Senecal, P. K.; Leach, F. Diversity in Transportation: Why a Mix of Propulsion Technologies Is the Way Forward for the Future Fleet. *Results in Engineering* **2019**, *4*, 100060. https://doi.org/10.1016/j.rineng.2019.100060.
(3) *Inventory of U.S. Greenhouse Gas Emissions and Sinks: 1990-2020*; EPA 430-R-22-003; United States Environmental Protection Agency.
(4) Alleman, T. L.; McCormick, R. L.; Christensen, E. D.; Fioroni, G.; Moriart, K.; Yanowitz, J. Biodiesel Handling and Use Guide (Fifth Edition). 72.
(5) House, T. W. *FACT SHEET: President Biden Announces Steps to Drive American Leadership Forward on Clean Cars and Trucks*. The White House. https://www.whitehouse.gov/briefing-room/statements-releases/2021/08/05/fact-sheet-president-biden-announces-steps-to-drive-american-leadership-forward-on-clean-cars-and-trucks/ (accessed 2022-09-27).
(6) Perkins, T. Biden Talks up Electric Vehicle Revolution – but Is America Ready to Give up Gas? *The Guardian*. September 17, 2022.
(7) *Electrifying Transportation to Benefit Every American*. Energy.gov. https://www.energy.gov/eere/articles/electrifying-transportation-benefit-every-american (accessed 2022-09-27).
(8) Senecal, K.; Leach, F. *Racing Toward Zero: The Untold Story of Driving Green*; SAE International, 2021.
(9) Morris, J. *Sustainable Transport Is About Much More Than Electrification*. Forbes. https://www.forbes.com/sites/jamesmorris/2022/09/17/sustainable-transport-is-about-much-more-than-electrification/ (accessed 2022-09-27).
(10) Egeskog, A.; Hagdahl, K.-H.; Krewer, C.; Rade, I.; Bolin, L. *Carbon Footprint Report - Battery Electric XC40 Recharge and the XC40 ICE*; Volvo Cars.
(11) West, K. Carmakers' Electric Dreams Depend on Supplies of Rare Minerals. *The Guardian* 4.
(12) Gonzalez, A.; de Haan, E. *The Battery Paradox: How the Electric Vehicle Boom Is Draining Communities and the Planet*; Centre for Research on Multinational Corporations (SOMO), 2020.
(13) *Eco-friendly biofuels made from food waste could cut "flight shame" among air travelers*. NBC News. https://www.nbcnews.com/mach/science/eco-friendly-biofuels-made-food-waste-could-cut-flight-shame-ncna1030801 (accessed 2022-09-25).
(14) JBEI. *Bright Skies for Plant-Based Jet Fuels*. jbei.org. https://www.jbei.org/bright-skies-for-biofuels/ (accessed 2022-09-25).
(15) Salvachúa, D.; Saboe, P. O.; Nelson, R. S.; Singer, C.; McNamara, I.; del Cerro, C.; Chou, Y.-C.; Mohagheghi, A.; Peterson, D. J.; Haugen, S.; Cleveland, N. S.; Monroe, H. R.; Guarnieri, M. T.; Tan, E. C. D.; Beckham, G. T.; Karp, E. M.;

Linger, J. G. Process Intensification for the Biological Production of the Fuel Precursor Butyric Acid from Biomass. *Cell Reports Physical Science* **2021**, *2* (10), 100587. https://doi.org/10.1016/j.xcrp.2021.100587.
(16) de Jong, S.; Antonissen, K.; Hoefnagels, R.; Lonza, L.; Wang, M.; Faaij, A.; Junginger, M. Life-Cycle Analysis of Greenhouse Gas Emissions from Renewable Jet Fuel Production. *Biotechnol Biofuels* **2017**, *10* (1), 64. https://doi.org/10.1186/s13068-017-0739-7.
(17) Wu, W.; Liu, F.; Singh, S. Toward Engineering *E. Coli* with an Autoregulatory System for Lignin Valorization. *Proc. Natl. Acad. Sci. U.S.A.* **2018**, *115* (12), 2970–2975. https://doi.org/10.1073/pnas.1720129115.
(18) Al-Hasan, M. Effect of Ethanol–Unleaded Gasoline Blends on Engine Performance and Exhaust Emission. *M. Al* **2003**, 15.
(19) Thomas, J. F.; West, B. H.; Huff, S. P. *Effects of High Octane Ethanol Blends on Four Legacy Flex-Fuel Vehicles, and a Turbocharged GDI Vehicle*; ORNL/TM-2015/116, 1185964; 2015; p ORNL/TM-2015/116, 1185964. https://doi.org/10.2172/1185964.
(20) Rodríguez-Antón, L. M.; Gutíerrez-Martín, F.; Doce, Y. Physical Properties of Gasoline, Isobutanol and ETBE Binary Blends in Comparison with Gasoline Ethanol Blends. *Fuel* **2016**, *166*, 73–78. https://doi.org/10.1016/j.fuel.2015.10.106.
(21) Yan, X.; Inderwildi, O. R.; King, D. A.; Boies, A. M. Effects of Ethanol on Vehicle Energy Efficiency and Implications on Ethanol Life-Cycle Greenhouse Gas Analysis. *Environ. Sci. Technol.* **2013**, *47* (11), 5535–5544. https://doi.org/10.1021/es305209a.
(22) Bhutto, A. W.; Qureshi, K.; Abro, R.; Harijan, K.; Zhao, Z.; Bazmi, A. A.; Abbas, T.; Yu, G. Progress in the Production of Biomass-to-Liquid Biofuels to Decarbonize the Transport Sector – Prospects and Challenges. *RSC Advances* **2016**, *6* (38), 32140–32170. https://doi.org/10.1039/C5RA26459F.
(23) Regalbuto, J. R. Cellulosic Biofuels--Got Gasoline? *Science* **2009**, *325* (5942), 822–824. https://doi.org/10.1126/science.1174581.
(24) Schmidt, L. D.; Dauenhauer, P. J. Hybrid Routes to Biofuels. *Nature* **2007**, *447* (7147), 914–915. https://doi.org/10.1038/447914a.
(25) Coyle, W. T. Near-Term Challenges and Implications for Agriculture. **2009**, 26.
(26) Rotavera, B.; Taatjes, C. A. Influence of Functional Groups on Low-Temperature Combustion Chemistry of Biofuels. *Progress in Energy and Combustion Science* **2021**, *86*, 100925. https://doi.org/10.1016/j.pecs.2021.100925.
(27) Jeevahan, J.; Mageshwaran, G.; Joseph, G. B.; Raj, R. B. D.; Kannan, R. T. Various Strategies for Reducing No *x* Emissions of Biodiesel Fuel Used in Conventional Diesel Engines: A Review. *Chemical Engineering Communications* **2017**, *204* (10), 1202–1223. https://doi.org/10.1080/00986445.2017.1353500.
(28) Kalghatgi, G. T. The Outlook for Fuels for Internal Combustion Engines. *International Journal of Engine Research* **2014**, *15* (4), 383–398. https://doi.org/10.1177/1468087414526189.
(29) Khaled, F.; Badra, J.; Farooq, A. Ignition Delay Time Correlation of Fuel Blends Based on Livengood-Wu Description. *Fuel* **2017**, *209*, 776–786. https://doi.org/10.1016/j.fuel.2017.07.095.

(30) Hanson, R. K.; Davidson, D. F. Recent Advances in Laser Absorption and Shock Tube Methods for Studies of Combustion Chemistry. *Progress in Energy and Combustion Science* **2014**, *44*, 103–114. https://doi.org/10.1016/j.pecs.2014.05.001.
(31) Goldsborough, S. S.; Hochgreb, S.; Vanhove, G.; Wooldridge, M. S.; Curran, H. J.; Sung, C.-J. Advances in Rapid Compression Machine Studies of Low- and Intermediate-Temperature Autoignition Phenomena. *Progress in Energy and Combustion Science* **2017**, *63*, 1–78.
(32) Al Rashidi, M. J.; Mármol, J. C.; Banyon, C.; Sajid, M. B.; Mehl, M.; Pitz, W. J.; Mohamed, S.; Alfazazi, A.; Lu, T.; Curran, H. J.; Farooq, A.; Sarathy, S. M. Cyclopentane Combustion. Part II. Ignition Delay Measurements and Mechanism Validation. *Combustion and Flame* **2017**, *183*, 372–385. https://doi.org/10.1016/j.combustflame.2017.05.017.
(33) Al Rashidi, M. J.; Mehl, M.; Pitz, W. J.; Mohamed, S.; Sarathy, S. M. Cyclopentane Combustion Chemistry. Part I: Mechanism Development and Computational Kinetics. *Combustion and Flame* **2017**, *183*, 358–371. https://doi.org/10.1016/j.combustflame.2017.05.018.
(34) Fenard, Y.; Gil, A.; Vanhove, G.; Carstensen, H.-H.; Van Geem, K. M.; Westmoreland, P. R.; Herbinet, O.; Battin-Leclerc, F. A Model of Tetrahydrofuran Low-Temperature Oxidation Based on Theoretically Calculated Rate Constants. *Combustion and Flame* **2018**, *191*, 252–269. https://doi.org/10.1016/j.combustflame.2018.01.006.
(35) Cox, R. A.; Cole, J. A. Chemical Aspects of the Autoignition of Hydrocarbon□air Mixtures. *Combustion and Flame* **1985**, *60* (2), 109–123. https://doi.org/10.1016/0010-2180(85)90001-X.
(36) Savee, J. D.; Papajak, E.; Rotavera, B.; Huang, H.; Eskola, A. J.; Welz, O.; Sheps, L.; Taatjes, C. A.; Zador, J.; Osborn, D. L. Direct Observation and Kinetics of a Hydroperoxyalkyl Radical (QOOH). *Science* **2015**, *347* (6222), 643–646. https://doi.org/10.1126/science.aaa1495.
(37) Koritzke, A. L.; Davis, J. C.; Caravan, R. L.; Christianson, M. G.; Osborn, D. L.; Taatjes, C. A.; Rotavera, B. ̇QOOH-Mediated Reactions in Cyclohexene Oxidation. *Proceedings of the Combustion Institute* **2018**. https://doi.org/10.1016/j.proci.2018.05.029.
(38) Tran, L.-S.; Herbinet, O.; Carstensen, H.-H.; Battin-Leclerc, F. Chemical Kinetics of Cyclic Ethers in Combustion. *Progress in Energy and Combustion Science* **2022**, *92*, 101019. https://doi.org/10.1016/j.pecs.2022.101019.
(39) Davis, J. C.; Koritzke, A. L.; Caravan, R. L.; Antonov, I. O.; Christianson, M. G.; Doner, A. C.; Osborn, D. L.; Sheps, L.; Taatjes, C. A.; Rotavera, B. Influence of the Ether Functional Group on Ketohydroperoxide Formation in Cyclic Hydrocarbons: Tetrahydropyran and Cyclohexane. *The Journal of Physical Chemistry A* **2019**, *123* (17), 3634–3646. https://doi.org/10.1021/acs.jpca.8b12510.
(40) *Emissions of air pollutants in the UK – Particulate matter (PM10 and PM2.5)*. GOV.UK. https://www.gov.uk/government/statistics/emissions-of-air-pollutants/emissions-of-air-pollutants-in-the-uk-particulate-matter-pm10-and-pm25 (accessed 2022-09-19).
(41) *The 2021 EPA Automotive Trends Report: Greenhouse Gas Emissions, Fuel Economy, and Technology since 1975*; EPA-420-S-21-002; 2021.

(42) European Commission. Joint Research Centre. *Electric and Hybrid Vehicle Testing: BMWi3 Performance Assessment in Realistic Use Scenarios.*; Publications Office: LU, 2018.
(43) Timmers, V. R. J. H.; Achten, P. A. J. Non-Exhaust PM Emissions from Electric Vehicles. *Atmospheric Environment* **2016**, *134*, 10–17. https://doi.org/10.1016/j.atmosenv.2016.03.017.
(44) Uygun, Y.; Ishihara, S.; Olivier, H. A High Pressure Ignition Delay Time Study of 2-Methylfuran and Tetrahydrofuran in Shock Tubes. *Combustion and Flame* **2014**, *161* (10), 2519–2530. https://doi.org/10.1016/j.combustflame.2014.04.004.
(45) Aldhaidhawi, M.; Najee, M.; Mahboba, M. H. Engine Performance and Emission Formation of a Diesel Engine Fueled with Biodiesel B15 at Different Injection Timings. *IOP Conf. Ser.: Mater. Sci. Eng.* **2019**, *518* (3), 032024. https://doi.org/10.1088/1757-899X/518/3/032024.
(46) Vanhove, G.; Yu, Y.; Boumehdi, M. A.; Frottier, O.; Herbinet, O.; Glaude, P.-A.; Battin-Leclerc, F. Experimental Study of Tetrahydrofuran Oxidation and Ignition in Low-Temperature Conditions. *Energy & Fuels* **2015**, *29* (9), 6118–6125. https://doi.org/10.1021/acs.energyfuels.5b01057.
(47) Curran, H. J. Developing Detailed Chemical Kinetic Mechanisms for Fuel Combustion. *Proceedings of the Combustion Institute* **2019**, *37* (1), 57–81. https://doi.org/10.1016/j.proci.2018.06.054.
(48) Blurock, E.; Battin-Leclerc, F. Modeling Combustion with Detailed Kinetics Mechanisms. In *Cleaner Combustion*; Battin-Leclerc, F., Simmie, J. M., Blurock, E., Eds.; Green Energy and Technology; Springer London: London, 2013; pp 17-57183–57210. https://doi.org/10.1007/978-1-4471-5307-8_8.
(49) Klippenstein, S. J. From Theoretical Reaction Dynamics to Chemical Modeling of Combustion. *Proceedings of the Combustion Institute* **2017**, *36* (1), 77–111. https://doi.org/10.1016/j.proci.2016.07.100.
(50) Cai, L.; Pitsch, H.; Mohamed, S. Y.; Raman, V.; Bugler, J.; Curran, H.; Sarathy, S. M. Optimized Reaction Mechanism Rate Rules for Ignition of Normal Alkanes. *Combustion and Flame* **2016**, *173*, 468–482. https://doi.org/10.1016/j.combustflame.2016.04.022.
(51) Curran, H. J.; Gaffuri, P.; Pitz, W. J.; Westbrook, C. K. A Comprehensive Modeling Study of N-Heptane Oxidation. *Combustion and Flame* **1998**, *114* (1–2), 149–177. https://doi.org/10.1016/S0010-2180(97)00282-4.
(52) Atkinson, R. A Structure-Activity Relationship for the Estimatation of Rate Constants for the Gas-Phase Reactions of OH Radicals with Organic Compounds. *International Journal of Chemical Kinetics* **1987**, *19*, 799–828.
(53) Herbinet, O.; Dayma, G. Jet-Stirred Reactors. In *Cleaner Combustion*; Battin-Leclerc, F., Simmie, J. M., Blurock, E., Eds.; Green Energy and Technology; Springer London: London, 2013; pp 183–210. https://doi.org/10.1007/978-1-4471-5307-8_8.
(54) ANSYS Chemkin Theory Manual 17.0 (15151), 2015.
(55) Tran, L.-S.; Verdicchio, M.; Monge, F.; Martin, R. C.; Bounaceur, R.; Sirjean, B.; Glaude, P.-A.; Alzueta, M. U.; Battin-Leclerc, F. An Experimental and Modeling Study of the Combustion of Tetrahydrofuran. *Combustion and Flame* **2015**, *162* (5), 1899–1918. https://doi.org/10.1016/j.combustflame.2014.12.010.

(56) Cord, M.; Sirjean, B.; Fournet, R.; Tomlin, A.; Ruiz-Lopez, M.; Battin-Leclerc, F. Improvement of the Modeling of the Low-Temperature Oxidation of *n* -Butane: Study of the Primary Reactions. *J. Phys. Chem. A* **2012**, *116* (24), 6142–6158. https://doi.org/10.1021/jp211434f.
(57) Doner, A. C.; Davis, M. M.; Koritzke, A. L.; Christianson, M. G.; Turney, J. M.; Schaefer, H. F.; Sheps, L.; Osborn, D. L.; Taatjes, C. A.; Rotavera, B. Isomer-dependent Reaction Mechanisms of Cyclic Ether Intermediates: *Cis* -2,3-dimethyloxirane and *Trans* -2,3-dimethyloxirane. *International Journal of Chemical Kinetics* **2021**, *53* (1), 127–145. https://doi.org/10.1002/kin.21429.
(58) Hartness, S. W.; Dewey, N. S.; Christianson, M. G.; Koritzke, A. L.; Doner, A. C.; Webb, A. R.; Rotavera, B. Probing O2-Dependence of Hydroperoxy-Butyl Reactions via Isomer-Resolved Speciation. *Proceedings of the Combustion Institute* **2022**, *39*.
(59) Ranzi, E.; Frassoldati, A.; Granata, S.; Faravelli, T. Wide-Range Kinetic Modeling Study of the Pyrolysis, Partial Oxidation, and Combustion of Heavy *n* -Alkanes. *Ind. Eng. Chem. Res.* **2005**, *44* (14), 5170–5183. https://doi.org/10.1021/ie049318g.
(60) Ranzi, E.; Dente, M.; Goldaniga, A.; Bozzano, G.; Faravelli, T. Lumping Procedures in Detailed Kinetic Modeling of Gasification, Pyrolysis, Partial Oxidation and Combustion of Hydrocarbon Mixtures. *Progress in Energy and Combustion Science* **2001**, *27* (1), 99–139. https://doi.org/10.1016/S0360-1285(00)00013-7.
(61) Tomlin, A. S.; Turányi, T. Mechanism Reduction to Skeletal Form and Species Lumping. In *Cleaner Combustion: Developing Detailed Chemical Kinetic Models*; Battin-Leclerc, F., Simmie, J. M., Blurock, E., Eds.; Green Energy and Technology; Springer: London, 2013; pp 447–466. https://doi.org/10.1007/978-1-4471-5307-8_17.
(62) Wu, Y.; Xu, N.; Yang, M.; Liu, Y.; Tang, C.; Huang, Z. Ignition Delay Time Measurement and Kinetic Modeling of Furan, and Comparative Studies of 2,3-Dihydrofuran and Tetrahydrofuran at Low to Intermediate Temperatures by Using a Rapid Compression Machine. *Combustion and Flame* **2020**, *213*, 226–236. https://doi.org/10.1016/j.combustflame.2019.12.010.
(63) Jorand, F.; Heiss, A.; Perrin, O.; Sahetchian, K.; Kerhoas, L.; Einhorn, J. Isomeric Hexyl-Ketohydroperoxides Formed by Reactions of Hexoxy and Hexylperoxy Radicals in Oxygen. *International Journal of Chemical Kinetics* **2003**, *35* (8), 354–366. https://doi.org/10.1002/kin.10136.
(64) Bugler, J.; Rodriguez, A.; Herbinet, O.; Battin-Leclerc, F.; Togbé, C.; Dayma, G.; Dagaut, P.; Curran, H. J. An Experimental and Modelling Study of N-Pentane Oxidation in Two Jet-Stirred Reactors: The Importance of Pressure-Dependent Kinetics and New Reaction Pathways. *Proceedings of the Combustion Institute* **2017**, *36* (1), 441–448. https://doi.org/10.1016/j.proci.2016.05.048.
(65) Ulonska, K.; Voll, A.; Marquardt, W. Screening Pathways for the Production of Next Generation Biofuels. *Energy Fuels* **2016**, *30* (1), 445–456. https://doi.org/10.1021/acs.energyfuels.5b02460.
(66) Geilen, F. M. A.; Engendahl, B.; Harwardt, A.; Marquardt, W.; Klankermayer, J.; Leitner, W. Selective and Flexible Transformation of Biomass-Derived Platform Chemicals by a Multifunctional Catalytic System. *Angewandte Chemie*

International Edition **2010**, *49* (32), 5510–5514. https://doi.org/10.1002/anie.201002060.
(67) Minetti, R.; Ribaucour, M.; Carlier, M.; Fittschen, C.; Sochet, L. R. Experimental and Modeling Study of Oxidation and Autoignition of Butane at High Pressure. *Combustion and Flame* **1994**, *96* (3), 201–211. https://doi.org/10.1016/0010-2180(94)90009-4.
(68) Wilk, R. D.; Pitz, W. J.; Westbrook, C. K.; Addagarla, S.; Miller, D. L.; Cernansky, N. P.; Green, R. M. Combustion of N-Butane and Isobutane in an Internal Combustion Engine: A Comparison of Experimental and Modeling Results. *Symposium (International) on Combustion* **1991**, *23* (1), 1047–1053. https://doi.org/10.1016/S0082-0784(06)80363-2.
(69) Eskola, A. J.; Welz, O.; Savee, J. D.; Osborn, D. L.; Taatjes, C. A. Synchrotron Photoionization Mass Spectrometry Measurements of Product Formation in Low-Temperature *n* -Butane Oxidation: Toward a Fundamental Understanding of Autoignition Chemistry and *n* -$C_4H_9 + O_2$ / *s* -$C_4H_9 + O_2$ Reactions. *The Journal of Physical Chemistry A* **2013**, *117* (47), 12216–12235. https://doi.org/10.1021/jp408467g.
(70) Antonov, I. O.; Zádor, J.; Rotavera, B.; Papajak, E.; Osborn, D. L.; Taatjes, C. A.; Sheps, L. Pressure-Dependent Competition among Reaction Pathways from First- and Second-O_2 Additions in the Low-Temperature Oxidation of Tetrahydrofuran. *The Journal of Physical Chemistry A* **2016**, *120* (33), 6582–6595. https://doi.org/10.1021/acs.jpca.6b05411.
(71) Dagaut, P.; Mcguinness, M.; Simmie, J. M.; Cathonnet, M. The Ignition and Oxidation of Tetrahydrofuran: Experiments and Kinetic Modeling. *Combustion Science and Technology* **1998**, *135* (1–6), 3–29. https://doi.org/10.1080/00102209808924147.
(72) Hansen, N.; Moshammer, K.; Jasper, A. W. Isomer-Selective Detection of Keto-Hydroperoxides in the Low-Temperature Oxidation of Tetrahydrofuran. *J. Phys. Chem. A* **2019**, *123* (38), 8274–8284. https://doi.org/10.1021/acs.jpca.9b07017.
(73) Belhadj, N.; Benoit, R.; Dagaut, P.; Lailliau, M. Experimental Characterization of Tetrahydrofuran Low-Temperature Oxidation Products Including Ketohydroperoxides and Highly Oxygenated Molecules. *Energy Fuels* **2021**, *35* (9), 7242–7252. https://doi.org/10.1021/acs.energyfuels.0c03291.
(74) Molera, M. J.; Couto, A.; Garcia-Dominguez, J. A. Gas Phase Oxidation of Tetrahydrofuran. *Int. J. Chem. Kinet.* **1988**, *20* (9), 673–685. https://doi.org/10.1002/kin.550200902.
(75) Lockwood, K. S.; Labbe, N. J. Insights on Keto-Hydroperoxide Formation from O2 Addition to the Beta-Tetrahydrofuran Radical. *Proceedings of the Combustion Institute* **2021**, *38* (1), 533–541. https://doi.org/10.1016/j.proci.2020.06.357.
(76) Davis, J. C. DESIGN OF A HIGH-PRESSURE JET-STIRRED REACTOR FACILITY FOR GAS-PHASE CHEMICAL KINETICS. 91.
(77) Heitor, M. V.; Moreira, A. L. N. Thermocouples and Sample Probes for Combustion Studies. *Progress in Energy and Combustion Science* **1993**, *19* (3), 259–278. https://doi.org/10.1016/0360-1285(93)90017-9.
(78) Doner, A. C.; Christianson, M. G.; Davis, J. C.; Koritzke, A. L.; Larsson, A.; Frandsen, K.; Rotavera, B. Vacuum-Ultraviolet Absorption Cross-Sections of

Functionalized Cyclic Hydrocarbons: Six-Membered Rings. *Journal of Quantitative Spectroscopy and Radiative Transfer* **2019**, *236*, 106603. https://doi.org/10.1016/j.jqsrt.2019.106603.
(79) Christianson, M. G.; Doner, A. C.; Koritzke, A. L.; Frandsen, K.; Rotavera, B. Vacuum-Ultraviolet Absorption Cross-Sections of Functionalized Cyclic Hydrocarbons: Five-Membered Rings. *Journal of Quantitative Spectroscopy and Radiative Transfer* **2021**, *258*, 107274. https://doi.org/10.1016/j.jqsrt.2020.107274.
(80) Doner, A. C.; Webb, A. R.; Dewey, N. S.; Hartness, S. W.; Christianson, M. G.; Koritzke, A. L.; Larsson, A.; Frandsen, K. M.; Rotavera, B. Vacuum-Ultraviolet Absorption Cross-Sections of Functionalized Four-Carbon Species. *Journal of Quantitative Spectroscopy and Radiative Transfer* **2022**, *292*, 108346. https://doi.org/10.1016/j.jqsrt.2022.108346.
(81) McLafferty, F. W.; Turecek, F. *Interpretation of Mass Spectra*; University Science Books, 1993.
(82) Dagaut, P.; Reuillon, M.; Cathonnet, M.; Presvots, D. Gas Chromatography and Mass Spectrometry Identification of Cyclic Ethers Formed from Reference Fuels Combustion. *Chromatographia* **1995**, *40* (3–4), 147–154. https://doi.org/10.1007/BF02272163.
(83) Blin-Simiand, N.; Jorand, F.; Sahetchian, K.; Brun, M.; Kerhoas, L.; Malosse, C.; Einhorn, J. Hydroperoxides with Zero, One, Two or More Carbonyl Groups Formed during the Oxidation of n-Dodecane. *Combustion and Flame* **2001**, *126* (1–2), 1524–1532. https://doi.org/10.1016/S0010-2180(01)00264-4.
(84) Koritzke, A. L.; Frandsen, K. M.; Christianson, M. G.; Davis, J. C.; Doner, A. C.; Larsson, A.; Breda-Nixon, J.; Rotavera, B. Fragmentation Mechanisms from Electron-Impact of Complex Cyclic Ethers Formed in Combustion. *International Journal of Mass Spectrometry* **2020**, *454*, 116342. https://doi.org/10.1016/j.ijms.2020.116342.
(85) Dagaut, P.; Cathonnet, M. Oxidation of Neopentane in a Jet-Stirred Reactor from 1 to 10 Atm: An Experimental and Detailed Kinetic Modeling Study. *Combustion and Flame* **1999**, *118* (1–2), 191–203. https://doi.org/10.1016/S0010-2180(98)00147-3.
(86) Schug, K. A.; Sawicki, I.; Carlton, D. D.; Fan, H.; McNair, H. M.; Nimmo, J. P.; Kroll, P.; Smuts, J.; Walsh, P.; Harrison, D. Vacuum Ultraviolet Detector for Gas Chromatography. *Anal. Chem.* **2014**, *86* (16), 8329–8335. https://doi.org/10.1021/ac5018343.
(87) Cai, L.; Minwegen, H.; Beeckmann, J.; Burke, U.; Tripathi, R.; Ramalingam, A.; Kröger, L. C.; Sudholt, A.; Leonhard, K.; Klankermayer, J.; Heufer, K. A.; Pitsch, H. Experimental and Numerical Study of a Novel Biofuel: 2-Butyltetrahydrofuran. *Combustion and Flame* **2017**, *178*, 257–267. https://doi.org/10.1016/j.combustflame.2016.12.021.
(88) Tripathi, R.; Lee, C.; Fernandes, R. X.; Olivier, H.; Curran, H. J.; Mani Sarathy, S.; Pitsch, H. Ignition Characteristics of 2-Methyltetrahydrofuran: An Experimental and Kinetic Study. *Proceedings of the Combustion Institute* **2017**, *36* (1), 587–595. https://doi.org/10.1016/j.proci.2016.07.103.
(89) Tran, L.-S.; Wang, Z.; Carstensen, H.-H.; Hemken, C.; Battin-Leclerc, F.; Kohse-Höinghaus, K. Comparative Experimental and Modeling Study of the Low- to Moderate-Temperature Oxidation Chemistry of 2,5-Dimethylfuran, 2-Methylfuran,

and Furan. *Combustion and Flame* **2017**, *181*, 251–269. https://doi.org/10.1016/j.combustflame.2017.03.030.
(90) Rotavera, B.; Savee, J. D.; Antonov, I. O.; Caravan, R. L.; Sheps, L.; Osborn, D. L.; Zádor, J.; Taatjes, C. A. Influence of Oxygenation in Cyclic Hydrocarbons on Chain-Termination Reactions from R + O2: Tetrahydropyran and Cyclohexane. *Proceedings of the Combustion Institute* **2017**, *36* (1), 597–606. https://doi.org/10.1016/j.proci.2016.05.020.
(91) Dubnikova, F.; Lifshitz, A. Isomerization of 2,3-Dihydrofuran and 5-Methyl-2,3-Dihydrofuran: Quantum Chemical and Kinetics Calculations. *J. Phys. Chem. A* **2002**, *106* (6), 1026–1034. https://doi.org/10.1021/jp012714h.
(92) Tomas, A.; Villenave, E.; Lesclaux, R. Kinetics of the (CH3)2CHCO and (CH3)3CCO Radical Decomposition: Temperature and Pressure Dependences. *Phys. Chem. Chem. Phys.* **2000**, *2* (6), 1165–1174. https://doi.org/10.1039/a909377j.
(93) Curran, H. J. Rate Constant Estimation for C1 to C4 Alkyl and Alkoxyl Radical Decomposition. *Int. J. Chem. Kinet.* **2006**, *38* (4), 250–275. https://doi.org/10.1002/kin.20153.
(94) DeSain, J. D.; Klippenstein, S. J.; Miller, J. A.; Taatjes, C. A. Measurements, Theory, and Modeling of OH Formation in Ethyl + O_2 and Propyl + O_2 Reactions. *J. Phys. Chem. A* **2003**, *107* (22), 4415–4427. https://doi.org/10.1021/jp0221946.
(95) Huang, H.; Merthe, D. J.; Zádor, J.; Jusinski, L. E.; Taatjes, C. A. New Experiments and Validated Master-Equation Modeling for OH Production in Propyl+O2 Reactions. *Proceedings of the Combustion Institute* **2011**, *33* (1), 293–299. https://doi.org/10.1016/j.proci.2010.06.039.
(96) Simmie, J. M. Kinetics and Thermochemistry of 2,5-Dimethyltetrahydrofuran and Related Oxolanes: Next Next-Generation Biofuels. *J. Phys. Chem. A* **2012**, *116* (18), 4528–4538. https://doi.org/10.1021/jp301870w.
(97) Giri, B. R.; Khaled, F.; Szőri, M.; Viskolcz, B.; Farooq, A. An Experimental and Theoretical Kinetic Study of the Reaction of OH Radicals with Tetrahydrofuran. *Proceedings of the Combustion Institute* **2017**, *36* (1), 143–150. https://doi.org/10.1016/j.proci.2016.06.016.
(98) Sudholt, A.; Cai, L.; Heyne, J.; Haas, F. M.; Pitsch, H.; Dryer, F. L. Ignition Characteristics of a Bio-Derived Class of Saturated and Unsaturated Furans for Engine Applications. *Proceedings of the Combustion Institute* **2015**, *35* (3), 2957–2965. https://doi.org/10.1016/j.proci.2014.06.147.
(99) Dubnikova, F.; Lifshitz, A. Molecular Hydrogen Elimination From 2,5-Dihydrofuran, 2,3-Dihydrofuran, and 2-Methyl-2,5-Dihydrofuran: Quantum Chemical and Kinetics Calculations. *International Journal of Chemical Kinetics* **2001**, *33* (11), 685–697.
(100) Zádor, J.; Klippenstein, S. J.; Miller, J. A. Pressure-Dependent OH Yields in Alkene + HO_2 Reactions: A Theoretical Study. *J. Phys. Chem. A* **2011**, *115* (36), 10218–10225. https://doi.org/10.1021/jp2059276.
(101) Doner, A. C.; Zádor, J.; Rotavera, B. Stereoisomer-Dependent Unimolecular Kinetics of 2,4- **Dimethyloxetanyl** Peroxy Radicals. *Faraday Discuss.* **2022**, 10.1039.D2FD00029F. https://doi.org/10.1039/D2FD00029F.
(102) Christianson, M. G.; Doner, A. C.; Davis, M. M.; Koritzke, A. L.; Turney, J. M.; Schaefer, H. F.; Sheps, L.; Osborn, D. L.; Taatjes, C. A.; Rotavera, B. Reaction

Mechanisms of a Cyclic Ether Intermediate: Ethyloxirane. *International Journal of Chemical Kinetics* **2021**, *53* (1), 43–59. https://doi.org/10.1002/kin.21423.
(103) Rotavera, B.; Caravan, R. L.; Taatjes, C. A. Subsequent R + O2 Chemistry of Intermediates Formed in Low-Temperature R + O2 Reactions: Potential Importance in Modeling Autoignition Behavior. 61.
(104) Faravelli, T.; Manenti, F.; Ranzi, E. *Mathematical Modelling of Gas-Phase Complex Reaction Systems: Pyrolysis and Combustion*; Elsevier, 2019.
(105) Herbinet, O.; Glaude, P.-A.; Fournet, R.; Zhou, Z.; Deng, L.; Guo, H.; Xie, M.; Qi, F. Detailed Product Analysis during the Low Temperature Oxidation of N-Butanew. **2011**, 13.

APPENDIX A

DEVELOPMENT OF SYRINGE-INJECTION OF LIQUIDS TO GC

Because the process for making gas-phase mixtures is dependent on the vapor pressure of the species, occasionally a species is unable to reach the minimum necessary pressure of ~0.5 Torr, despite external heating. Instead, the liquid can be injected into the GC for measurement of reference spectra. However out of concern that saturation limits would be surpassed causing the accompanying signal to be too saturated to use for quantification, a new method was developed to mitigate these concerns.

The GC split ratio and liquid injection volume were optimized where the best combination was determined by observing measured absorbance of dichloromethane (DCM) with the majority of spectral features under the saturation limit. It is worth noting that the entire spectrum need not fall within saturation limits as the quantification technique selects specific spectral ranges over which to quantify. Under normal operating conditions the split ratio for the column that leads to the MS is 14:1 where that leading to the VUV is 11:1. The split ratio was adjusted to dilute the injected liquid by a factor of 10, 20, 30, 50 (**Table A1**).

Table A1. Split ratios and corresponding dilution factors tested to mitigate saturation concerns with liquid injection.

Dilution Factor	GC (MS) Split Ratio	GC (VUV) Split Ratio
1	14:1	11:1
10	140:1	110:1
20	280:1	220:1
30	420:1	330:1
50	700:1	550:1

The injection volume was bound by the size of available syringes. An Agilent fixed cone-type 10 μL syringe made of stainless steel was used initially to test a volume of 0.1 μL. However, variability in syringe volume was too great as slight variations in manual operation of the syringe resulted in large volume changes. In addition, 0.1 μL approached the lower limit of the syringe volume range, so smaller 5 μL stainless steel syringes were used instead. Volumes of 0.05 and 0.2 μL were tested at the previously discussed split ratios.

The results are shown in **Figure A1**. While all conditions have spectral features that fall below the saturation limit, it was important to note that the spectral features present in DCM, may not be present in all species that will be manually injected. Additionally, not all species may absorb at lower energies. Therefore, the conditions chosen as optimal had the most signal under the saturation limit at the most wavelengths. Although, this would appear to be a dilution factor of 50 and a volume of 0.05 μL, given the variation in volume that results from manual use of the syringe and given that a larger volume would be less sensitive, the optimized conditions were chosen to be a dilution factor of 30 and volume of 0.2 μL. Further testing to cover a wider range of conditions may be helpful, specifically a volume of 0.2 μL at a dilution factor of 50, which was omitted from this test due to time constraints.

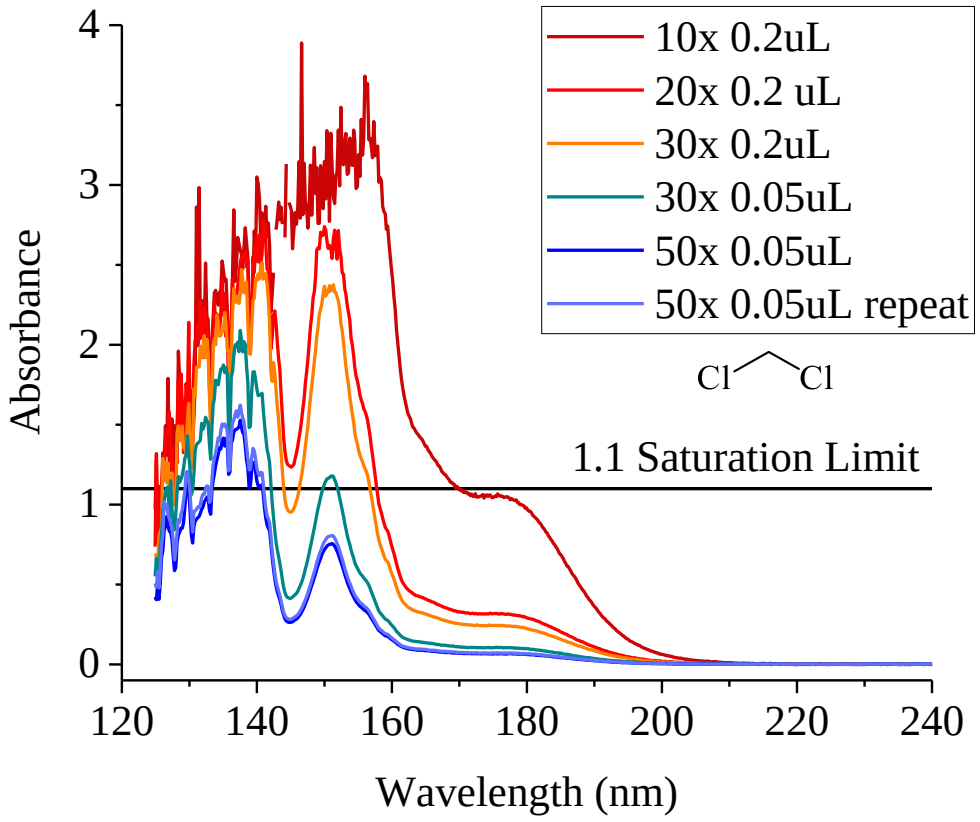

Figure A1. Results of split ratio and injection volume optimization where warm colors represent volume of 0.2 μL and cool colors are 0.05 μL.

APPENDIX B

EXTERNAL COLLABORATIVE WORK

B.1 ADVANCED LIGHT SOURCE PROJECTS

Several combustion projects were completed using the Advanced Light Source at Lawrence Berkeley National Laboratory where low-temperature oxidation was studied for cyclohexene, tetrahydropyran, ethyloxirane, and *cis*- and *trans*-2,3-dimethyloxirane. I completed the experiments for cyclohexene where for tetrahydropyran, ethyloxirane, and 2,3-dimethyloxirane, I contributed substantially to the post-processing and analysis of data collected from experiments performed by other members of the Rotavera group. I co-authored a first-author publication for the work on cyclohexene in Proceedings of the Combustion Institute and the other projects on tetrahydropyran and the oxiranes have been published in The Journal of Physical Chemistry A and The International Journal of Chemical Kinetics, respectively.[37,39,57,102]

B.1.1 Oxidation of cyclohexene at low-temperature

In a similar manner to how to tetrahydrofuran can be studied in comparison to cyclopentane to understand how the presence of an ether group influence low-temperature chemistry, a comparison can be made for cyclohexene and cyclohexane to study the influence of a pi-bond. Cyclohexene is relevant as an intermediate of cyclohexane combustion where cyclohexyl + O_2 → cyclohexene + HOȮ shown in **Figure B1a**, so

understanding cyclohexene combustion will enhance the understanding of cyclohexane combustion.

The pi-bond in cyclohexene can allow for resonance stabilization of cyclohexenyl radical when H-abstraction occurs on the α-site relative to the location of the pi-bond (**Figure B1b**). Resonance-stabilization also occurs on several ȮOOH species including α-ȮOOH, δ-ȮOOH, β'-ȮOOH, and γ'-ȮOOH (**Figure B1c**). The purpose of this work was to study the effect of the pi-bond and subsequent resonance stabilization on low-temperature combustion chemistry by measuring combustion products from which mechanistic information could be inferred.

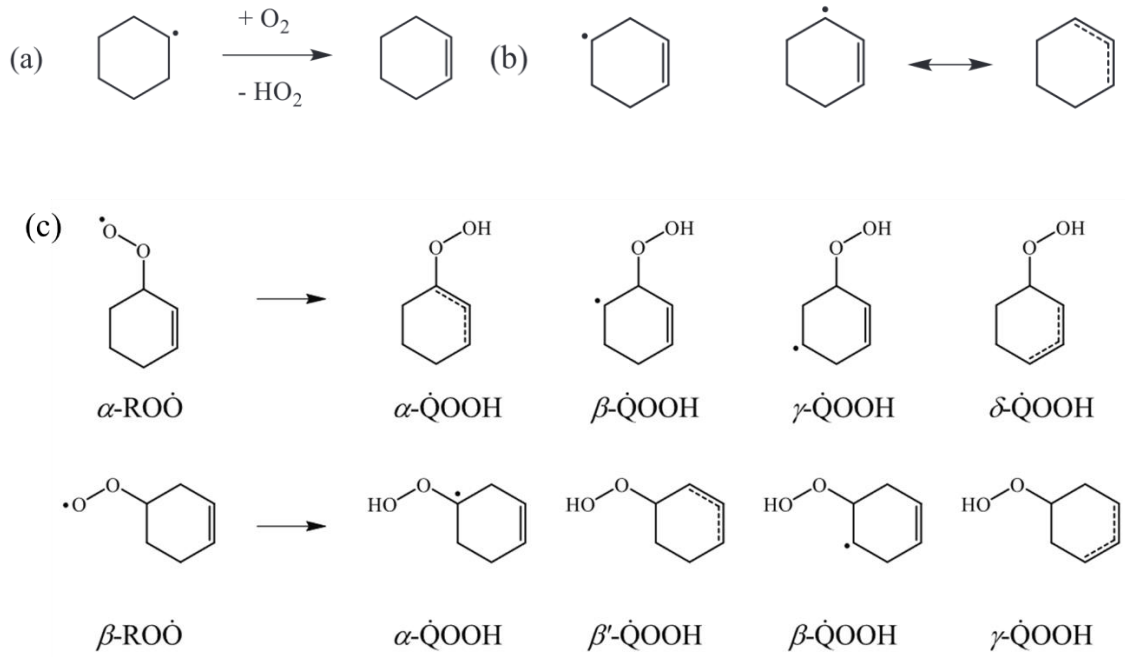

Figure B1. Formation of cyclohexene from cyclohexane oxidation (a), resonance stabilization of cyclohexenyl radicals (b) and ȮOOH species (c).

Multiplexed photoionization mass spectrometry (MPIMS) experiments were conducted from 500 – 700 K and 10 Torr and an experimental schematic is shown in **Figure B2**. Fuel, Cl_2, O_2, and diluent (He) is flowed through a quartz reactor where the reaction is photolytically initiated using a pulsed excimer laser of 351-nm light, which generates Ċl atoms instantaneously and homogenously along the reactor. The Ċl atoms react with cyclohexene via cyclohexene + Ċl → cyclohexenyl + HCl generating the initial Ṙ radical pool, which subsequently undergo pseudo-first reaction with O_2. Products from the reaction are directed through a 600-μm side orifice into a detector region where they are intersected with a molecular beam with tunable VUV synchrotron radiation and detected using a time-of-flight mass spectrometer. Three-dimensional data is collected including high-resolution mass spectra, photoionization cross sections, and time-dependent kinetic signal. In addition to reactive experiments, unreactive experiments were performed to measure individual photoionization cross-section references needed for combustion product identification. Further experimental information can be found in Koritzke et al.[37] To support experimental results, single-point energies on potential energy surfaces of α- and β-cyclohexenyl radicals.

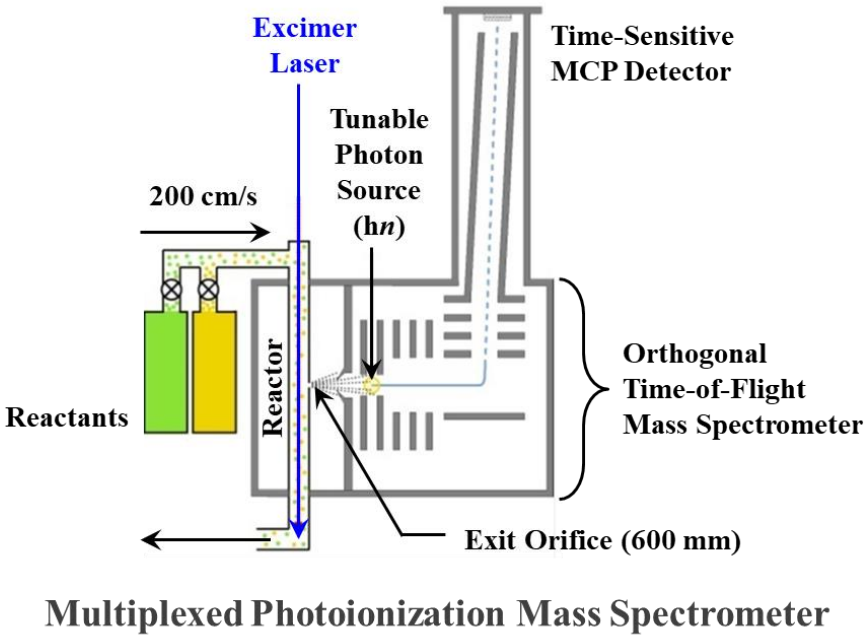

Figure B2. Multiplexed photoionization mass spectrometer (MPIMS) experiment schematic.

The main conclusion from this work was that resonance stabilization of ȮOOH facilitates second-O_2 addition pathways to ketohydroperoxide formation because it lowers the energy of and stabilizes the ȮOOH energy well, which in turn hinders ȮOOH unimolecular decomposition reactions. Ketohydroperoxide was detected at the exact mass of 128.047 amu, which corresponds to $C_6H_8O_3$. Potential energy surfaces were used to support experimental results and indicated that β-RO$\dot{O}$ → γ-ȮOOH, which is resonance stabilized, is 8.3 kcal/mol lower in comparison to the same reaction for cyclohexane, without the pi-bond (c.f. **Figure 6a**). Therefore, the barrier for unimolecular decomposition of γ-ȮOOH increases by 8.7 kcal/mol. The same trend is observed for other resonance stabilized ȮOOH species.

B.1.2 Tetrahydropyran, ethyloxirane, and cis- *and* trans-*2,3-dimethyloxirane*

In addition to cyclohexene, MPIMS experiments were conducted on tetrahydropyran, ethyloxirane, and *cis*- and *trans*-2,3-dimethyloxirane. The ether group in tetrahydropyran affects the complexity of understanding reaction mechanisms because the introduction of a functional group increases the number of initial radicals in comparison to cyclohexane from one radical (cyclohexyl) to three (α-, β-, and γ-tetrahydropyranyl). Additionally, the presence of oxygen draws electronegativity from adjacent C-H bonds, lowering their bond dissociation energies and enabling facile H-abstraction.[90,97] Nine products of tetrahydropyran oxidation were quantified to determine the role of ring-opening reactions in diminishing the ȮOOH radical pool available for second-O_2 addition due to the ether group. Three pathways were determined to be dominant and depleting the ȮOOH radical pool available for second-O_2 addition (**Figure B3**): (a) α,α'-ȮOOH → pentanedial + ȮH, (b) α,α'-ȮOOH → vinyl formate + ethene + ȮH, and (c) γ-ȮOOH → 3-butenal + formaldehyde + ȮH.[39] Analogous pathways were compared for cyclohexane oxidation, but in the absence of analogous products based on mass spectral results, ring-opening reactions were confirmed to not be occurring (c.f. **Figure 6b**). Therefore, the ether group on tetrahydropyran facilitated ring-opening pathways.

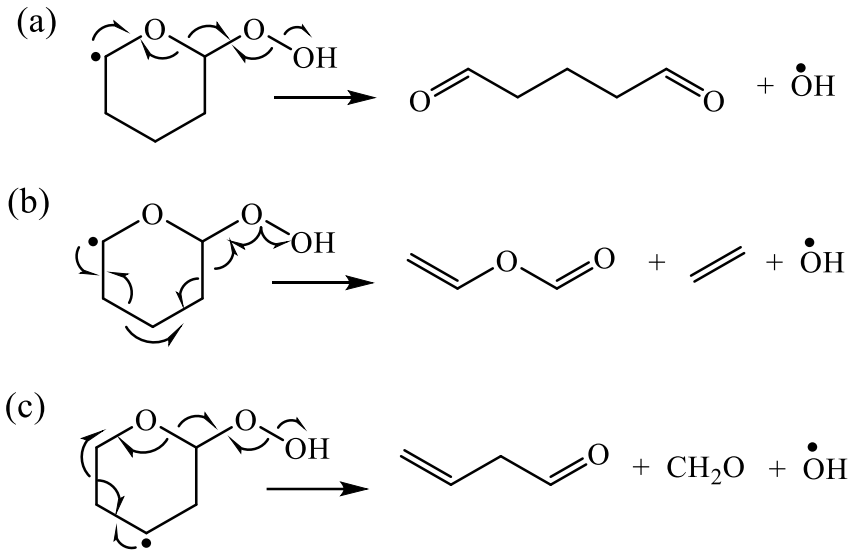

Figure B3. Three ring-opening pathways of tetrahydropyran that are facilitated by the presence of the ether group and form three detected products: (a) pentanedial, (b) vinyl formate, and (c) 3-butenal.

Ethyloxirane and 2,3-dimethyloxirane were studied because oxiranes are a class of cyclic ethers that are formed from low-temperature combustion of biofuels via unimolecular decomposition of ȮOOH or from HOȮ addition to alkenes.[37,103] While the formation of oxiranes are well studied, the consumption pathways are not.[103] As a result, chemical kinetics mechanisms often lump consumption pathways into a single step introducing mechanism truncation error.[104] Ethyloxirane and 2,3-dimethyloxirane are products of *n*-butane oxidation, so understanding the consumption pathways of cyclic ethers will improve upon chemical kinetics modeling of *n*-butane.[105] Additionally, stereochemical dependence of 2,3-dimethyloxirane is not accounted for in chemical kinetics mechanisms and isomer-resolved speciation measurements of *cis*- and *trans*-2,3-dimethyloxirane have not been reported. The work on ethyloxirane and *cis*- and *trans*-2,3-dimethyloxirane aim to provide the first direct experiments on oxirane consumption pathways at low-temperature and provide insight on isomer-dependence, when applicable.

Several new pathways were proposed for ethyloxirane oxidation based on detected products. One of the most important reaction classes involves a resonance-stabilized ketohydroperoxide type radical (Ṙ(=O)OOH) that is formed via ring-opening of ṠOOH species and can form products such as tetrahydrofuran-3-one and 2-butenal, which are also products of tetrahydrofuran combustion (**Figure B4**).[102] Therefore, including expanded sub-mechanisms of ethyloxirane may improve accounting of these species within chemical kinetics mechanisms of *n*-butane and tetrahydrofuran.

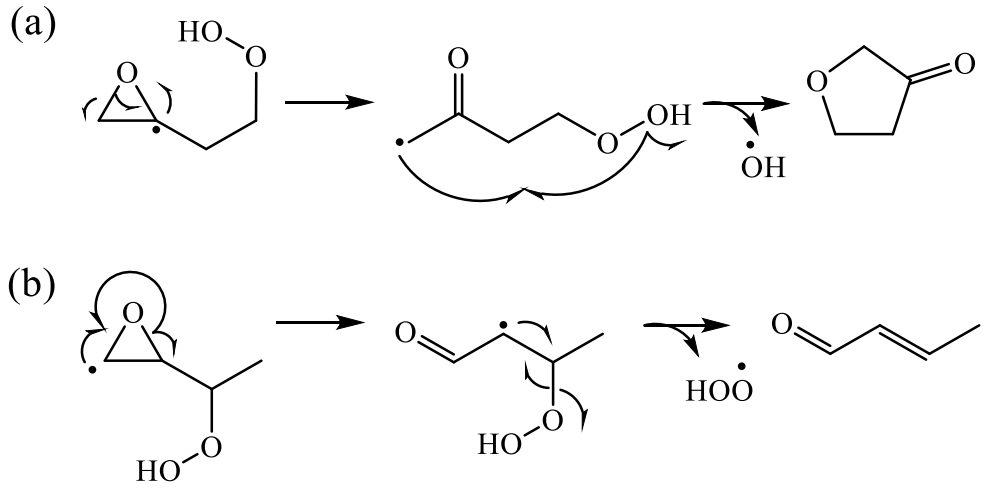

Figure B4. Reaction mechanisms for tetrahydrofuran-3-one (a) and 2-butenal (b) formation via resonance-stabilized ketohydroperoxide-type radicals.

Resonance-stabilized ketohydroperoxide-type radical mediated reactions were also important in *cis*-2,3-dimethyloxirane, namely the formation of diacetyl, which is also traditional product of 2-butyl oxidation (**Figure B5**).[57] Diacetyl has been detected in *n*-butane oxidation experiments and has previously only been attributed to ketohydroperoxide formation.[105] The results from the MPIMS experiments herein, indicate a new source of diacetyl formation from *cis*-2,3-dimethyloxirane that has been excluded from current chemical kinetics mechanisms. Furthermore, the signal-to-noise of diacetyl

in *trans*-2,3-dimethyloxirane was low, especially in comparison to that from *cis*-2,3-dimethyloxirane experiments, indicating that stereochemistry affects accessible combustion pathways. Additionally in comparison to ethyloxirane, 2,3-dimethyloxirane oxidation pathways did not include typical low-temperature alkane chemistry such as conjugate alkene formation, which may be attributed to the proximity of the unpaired electron in initial 2,3-dimethyloxirane radicals to the oxirane moiety in comparison to ethyloxirane, which favors ring-opening.[57]

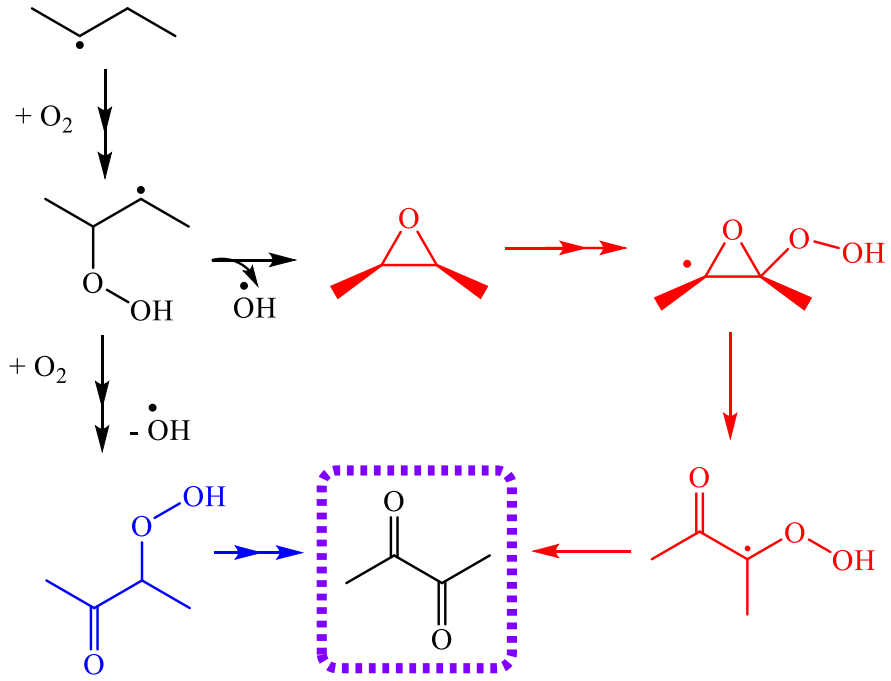

Figure B5. Pathways to diacetyl formation from 2-butyl oxidation includes ȮOOH-mediated reaction of *cis*-2,3-dimethyloxirane (red) and conventional ketohydroperoxide decomposition (blue).

APPENDIX C

STANDARD OPERATING PROCEDURES DEVELOPED

Because the Rotavera laboratory was new upon my joining, many procedures were developed in conjunction or prior to those discussed in detail in Section 2. These standard operating procedures are now used daily for all experiments by the Rotavera laboratory and therefore, are worth noting.

Table C1. Overview of standard operating procedures that were developed and are used daily within the Rotavera laboratory.

Task	Processes developed
Agilent GC-MS library operation	• How to create a customized MS library • How to add measured EI-MS reference spectra into new and existing libraries • Troubleshooting for Agilent Library program • Operation of Agilent NIST library
Operation of compression cell	• How to fill compression cell with sample and compress using integrated software • Optimized timing of compression process (compression and retraction) • Optimized time for pumping down between samples
Mass spectrometry species identification	• How to identify species with Agilent MassHunter Qualitative Analysis
Gas-phase mixture making	• Optimized static mixing time • Minimum amount of pump down time necessary before making another mixture
GC-MS startup operation and overnight procedures	• Optimal pressures of gases used (He, Ar, N_2) • Overnight operation adjustments to instrument settings • Bake out method, if needed for cleaning purposes
VUV startup operation and overnight procedures	• Optimal pressures of gases used (N_2) • Overnight makeup gas pressure • How to take on-column measurements • How to adjust lamp and grating for optimal reference scan signal